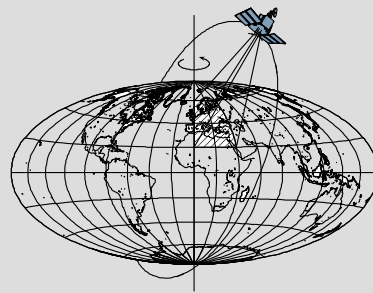


Global Ice Mass Balance and its Contribution to Early Twenty-first Century Sea Level Rise

by

Jianbin Duan



Report No. 508

Geodetic Science

The Ohio State University
Columbus, Ohio 43210

March 2014

Global Ice Mass Balance and its Contribution to
Early Twenty-first Century Sea Level Rise

DISSERTATION

Presented in Partial Fulfillment of the Requirements for the Degree Doctor of Philosophy
in the Graduate School of The Ohio State University

By
Jianbin Duan, M.S., B.S.
Graduate Program in Geodetic Science and Surveying

The Ohio State University
2013

Dissertation Committee:
Professor C.K. Shum, Advisor
Professor Christopher Jekeli
Professor Ian Howat

Copyright by
Jianbin Duan
2013

Abstract

Sea level change is an important consequence of anthropogenic climate change, both for societies and for the environment. For the past several decades, analysis of tide gauge measurements show an average rise in sea level of 1.7 ± 0.3 mm/yr from 1950 to 2009, while the analysis of satellite altimetry data indicates a rise of 3.3 ± 0.3 mm/yr from 1993 to 2009. The discrepancy of the sea level rise estimate could be due to an accelerated sea level rise over the last three decades, or that the satellite estimate is contaminated by interannual or longer oceanic signals. Mass imbalance of the polar ice sheets and major mountain glacier systems is one of the main contributors to present-day global mean sea level rise. Recent advances in the determination of the global ice mass balance show that polar ice sheets and most of the major glacier systems are losing mass. However, large discrepancy exists among these contemporary observations.

The Gravity Recovery and Climate Experiment (GRACE) satellite gravimetry mission launched in March 2002 provides a means of unprecedented accuracy and temporal and spatial resolutions to quantify global ice mass changes. In this study, we estimate ice mass balance and the associated uncertainty for the world's ice sheets, major glacier and ice cap systems by using GRACE monthly gravity fields. Our result shows that the ice mass change rate over Greenland, from Jan 2003 to Dec 2012, is -267 ± 10 Gt/yr, which is equivalent to sea level rise of 0.74 ± 0.03 mm/yr. Evident accelerated ice mass loss in Greenland was found occurring during 2010, 2011 and 2012. The mass loss rates are about twice for the years before 2010. For Antarctica, we report ice mass changes of -118 ± 30 Gt/yr (0.33 ± 0.08 mm/yr sea level rise) and -194 ± 86 Gt/yr (0.54 ± 0.24 mm/yr sea level rise) using two different Glacial isostatic Adjustment (GIA) models, the Whitehouse and the Paulson GIA models, respectively, to correct for subglacial topography uplifts due to GIA process. The contribution of mass loss from global mountain glacier and ice caps from 5 major systems including Alaska, Iceland, Canadian Arctic, High Mountain Asia (HMA) and Patagonia is considerable. We report mass changes of -171 ± 9 Gt/yr (mass loss, and an estimate of contribution to sea level rise of 0.48 ± 0.02 mm/yr, assuming the melt water immediately reaches the oceans).

In this study, we geometrically corrected the effects of spurious jumps and artificial trends in GRACE de-aliasing products due to the known errors in the ECMWF operational atmosphere model. However, the effect of these errors on the actual GRACE monthly gravity field inversion requires further studies. We found that the errors in the long-wavelength geopotential coefficients (C_{20} and C_{40}) in GRACE determined monthly gravity fields are more significant than previously thought for ice sheet mass balance estimates using GRACE. More accurate estimates of HMA glacier mass balance are only possible by improving the current knowledge of hydrologic fluxes or hydrologic model fidelity over the Qinghai-Tibetan Plateau. Here we estimated the uncertainties of

GRACE-derived mass changes based an elaborate error budget. Final estimates of global ice mass balance are calculated by applying the appropriate error propagation resulting from the estimated uncertainties. We reduced uncertainties in the estimates of GRACE-derived global mass balance by taking into account of corrections or errors of corrections not considered in previous studies. Finally, the contribution of global ice mass balance to the present-day sea level rise is estimated to be 1.55 ± 0.10 mm/yr from January 2003 to December 2012 using GRACE monthly gravity fields.

Preface

This report was prepared and submitted to the Graduate School of the Ohio State University as a dissertation in partial fulfillment of the requirements of the Ph.D. degree.

This research is partially funded by grants supported under NASA's Cryosphere program (NNX11AR47G and NNX10AG31G), Ocean Surface Topography Mission (OSTM) Program (JPL 1384376 and CU154-5322), Physical Oceanography Program (The Ohio State University's Climate, Water, and Carbon program (<http://cwc.osu.edu>), NASA Earth and Space Science Fellowship (NNX09AO50H) and Friends of Orton Hall (FOH) Award.

Acknowledgments

I would like to express my sincere gratitude to my Advisor, Dr. C.K. Shum, for his professional guidance, intellectual support and encouragement, all of which have made this research possible. I would also like to thank him for the patience and help during my entire stay at The Ohio State University. I wish to particularly thank Dr. Junyi Guo, who enriched me with invaluable experiences in both of the theoretical and technical aspects of my research topic. I appreciate his invaluable discussion and tireless help on various technical and programming issues related to GRACE data processing.

I would like to thank Dr. Christopher Jekeli and Dr. Ian Howat for serving as members of my PhD Dissertation Committee, and for their fruitful advice and comments that have improved the quality of the Dissertation.

I am thankful to Professor Douglas Alsdorf, Professor Ralph Von Frese, Professor Burkhard Schaffrin, and Professor Alan Saalfeld who are always willing to provide help and advice during my study. I acknowledge Professor Chungyen Kuo, National Chengkung University, Taiwan, for his collaboration and technical assistance on sea level data sets.

I enjoyed many fruitful discussions and friendship with my colleagues, including Zhenwei Huang, Kuo-Hsin Tseng, Hok Sum Fok, at the Division of Geodetic Science, School of Earth Sciences.

Table of Contents

Abstract	i
Preface	iii
Acknowledgments	iv
Chapter 1 Introduction	1
1.1 Global Sea Level Rise	1
1.2 Mass Balance of Global Ice Reservoirs	2
1.3 Measuring Mass Redistribution Using Satellite Gravimetry	5
1.4 Motivation for This Study	6
1.5 Dissertation Outlines	8
Chapter 2 GRACE Data Processing	9
2.1 Relationship Between Surface Mass and Gravity	9
2.2 Post-processing Techniques	12
2.2.1 Gaussian Smoothing	15
2.2.2 Decorrelation.....	17
2.2.3 Leakage Reduction	21
2.3 Uncertainty of GRACE mass estimates	24
Chapter 3 Uncovered Spurious Jumps in the GRACE De-aliasing Data	29
3.1 Introduction	29
3.2 Systematic Biases in the AOD1B Data	30
3.3 Potential Impacts of the Systematic Biases	35
3.4 Chapter Summary	37
Chapter 4 Glacier Mass Balance in High Mountain Asia	38
4.1 Introduction	38
4.2 Methods Summary	40
4.3 Main Uncertainty Sources	44
4.3.1 Lakes and Wetland	45
4.3.2 Precipitation.....	45
4.3.3 Hydrology Models.....	50
4.3.4 Spurious Jumps in GRACE Atmospheric De-aliasing Data	52
4.4 Glacier Mass Balance in HMA	55
4.5 Chapter Summary	64
Chapter 5 Mass Balance in Greenland	65
5.1 Introduction	65
5.2 Study Region	66
5.3 GRACE-determined mass changes	68
5.4 Surface Mass Balance	77
5.5 Results	80
Chapter 6 Antarctic Ice Mass Balance	85

6.1	Introduction.....	85
6.2	Ice Mass Balance Observed by GRACE.....	85
6.3	Antarctic Surface Mass Balance	96
6.4	Uncertainty Assessment	101
6.4.1	Potential GIA models error.....	101
6.4.2	AOD1B RL05 de-aliasing ocean model	102
6.4.3	Long-wavelength gravity signals	103
6.5	Results	108
Chapter 7	Conclusions	114
Bibliography.....		117
Appendix		130

Chapter 1 Introduction

1.1 Global Sea Level Rise

Sea level change is an important consequence of anthropogenic climate change, both for societies and for the environment. Current sea level rise potentially affects human populations (e.g., those live in coastal regions and on islands) and the natural environment (e.g., marine ecosystems) [Bindoff et al., 2007; Fischlin et al., 2007]. The 2007 Intergovernmental Panel for Climate Change (IPCC) Fourth Assessment Report (AR4) concluded that the warming of the climate system is unequivocal, and with high certainty that the effect of human activities since 1750 has resulted in global warming [IPCC, 2007]. The 20th century and present day sea level rise are recognized to be measurable using tide gauges since the last century and a half, and Earth-orbiting satellite altimetry missions over the past 2 decades [Shum and Kuo, 2011; 2013] (Figure 1.1). Global mean sea level rose 195mm during 1870~2004 [Church and White, 2006]. For past several decades, measurements show an average annual rise in sea level of 1.7 ± 0.3 mm/yr for the period from 1950 to 2009, with the satellite altimetry mission showing a rise of 3.3 ± 0.3 mm/yr from 1993 to 2009 (Figure 1.1), which shows a faster rate of increase than previously estimated [IPCC, 2007]. However, the discrepancy of the sea level rise estimate could be due to an accelerated sea level rise over the last three decades, or that the satellite estimate is contaminated by interannual or longer oceanic signals, primarily resulting from shorter records of satellite altimetry data.

Quantifying and understanding the causes of the rate of sea level rise remain challenging: the signal has a wide range of temporal and spatial scales resulting from complex interactions between various Earth-atmosphere-ocean-cryosphere-hydrosphere processes [Bindoff et al., 2007; Cazenave et al., 2010; Shum and Kuo, 2011]. Observed sea level rise has two main contributing facts, the first one is ocean volume change, or steric changes of the ocean, from ocean temperature and salinity changes as the ocean warms; the second one is total ocean mass changes driven by exchanges with water stored on land. By far the most important land storage is frozen in continental ice masses, which contain more than 90% of the Earth's fresh water resources. It is estimated that total melting of the Antarctic ice sheet, the Greenland ice sheet, and the mountain glaciers and ice caps would raise global sea level by over 70 m.

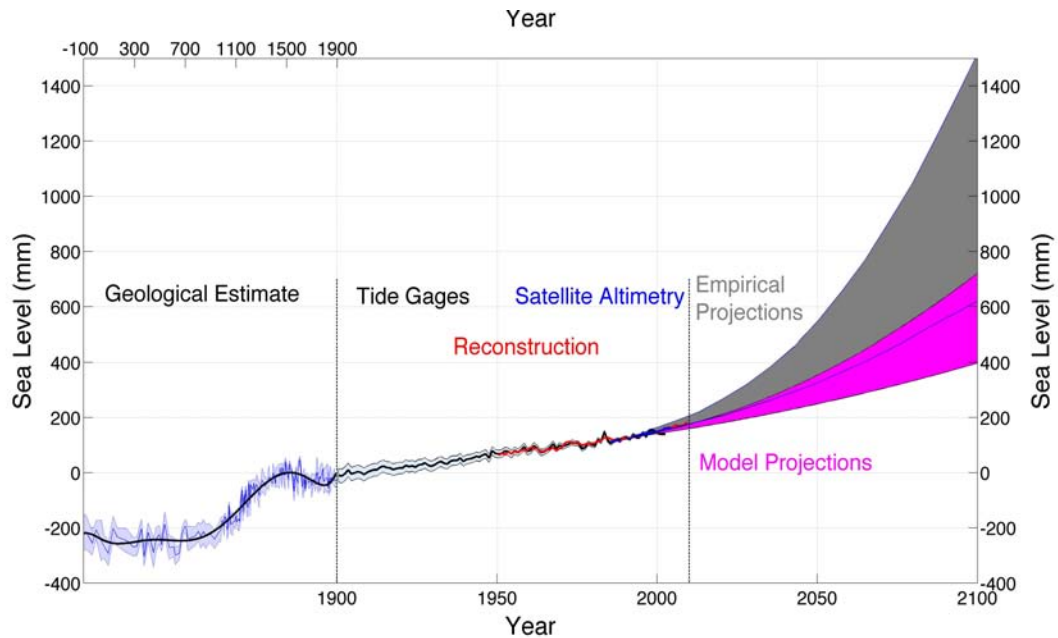


Figure 1.1 Global mean sea level changes: observation and prediction (from 100 BC to 2100 AD), updated from Shum and Kuo [2011].

The 2007 IPCC AR4 sea level assessment [Bindoff et al., 2007] has narrowed the gap between the observations and the geophysical causes of sea level rise as compared to the 2001 IPCC Third Assessment Report [Church et al., 2001]. However, the differences between observed ($1.8 \rightarrow 2.1 \text{ mm yr}^{-1}$), 1972–2008 [e.g., Church et al., 2011] and explained geophysical contributions to global sea level rise (summed to $1.42 \rightarrow 2.14 \text{ mm yr}^{-1}$) [Church et al., 2011] has an upper bound discrepancy of 0.7 mm yr^{-1} . This significant discrepancy is primarily attributable to the prevailing uncertainty of ice-sheet and mountain glacier mass balance estimates [Cazenave, 2006; Wingham et al., 1998, 2006; Shepherd and Wingham, 2007].

1.2 Mass Balance of Global Ice Reservoirs

Continental ice reservoirs contain over 90% of the Earth's freshwater, which play an important role to global climate changes and sea level rise. The temporal change in the mass of a glacier or ice sheet is usually called *ice mass balance*.

Common glaciological usage equates *mass balance* with the change in storage. The term *mass budget* is a synonym of mass balance. Actually mass budget is a more correct term than mass balance, but is used less often [Cogley et al., 2011]. Ice mass balance represents the difference between ice mass accumulation and ice mass loss over a stated span of time:

$$\Delta M = B = C + A = \int_{t_0}^{t_1} (\dot{C} + \dot{A}) dt \quad 1-1$$

where C is the sum of accumulation, A is the ablation (it is defined here as negative), and the symbol B appears most often in mass balance studies. Accumulation includes all processes that add to the mass of the ice system, of which the most important component is snowfall. On the other hand, ablation contains all processes that reduce the mass of the ice system, including melting, calving and sublimation. The mass balance can be positive or negative (or zero). For particular time period, if total accumulation exceeds total ablation, then the mass balance is positive. On the other hand, if accumulation is less than ablation, then the mass balance is negative. The term *mass imbalance* is used to describe the status of an ice system for $\Delta M \neq 0$. Note that the *mass balance* and *mass imbalance* are not opposite of each other. The term *mass imbalance* keeps its literal meaning, while *mass balance* is a glaciological term defined as change in ice mass.

Often, however, the most fitting interpretation is that the mass balance is a rate [Cogley et al., 2011]. And, mass balance is often treated as a rate in mass-balance studies, e.g., van den Broeke et al. [2009]. Cogley et al. [2011] also point out that whether to present the mass balance as a rate or not will depend on the context of the investigation. In this study we interpret mass balance as mass changes during the period 2003 ~ 2012 represented by the time derivative dM/dt .

Here, we generally introduce current mass change status of the Earth's major ice systems. The Antarctic and Greenland ice sheets together hold 33 million km^3 of ice, which can raise global sea level by over 70 m. Annual snowfall on the ice sheets is equivalent to 6.5 mm of sea level, hence only a small imbalance between snowfall and discharge of ice could be a major contributor to present-day sea level rise [Rignot and Thomas, 2002].

Greenland contains about 2.5 million km^3 or 10% of the total global ice mass, which is the second largest ice cap on Earth. Changes in Greenland ice mass balance have important consequences because, as the Antarctic ice sheet, they affect global sea levels and climate changes. Complete melting of Greenland ice sheet would raise global mean sea level by about 6.5 m, although it is unlikely to happen in the near future. Therefore, Greenland ice loss under the climate of global warming is of greatest concern. Recent studies have confirmed increasing ice melting over Greenland ice sheet since 1990s when satellite altimetry became a powerful tool, which can remotely sense ice sheet surface elevation changes (e.g., Johannessen et al., 2005). Aircraft laser-altimeter observations also show peripheral ice thinning in the 1990s at low elevations nearer the coast [Krabill et al, 2000]. During the past two decades, revolutionized satellite geodesy techniques also change the manner in which ice sheet mass balance is estimated, various measurements, derived from radar and laser altimetry, interferometry, imaging spectro-radiometer and gravimetry, supply at least 29 ice-sheet mass balance estimates since 1998, however, large discrepancy exists among those contemporary estimates which allow for a combined Greenland and Antarctic ice-sheet mass imbalance of between -676 and +69

Gt/yr [Shepherd et al., 2012], because each satellite method has its strengths and weaknesses. Even the same satellite mission can yield different mass balance estimates because of different post-processing techniques applied.

The Antarctic ice sheet holds more than 30 million km³ of ice, which is 90% of the world's ice or ~70% of global fresh water. Complete melting of the Antarctic ice sheet can raise global sea level by 60 m. Hence, quantifying Antarctic ice mass balance is of considerable societal importance, and is a key issue in understanding changes in global mean sea level rise.

Different from Greenland, the climate of which is strongly affected by nearby land processes and North Atlantic, Antarctica has a dominant influence on its own climate and on the surrounding ocean. With cold conditions even during the summer time, there is little surface melting of ice sheet, even near the coast and around its northern margins. Ice loss is primarily because of basal melting and iceberg calving from vast ice shelves distributed around much of the periphery of Antarctic continent [Rignot and Thomas, 2002]. Although it is plausible that Antarctic ice sheet contributed little to global mean sea level during the 20th century [Cazenave et al., 2006; Wingham et al., 2006], West Antarctica has received more attention over the last 30 years. Most of West Antarctica Ice Sheet (WAIS) is classified as a “marine ice sheet”, meaning that its bed lies well below sea level and its edges flow in floating ice shelves. Also since large parts of the WAIS sit on a bed slopes downward inland, the slope and low isostatic head mean that the WAIS is theoretically unstable. Glaciers flowing into the Amundsen Sea would float free from the bedrock, hence potentially easing resistive forces acting on upstream ice and thus leading to further glacier acceleration [Thomas et al., 2004]. A small retreat might destabilize the entire WAIS leading to rapid disintegration, prompting concerns over its stability in a warming climate. The Antarctic Peninsula ice sheet (APIS) occupies just 4% of the continent area, the ice mass is close to balance during the 1990s, however, there have been significant mass losses since then because of glacier acceleration in the wake of ice-shelf collapse and calving-front retreat [Pritchard et al., 2009; De Angelis and Skvarca, 2003; Cook et al., 2005]. The APIS now accounts for 25% of all mass loss from Antarctic regions that are in a state of negative mass balance [Shepherd et al., 2012].

Satellite geodesy provides most of the contemporary continent-wide observations for Antarctic ice sheet mass. Compared to Greenland, Antarctic ice sheet mass balance is even harder to estimate because it is far larger, more remote, and not well covered by most of existing satellites [Rignot and Thomas, 2002]. Antarctic ice-sheet contributed global sea level rise ranges from -0.12 to 0.17 mm/yr (assuming that 362 Gt of ice corresponds to 1 mm of sea level rise) based on previous studies using InSAR and satellite radar altimetry [Davis et al., 2005; Thomas et al., 2004; Wingham et al., 2006; Zwally et al., 2005].

Mountain glaciers and ice caps distinct from polar ice sheet have been significantly retreating, and contributing to global sea level. The IPCC 2007 AR4 concluded that the contribution of mountain glaciers and ice caps to sea level rise has been significantly higher than prior estimates: 0.32–0.68 mm/yr over the time span of 1962–2003 [Kaser et al., 2006; Lemke et al., 2007]. Besides glacier systems in Alaska, Patagonia and Canadian Arctic, which are reported losing large amount of water into oceans, another

important glacier system, which lacks publicly available *in situ* observations, is the glacier system in the High Mountain Asia (HMA), which includes Qinghai-Tibetan Plateau and its surroundings. The HMA contains about 120,163 km² of glacier-covered regions based on Randolph Glacier Inventory, version 3.0, ([Graham Cogley, Pers. com.]; and RGI, 3.0, <http://www.glims.org/RGI/>), representing significant water resources for people in that part of the world. The scientific question and the societal-relevant issue, including the controversy of whether the glaciers in the Himalayas are retreating or advancing, is the focus of the proposed investigation. The Tibetan Plateau contains the largest store of ice after Antarctic, Greenland, the Arctic, and is rightfully justified being called the *Third Pole*, and the *World Water Tower* [Qiu, 2008]. During the past half-century, it is claimed that 82% of the Plateau's glaciers have retreated, and 10% of the discontinuous and sporadic/isolated permafrost has thawed or degraded [Qiu, 2008].

1.3 Measuring Mass Redistribution Using Satellite Gravimetry

As described above, global ice mass loss plays an important role to present-day global sea level rise. However, to estimate and quantify annual amount of ice and snow melt along with the contribution of precipitation to discharge are all uncertain because of insufficient numbers of *in situ* measurements. Remote sensing techniques, such as InSAR and satellite radar/laser altimetry, can provide contemporary observations for elevation changes of ice sheets, glaciers and ice caps. However, these observations, while have significantly higher spatial resolution and other advantages than GRACE, are limited by factors including incomplete coverage, and unknown firn/ice density corrections.

The Gravity Recovery and Climate Experiment (GRACE) [Tapley et al., 2004] twin-satellite mission launched in March 2002 is measuring Earth's time-variable gravity field with unprecedented accuracy and temporal and spatial resolutions. The monthly GRACE measurements of Earth's gravity field provide accurate information on large-scale mass redistribution within the Earth system [Wahr et al., 1998]. A large variety of scientific problems in diverse disciplines have been studied using GRACE data, including ice mass balance of polar ice sheets and mountain glaciers, ocean bottom pressure and global sea level rise, hydrologic fluxes and earthquake induced seismic deformation [Velicogna et al., 2006; Chen et al., 2006; Jacob et al., 2012; Rodell et al., 2009; Chambers et al., 2004; Morison et al., 2012; Han et al., 2006].

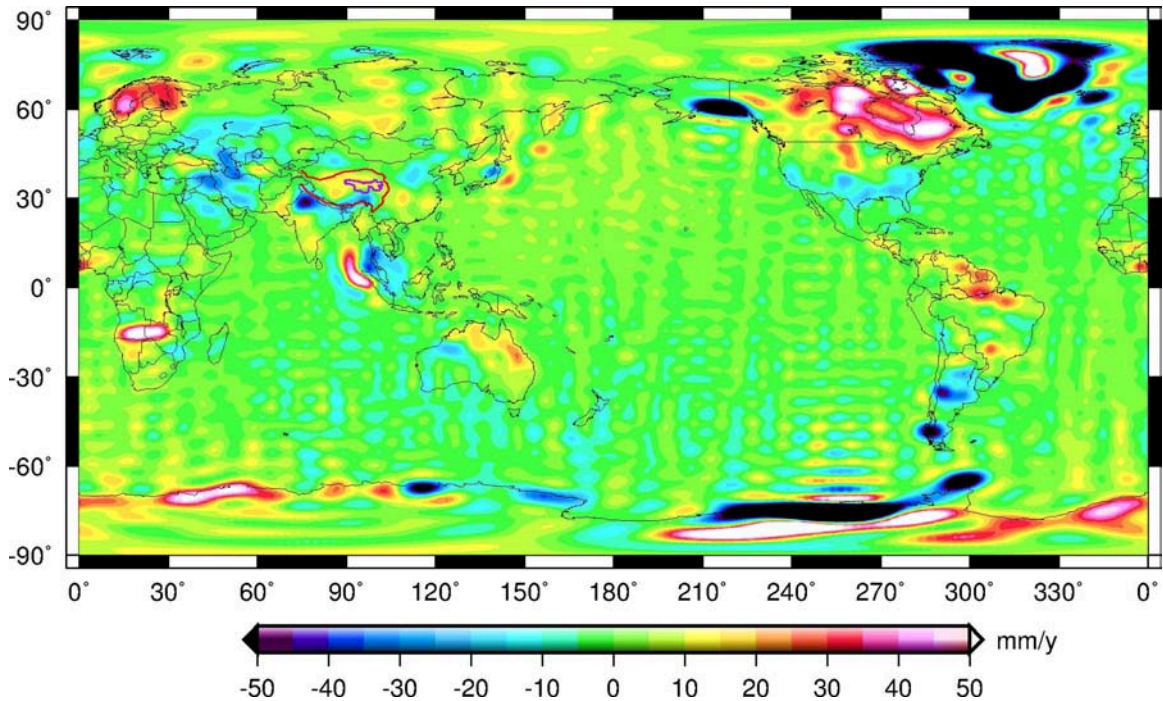


Figure 1.2 Trend map of surface mass changes within the Earth system, determined by GRACE monthly gravity fields (from Center for Space Research (CSR), Release 5) for period from January 2003 to December 2012, 150 km Gaussian smoothing [Jekeli, 1981; Guo et al., 2010] applied.

Figure 1.2 shows the trend map of mass changes within the Earth system, determined by GRACE monthly gravity fields for period from January 2003 to December 2012. From the trend map, we can see apparent mass loss in Greenland ice sheet, West Antarctic and Antarctic Peninsula, also for glaciers and ice caps in Canadian Arctic, Alaska, and Patagonia. Other geophysical processes are also observed by GRACE, e.g., the seismic deformation resulting from 2004 Sumatra earthquake, 2010 Chile earthquake and 2011 Japan earthquake; groundwater depletion in North India and inter-annual hydrology changes in Amazon and Africa.

As GRACE data accumulate, we can better estimate global ice mass balance and its contribution to present-day global mean sea level changes.

1.4 Motivation for This Study

GRACE provides unprecedented accuracy and temporal and spatial resolutions weighing global ice mass changes. Advantages of GRACE data include: 1) it provides regional mass changes without the need for interpolation; 2) it measures mass fluctuations directly without considering volume changes and density corrections; 3) it samples ice mass changes monthly [Shepherd et al., 2012]. However, a key challenge is to discriminate ice mass fluctuations from other geophysical causes.

What GRACE senses is the relative changes of total mass stored at all levels as a function of time [Rignot et al., 2011]. For polar ice sheets and glaciers, GRACE

observations (after correcting for non-ice mass change effect) mainly represent ice mass balance defined in Eq. 1-1. For other regions on the land, mass fluctuations are mainly caused by hydrologic water redistribution [Wahr et al, 1998]. Hydrologic mass balance equation has a similar expression as Eq. 1-1. Mass budget for a given area equates the total water storage change, $H(t)$, to the summed differences between precipitation, $P(t)$, evapotranspiration, $ET(t)$, and net water inflows and outflows, $Q(t)$ [Alsdorf et al., 2010]; that is,

$$H(t) = \int [P(t) - ET(t) - Q(t)] dt \quad 1-2$$

For glacier systems located in these regions, e.g. HMA, Alaska and Patagonia, hydrologic contribution to GRACE-derived mass changes has to be removed for the purpose of accurate estimation of glacier mass balance.

For Antarctic ice sheet (AIS), the other non-ice geophysical cause include the Glacial Isostatic Adjustment (GIA) process [Peltier, 2004], which manifests in the form of uplift or subsidence of subglacial topography and introduces considerable uncertainty (up to 130 Gt/yr) into ice-sheet mass balance estimates determined by GRACE, when different GIA models are used for correction [Shepherd et al., 2012]. Earlier estimates from Velicogna [2009] shows mass balance for AIS is -143 ± 73 Gt/yr during the period from 2002 to 2009, while Chen et al. [2009] estimated a range between -190 ± 77 Gt/yr and -250 Gt/yr (2002-2009) depending on different GIA model. Since 2012, published estimates intended to give much less negative mass balance values by using two new GIA models (W12a [Whitehouse et al., 2012] and the updated IJ05_R02 [Ivins et al., 2013]). King et al. [2012] estimated a continent-wide ice mass change of -69 ± 18 Gt/yr (from August 2002 to December 2010) by using W12a GIA model; and reconciled estimates from Shepherd et al. [2012] show Antarctic ice sheet changed in mass by -81 ± 33 Gt/yr (from January 2003 to December 2010) based on W12a and IJ05_R2 models. Velicogna and Wahr [2013] followed this trend and reported changes of -83 ± 49 Gt/yr (from January 2003 to November 2012) based on IJ05_R2 model applied. On the other hand, Chen et al. [2013] remained their previous estimates and reported Antarctic rate of -180 ± 94 Gt/yr (from 2005 to 2011). Estimates of mass balance of Greenland ice sheet are relatively not affected by GIA corrections [Huang et al., 2013], discrepancy still exists for previously published results because of different post-processing techniques applied. Unlike estimates of Antarctic ice mass balance that highly depend on GIA correction applied, hydrologic mass change is the main source of largest uncertainties estimating glacier mass balance over HMA. Published estimates of HMA ice loss rate range from -4 ± 20 Gt/yr (from January 2003 to December 2010) to -47 ± 12 Gt/yr (from 2003 to 2009) [[Jacob et al., 2012; Gardner et al., 2013; Matsuo and Heki, 2010].

In this study, we aim to produce mass balance estimates and the associated uncertainty for the world's ice sheets, major glacier and ice cap systems using GRACE gravimetry data. We will conduct an elaborate error analysis and compare the solutions with other available data sets, including *in situ* data and surface mass balance estimates,

towards a quantification of the contribution of global ice reservoirs to the present-day sea level rise.

1.5 Dissertation Outlines

Chapter 2 reviews the basis of relation between surface mass redistributions and time-variable satellite gravity measurements, and of GRACE data post-processing techniques.

Chapter 3 discusses the revealing of two uncovered spurious jumps in the GRACE de-aliasing data products, and analyzes their potential contaminations to glacier ice mass estimates determined by GRACE.

Chapter 4 devotes to estimate and quantify glacier mass loss in High Mountain Asia during January 2003 and December 2011, and its uncertainty.

Chapter 5 estimates mass changes of the ice sheet and glaciers (January 2003 ~ December 2012) using GRACE over the Greenland and Canadian Arctic, the results of mass changes over Alaska and Patagonia glaciers are also included at the end of this chapter.

Chapter 6 examines the mass balance of Antarctic ice sheet, also determines the sources of uncertainties, and quantifies their corresponding contributions to the estimates of mass balance over AIS determined by GRACE.

Chapter 7 concludes and proposes some future work.

Chapter 2 GRACE Data Processing

2.1 Relationship Between Surface Mass and Gravity

The application using GRACE observed time-variable gravity fields to estimate mass transport and redistribution on or within the Earth was first illustrated by Wahr et al. [1998].

Geoid, the equipotential surface that closely approximates mean sea level, is commonly used to describe the Earth's global gravity field, and it is usual to expand the geoid shape N as a sum of spherical harmonic (or Stokes') coefficients:

$$N(\theta, \phi) = a \sum_{l=0}^{\infty} \sum_{m=0}^l \tilde{P}_{lm}(\cos\theta) (C_{lm} \cos(m\phi) + S_{lm} \sin(m\phi)) \quad 2-1$$

where a is the mean radius of the Earth, θ and ϕ are colatitude and longitude, C_{lm} and S_{lm} are the (normalized) spherical harmonic coefficients and l and m are integers such that $0 \leq m \leq l$, $l \geq 0$. \tilde{P}_{lm} is fully-normalized associated Legendre function of the first kind:

$$\tilde{P}_{lm}(x) = N_{lm} \times P_{lm}(x) \quad 2-2$$

where $N_{lm} = \sqrt{(2 - \delta_{m0})(2l + 1) \frac{(l - m)!}{(l + m)!}}$, and the general form of associated Legendre function:

$$\tilde{P}_{lm}(x) = (-1)^m (1 - x^2)^{\frac{m}{2}} \frac{d^m}{dx^m} P_l(x) \quad 2-3$$

is from the Legendre function:

$$P_l(x) = \frac{1}{2^l l!} \frac{d^l}{dx^l} (x^2 - 1)^l \quad 2-4$$

What the GRACE satellite monthly solutions supply are numerical values of the C_{lm} and S_{lm} completed to degree and order (i.e., l and m) of 60.

Time-variable changes in the geoid ΔN , which represent either the geoid change from one time to another or the difference between N at one time and a reference static

geoid, are caused by mass density redistribution in the Earth. Hence, the time-dependent change in spherical harmonic coefficients ΔC_{lm} and ΔS_{lm} which result in ΔN can be related to the density redistribution $\Delta\rho(r,\theta,\phi)$ according to Chao and Gross [1987]:

$$\begin{Bmatrix} \Delta C_{lm} \\ \Delta S_{lm} \end{Bmatrix} = \frac{3}{4\pi a \rho_{ave} (2l+1)} \int \Delta\rho(r,\theta,\phi) \tilde{P}_{lm}(\cos\theta) \times \left(\frac{r}{a}\right)^{l+2} \begin{Bmatrix} \cos(m\phi) \\ \sin(m\phi) \end{Bmatrix} \sin\theta d\theta d\phi dr \quad 2-5$$

where $\rho_{ave} = 5517 \text{ kg/m}^3$ is the average density of the Earth.

The spherical harmonic coefficients are simply normalized multipoles of the Earth's density redistribution. The linear inversion of above equation is how to get $\Delta\rho(r,\theta,\phi)$ given the geoid change in the form of ΔC_{lm} and ΔS_{lm} . However, the well-known non-uniqueness of this gravitational inversion problem states that the external gravity field, even if completely and exactly known, cannot uniquely determine the density distribution of the body that produces the gravity field because of the degree of knowledge deficiency. On the other hand, the inversion solution to the surface density distribution is unique for a 2-D spherical shell without the radial dependence [Chao, 2005]. The 2-D inversion with uniqueness hence has important implications here for recovery of surface mass redistribution from the time-variable gravity signals that originate from the Earth's surface. Hence, the Earth's surface can be approximated as a spherical shell, supposing $\Delta\rho$ is concentrated in a thin layer of thickness H. For actual geophysical situation, this layer must be thick enough to include atmosphere, ice caps, ocean, and terrestrial water storage with significant mass fluctuations.

Surface density (i.e. mass/area), $\Delta\sigma$, is defined as the radial integral of $\Delta\rho$ through this thin layer:

$$\Delta\sigma(\theta,\phi) = \int_{\text{thin layer}} \Delta\rho(r,\theta,\phi) dr \quad 2-6$$

Under the current status of GRACE mission, the monthly gravity field solutions are commonly truncated to degrees $l < L_{\max} = 60$, which most of the recoverable time-variable gravity signals are concentrated. Suppose H is thin enough that $(L_{\max} + 2)H/a \ll 1$, then $(r/a)^{l+2} \approx 1$, thus Eq. 2-5 reduces to

$$\begin{Bmatrix} \Delta C_{lm} \\ \Delta S_{lm} \end{Bmatrix}_{\text{surface mass}} = \frac{3}{4\pi a \rho_{ave} (2l+1)} \int \Delta\sigma(\theta,\phi) \tilde{P}_{lm}(\cos\theta) \begin{Bmatrix} \cos(m\phi) \\ \sin(m\phi) \end{Bmatrix} \sin\theta d\theta d\phi \quad 2-7$$

The equation above describes the direct contribution to the geoid from the gravitational attraction of the surface mass redistribution. Redistributed surface mass also loads and deform the underlying solid Earth, which causes an additional contribution to geoid:

$$\begin{Bmatrix} \Delta C_{lm} \\ \Delta S_{lm} \end{Bmatrix}_{\text{solid Earth}} = \frac{3k_l}{4\pi a \rho_{ave} (2l+1)} \int \Delta\sigma(\theta, \phi) \tilde{P}_{lm}(\cos\theta) \begin{Bmatrix} \cos(m\phi) \\ \sin(m\phi) \end{Bmatrix} \sin\theta d\theta d\phi \quad 2-8$$

where k_l is the load deformation Love number of degree l [Munk and Macdonald, 1960].

The total geoid change thus can be expressed with the sum of Eq. 2-7 and Eq. 2-8:

$$\begin{Bmatrix} \Delta C_{lm} \\ \Delta S_{lm} \end{Bmatrix} = \begin{Bmatrix} \Delta C_{lm} \\ \Delta S_{lm} \end{Bmatrix}_{\text{solid Earth}} + \begin{Bmatrix} \Delta C_{lm} \\ \Delta S_{lm} \end{Bmatrix}_{\text{surface mass}} \quad 2-9$$

To relate ΔC_{lm} and ΔS_{lm} with $\Delta\sigma$ in a more compact form, we expand $\Delta\sigma$ as:

$$\Delta\sigma(\theta, \phi) = a\rho_w \sum_{l=0}^{\infty} \sum_{m=0}^l \tilde{P}_{lm}(\cos\theta) \left(\Delta\hat{C}_{lm} \cos(m\phi) + \Delta\hat{S}_{lm} \sin(m\phi) \right) \quad 2-10$$

The density of water ρ_w is used here so that ΔC_{lm} and ΔS_{lm} are dimensionless.

With the normalized \tilde{P}_{lm} which satisfies that:

$$\int_0^\pi \tilde{P}_{lm}^2(\cos\theta) \sin\theta d\theta = 2(2 - \delta_{m,0}) \quad 2-11$$

we have:

$$\begin{Bmatrix} \Delta\hat{C}_{lm} \\ \Delta\hat{S}_{lm} \end{Bmatrix} = \frac{1}{4\pi a \rho_w} \int_0^{2\pi} d\phi \int_0^\pi \Delta\sigma(\theta, \phi) \tilde{P}_{lm}(\cos\theta) \begin{Bmatrix} \cos(m\phi) \\ \sin(m\phi) \end{Bmatrix} \sin\theta d\theta \quad 2-12$$

We thus can find the relation between $(\Delta C_{lm}, \Delta S_{lm})$ and $(\Delta\hat{C}_{lm}, \Delta\hat{S}_{lm})$:

$$\begin{Bmatrix} \Delta C_{lm} \\ \Delta S_{lm} \end{Bmatrix} = \frac{3\rho_w}{\rho_{ave}} \frac{1+k_l}{2l+1} \begin{Bmatrix} \Delta\hat{C}_{lm} \\ \Delta\hat{S}_{lm} \end{Bmatrix} \quad 2-13$$

Or, conversely,

$$\begin{Bmatrix} \Delta\hat{C}_{lm} \\ \Delta\hat{S}_{lm} \end{Bmatrix} = \frac{\rho_{ave}}{\rho_w} \frac{1+2l}{1+k_l} \begin{Bmatrix} \Delta C_{lm} \\ \Delta S_{lm} \end{Bmatrix} \quad 2-14$$

And, finally, we can find the surface mass density change from changes $(\Delta C_{lm}, \Delta S_{lm})$ supplied by GRACE monthly gravity fields:

$$\Delta\sigma(\theta,\phi) = \frac{a\rho_{ave}}{3} \sum_{l=0}^{\infty} \sum_{m=0}^l \frac{2l+1}{1+k_l} \tilde{P}_{lm}(\cos\theta) (\Delta C_{lm} \cos(m\phi) + \Delta S_{lm} \sin(m\phi)) \quad 2-15$$

The equation above is more commonly used with the surface mass density expressed in equivalent water height (EWH):

$$\Delta h(\theta,\phi) = \frac{a\rho_{ave}}{3\rho_w} \sum_{l=0}^{\infty} \sum_{m=0}^l \frac{2l+1}{1+k_l} \tilde{P}_{lm}(\cos\theta) (\Delta C_{lm} \cos(m\phi) + \Delta S_{lm} \sin(m\phi)) \quad 2-16$$

2.2 Post-processing Techniques

Ideally, time-dependent global surface mass redistribution of the Earth could be mapped from GRACE observed monthly gravity fields using the Eq. 2-16 in the section above. A randomly picked monthly solution (March 2005) from University of Texas at Austin Center for Space Research (UTCSR) is shown in Figure 2.1. The figure represent the EWH changes of Mar 2005 corresponding to the temporal mean of 104 monthly solutions spanning January 2003 to December 2011.

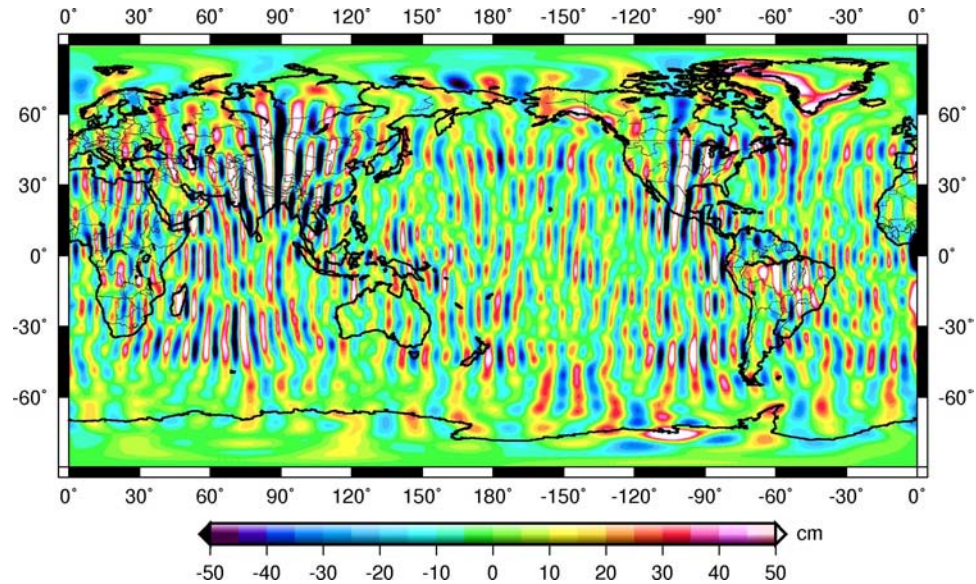


Figure 2.1 GRACE determined monthly map (March 2005) of surface mass anomaly in EWH, no smoothing or filtering applied.

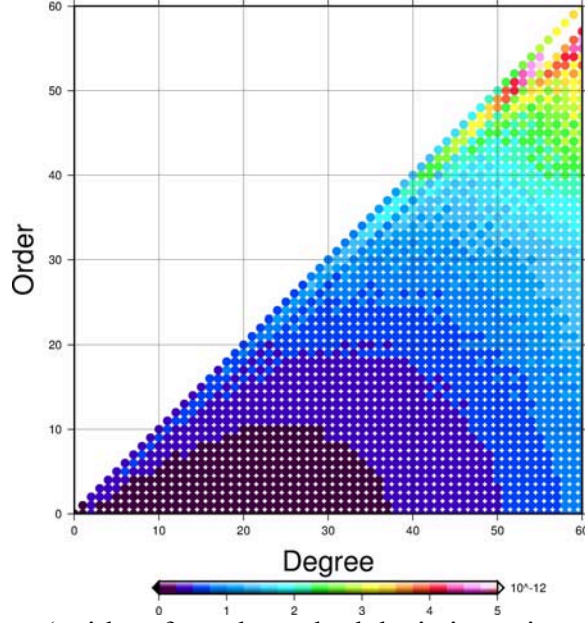


Figure 2.2 Error pattern (unitless formal standard deviations given in GRACE monthly Stokes' coefficients) of C_{lm} terms of March 2005 gravity field.

We can see from the figure that strong spurious north-south stripes dominate the map, which indicate that the GRACE gravitational solutions have large systematic errors (other months also show similar error pattern). By examining the standard deviations (SD) of the spherical harmonic coefficients, we can see the errors increases with increasing degrees and orders (Fig. 2.2). With ΔC_{lm} and ΔS_{lm} multiplied by terms with large $(2l+1)$ values in Eq. 2-16, the errors from high degree spherical harmonic coefficients can make large contributions to the sum in Eq. 2-16. The effect can also be seen in the GRACE monthly solutions by plotting the degree amplitudes (or square root of degree variance, square root of power per degree l), which is defined as:

$$c_l = \sqrt{\sum_{m=0}^l (\Delta C_{lm}^2 + \Delta S_{lm}^2)} \quad \text{in terms of unitless coefficients} \quad 2-17$$

or:

$$c_l(\Delta h) = \frac{a\rho_{ave}}{3\rho_w} \frac{2l+1}{1+k_l} \sqrt{\sum_{m=0}^l (\Delta C_{lm}^2 + \Delta S_{lm}^2)} \quad \text{in terms of EWH (m)} \quad 2-18$$

Figure 2.3 shows the degree amplitude spectrum, in term of unitless coefficients, for one month of GRACE RL05 gravity field solution (March 2005). The GRACE RL05 spectrum decreases until about degree 30, then increase after that. Swenson and Wahr

[2011] compared the degree amplitude spectrum of the CSR RL04 gravity field solutions to the spectrum derived from a simulated global surface mass signal from the Community Land Model version 4 (CLM). From the comparison (Figure 2.3), they infer that the large amplitudes of the high degree coefficients are largely the result of errors in the GRACE solutions.

Error analysis based on previous studies shows the GRACE solutions contain both random errors that increase as functions of spectral degree [Wahr et al., 2006] and systematic errors that are correlated with a particular spectral order [Swenson and Wahr, 2006]. To reduce the effects of the errors of the GRACE solutions, and thereby recover GRACE-observed surface mass density with improved signal-to-noise ratio, post-processing techniques are necessarily employed to GRACE original spherical harmonic coefficients. Here, we show three commonly used methods for GRACE data post-processing: 1) isotropic Gaussian smoothing, 2) decorrelation technique, and 3) leakage reduction.

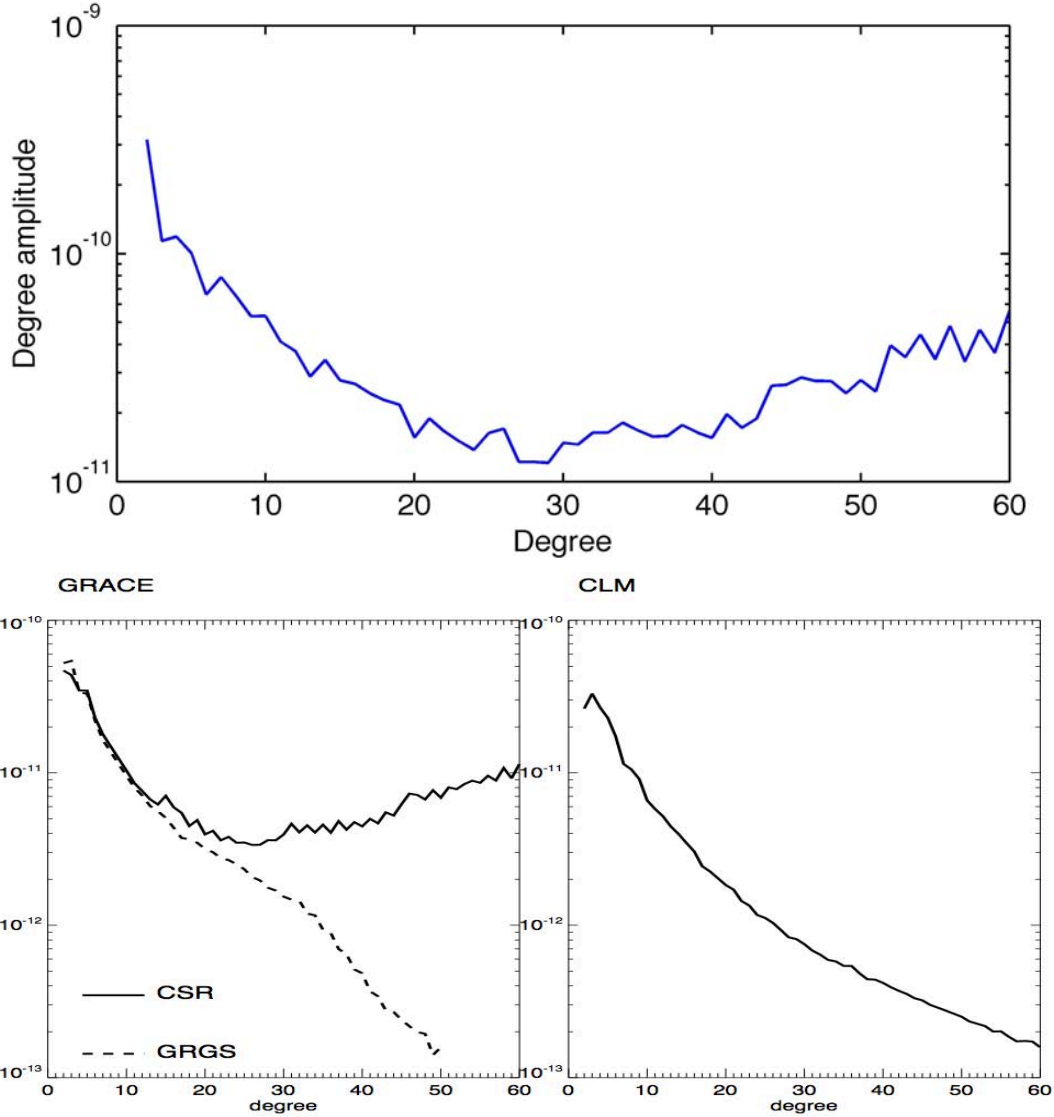


Figure 2.3 TOP: Error pattern (unitless formal standard deviations given in GRACE monthly Stokes' coefficients) of C_{lm} terms of March 2005 gravity field; BOTTOM: Left) GRACE degree amplitude spectrum for CSR gravity fields, Right) degree amplitude spectrum for the synthetic gravity field derived from a CLM simulation. (The bottom panel is from Swenson and Wahr [2011]).

2.2.1 Gaussian Smoothing

The idea of using Gaussian averaging function was developed by Jekeli [1981] for constructing spatial averages to compensate for poorly determined, short-wavelength spherical harmonic coefficients. By applying a Gaussian averaging function W , which is defined to be depending only on the angle ψ between points (θ, ϕ) and (θ', ϕ') , where $\cos \psi = \cos \theta \cos \theta' + \sin \theta \sin \theta' \cos(\phi - \phi')$, then we have the spatial average of the EWH:

$$\overline{\Delta h}(\theta, \phi) = \frac{2\pi a \rho_{ave}}{3\rho_w} \sum_{l=0}^{\infty} \sum_{m=0}^l \frac{2l+1}{1+k_l} W_l \tilde{P}_{lm}(\cos\theta) (\Delta C_{lm} \cos(m\phi) + \Delta S_{lm} \sin(m\phi)) \quad 2-19$$

where $W_l = \int_0^\pi W(\psi) P_l(\cos\psi) \sin\psi d\psi$, and where $P_l = \tilde{P}_{lm=0} / \sqrt{2l+1}$ are the Legendre polynomials.

Wahr et al. [1998] adopted Jekeli's Gaussian average function and normalize it so that the global integral of W is 1:

$$W(\psi) = \frac{b}{2\pi} \frac{\exp[-b(1-\cos\psi)]}{1-e^{-2b}} \quad 2-20$$

$$b = \frac{\ln(2)}{1-\cos(r/a)}$$

where r is the average radius which is the distance on the Earth's surface at which W drops to half its value at $\psi = 0$. The coefficients W_l can be computed with its recursion relations:

$$W_0 = \frac{1}{2\pi}$$

$$W_1 = \frac{1}{2\pi} \left[\frac{1+e^{-2b}}{1-e^{-2b}} - \frac{1}{b} \right] \quad 2-21$$

$$W_{l+1} = -\frac{2l+1}{b} W_l + W_{l-1}$$

Figure 2.4 shows the W_l for the average radius $r = 200, 250, 300, 350, 400, 450, 500, 600, 800$ km from right to left.

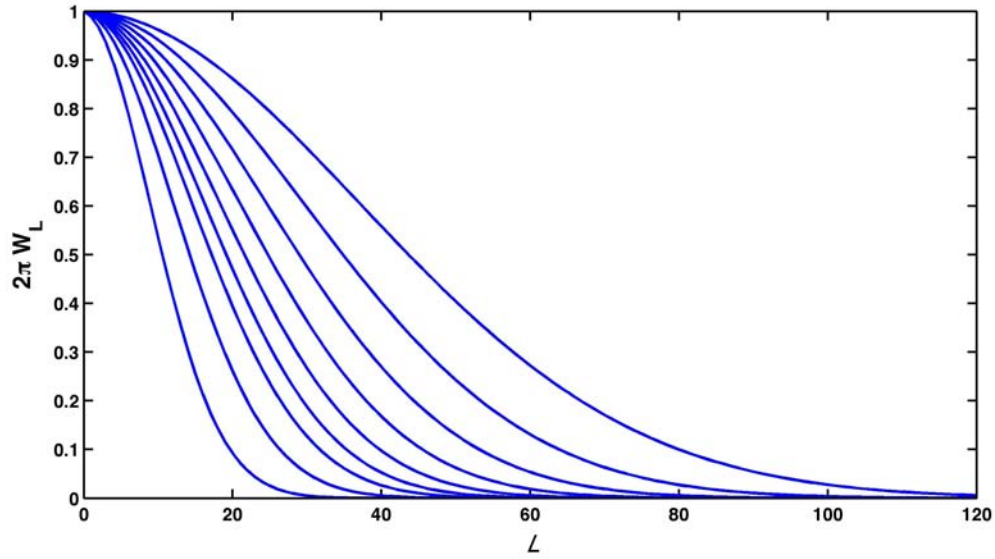


Figure 2.4 W_l for the average radius $r = 200, 250, 300, 350, 400, 450, 500, 600, 800$ km from right to left.

2.2.2 Decorrelation

As Figure 2.1 depicts, the north-south stripes show strong spatial correlations, which indicate corresponding correlations in the gravity field coefficients, Swenson and Wahr [2006] examined the spectral signature of the correlated errors, and revealed that certain spherical harmonic coefficients of the GRACE gravity field, at greater orders, are correlated. More specifically, the spherical harmonic coefficients of the same order (begins at approximately order $m = 8$) and the same parity in degrees are correlated with each other [Duan et al., 2009].

The correlated systematic errors can be reduced by applying high-passing filter designed to remove correlations between spectral degrees of like parity. The process is often referred to as decorrelation, or destriping. Swenson and Wahr [2006] first derived an empirical moving window filter to isolate and remove smoothly varying coefficients of like parity, by smoothing the spherical harmonic coefficients for particular order with a quadratic polynomial in a moving window of width w centered about degree l . The smoothed spherical harmonic coefficients can be expressed as:

$$\Delta C_{lm}^s = \sum_{i=0}^p Q_{lm}^i l^i \quad 2-22$$

where Q_{lm}^i is the degree i coefficient of the polynomial fit and p is the order of the polynomial, similar expressions are applied for ΔS_{lm}^s .

The polynomial coefficients Q_{lm}^i are given by least square fitting:

$$Q_{lm}^i = \sum_{j=0}^P \sum_{\substack{n=1-w/2 \\ n: \text{ even or odd}}}^{l+w/2} L_{ij}^{-1} n^j \Delta C_{nm} \quad 2-23$$

where

$$L_{ij} = \sum_{\substack{n=1-w/2 \\ n: \text{ even or odd}}}^{l+w/2} n^i n^j \quad 2-24$$

The summation applies only to terms of the same parity as l , i.e., if l is odd, then only odd degrees are summed, similar rule applies to the even degrees when l is even. By combining equations above, one can express each smoothed spherical harmonic coefficient, ΔC_{lm}^s , as:

$$\Delta C_{lm}^s = \sum_{\substack{n=1-w/2 \\ n: \text{ even or odd}}}^{l+w/2} W_{lmn} \Delta C_{nm} \quad 2-25$$

with the filter, W_{lmn} , defined by:

$$W_{lmn} = \sum_{i=0}^P \sum_j^P L_{ij}^{-1} n^j l^i \quad 2-26$$

To summarize the approach of Swenson and Wahr [2006] described above, we see the correlated part of the GRACE monthly spherical harmonic coefficients is computed and removed by fitting $\Delta C_{l-2\alpha}^m, \dots, \Delta C_{l-2}^m, \Delta C_l^m, \Delta C_{l+2}^m, \dots, \Delta C_{l+2\alpha}^m$, with $\alpha = (w-1)/2$, using a quadratic polynomial. The window width w was not provided in *Swenson and Wahr* [2006], but explicitly give by Duan et al. [2009]:

$$w = \max(Ae^{-m/K} + 1, 5) \quad 2-27$$

where A and K are empirically chosen to be 30 and 15 respectively by Swenson and Wahr [2006] based on a trial-and-error procedure. Since the coefficients are fitted with a quadratic polynomial, the window width should be greater than 3 to ensure certain information is retained after filtering, also w should be a odd integer based on the definition above, thus the minimum width should be 5. For $l < m + \alpha$ and $l > L_{\max} - \alpha$, (C_{lm}, S_{lm}) are not located at the center of the window. In this case, w number of coefficients of the same parity as l , with lowest or highest degrees, are used for the polynomial fitting.

Since the polynomial fitting parameters are basically empirically determined, different decorrelation schemes for different purposes were applied and studied after Swenson and Wahr [2006] [e.g. Chambers, 2006; Chen et al., 2007; Schrama et al., 2007; Wouters and Schrama, 2007; Davis et al., 2008; Kusche, 2007; Klees et al., 2008; and Duan et al., 2009]. Here, we choose to apply the decorrelation technique developed by Duan et al. [2009] for our study.

Compared to other approaches, Duan et al. [2009] use the standard deviations of the spherical harmonic coefficients from the GRACE data products as the criteria for choosing decorrelation parameters. This approach keeps unchanged a portion of lower degree-order spherical harmonic coefficients with smaller standard deviation, and decorrelates the rest using a quadratic polynomial moving window filtering. The window width decreases as the standard deviation increases, which allows filtering of the coefficients of different degree/order with different strength.

As we already showed in Figure 2.2, the standard deviations strongly depend on both the degree and order, and the near-sectorial coefficients show apparently larger standard deviations. Based on this error pattern, we keep a lower degree/order portion of the Stokes' coefficients unchanged/unfiltered, black curves in Figure 2. 5 show the boundaries for unchanged portions that are defined as:

$$l = l_0 + \beta m^r \quad 2-28$$

The curve specified by chosen parameters follows a contour of the error pattern of the coefficients. r was set to be 3.5 after a large number of trial-and-error experiments. The values of l_0 and β are defined by the two ends of the curve, i.e. the one with $m=0$ and the other with $m=l$. The end-point pairs for the three black curves in Figure 2.5 are [(20,0), (10,10)], [(35,0), (15, 15)], and [(45,0), (20,20)] respectively from left to right. Similar to the moving window filtering in Swenson and Wahr [2006], Duan et al. [2009] used the quadratic polynomial, but with adjustable window width based on the error pattern. The larger the stand deviation is, the smaller the window width is, which ensure stronger filtering applied. Different from Swenson and Wahr [2006] which define window width depending only order m , the window width is given by:

$$w = \max \left(A e^{\frac{[(1-\gamma)m^p + \gamma l^p]^{1/p}}{K}} + 1, 5 \right) \quad 2-29$$

The window width defined above depends on both degree l and order m , with empirically determined parameters γ and p , the window width has a pattern similar to error pattern in Figure 2.2. According to Duan et al. [2009], γ and p are set to be 0.1 and 3 respectively, with the same $A=30$ as Swenson et al. [2006], the window width is defined by K alone, Figure 2.5 shows the window width pattern with $K=10$ and 15 respectively, we can see that larger K defines corresponding larger window widths.

Figure 2.6 shows degree amplitude spectrums for smoothed and filtered monthly gravity field anomaly as for Figure 2.3. We can see high degree noise/signal are suppressed by Gaussian smoothing and de-correlation techniques, these are more apparent in spatial domain.

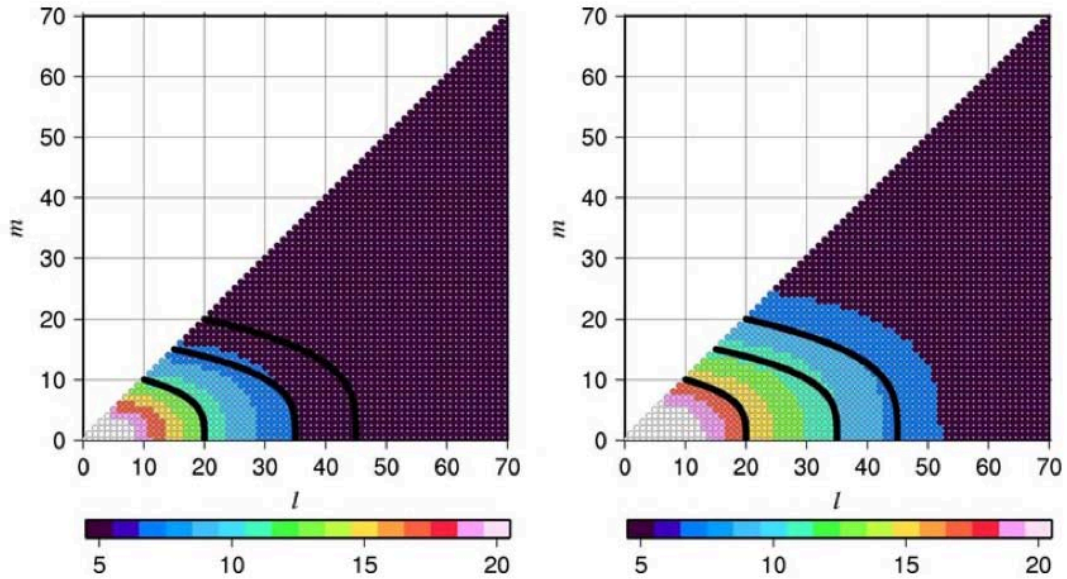


Figure 2.5 Window width as function of l and m with $K = 10$ (Left) and $K = 15$ (Right).

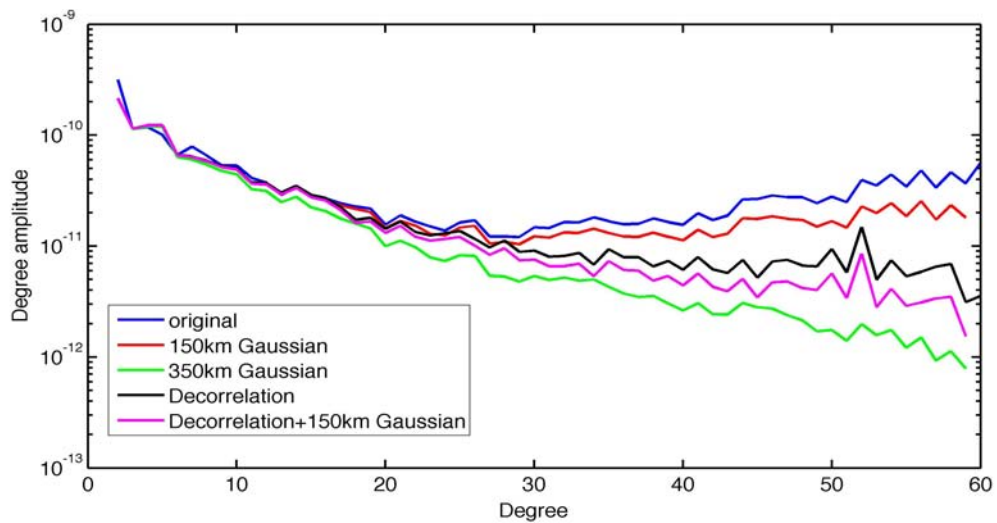


Figure 2.6 Degree amplitude spectrums for smoothed and filtered monthly gravity field anomaly (March 2005).

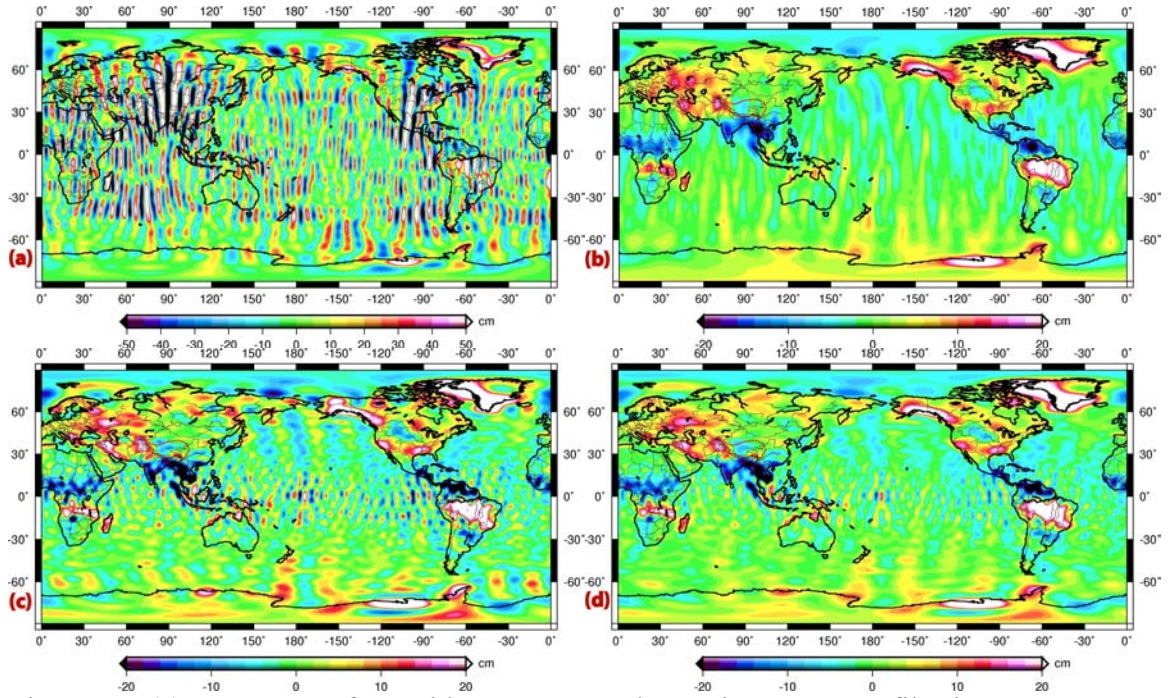


Figure 2.7 (a) same map of monthly mass anomaly as Figure 2.1, no filtering or smoothing applied; (b) 350 km Gaussian smoothing applied; (c) de-striped mass anomaly map; (d) 150 km Gaussian smoothing applied after de-striping.

2.2.3 Leakage Reduction

We introduced the Gaussian smoothing technique in the section above. From Figure 2.7b we can see that smoothing would attenuate signal magnitude on land for GRACE data. The attenuation represents the loss of a part of the signal on land that is added to the smoothed value over ocean, i.e. the signal on land is leaked in the coastal ocean [Guo et al., 2010], especially for Greenland and Antarctic ice sheets. To get accurate estimate of mass changes on land, leaked signals should be recovered. Wahr et al. [1998] present an iterative algorithm to eliminate the effect of signal leakage. Some studies applied empirical “scaling factor” to correct signal leakage while estimating regional mass changes [e.g., Valicogna and Wahr, 2006, 2013; Baur et al., 2009]. Chen et al. [2006, 2013] used a kind of “trial-and-error” forward modeling approach to estimate total mass changes of ice sheet system.

In this study, we apply a leakage recovery technique according to Guo et al. [2010]. The algorithm is based on two assumptions: 1) most of stripes and high-degree noises are removed by appropriate smoothing/decorrelation techniques; 2) signal over ocean is reduced to very small magnitude in GRACE monthly gravity fields by taking into account of de-aliasing product during GRACE data processing (see Chapter 3 for more detail about GRACE de-aliasing product). Thus, the contribution from signals over coastal ocean can be neglected in the results of smoothed mass changes on land. The leakage signals can be recovered by re-scaling the Gaussian-smoothed mass changes so that the final results are equal to that obtained by a weighted averaging of land signals alone. The result of this approach is actually equivalent to that of the regional filter for

land alone [Wahr et al., 1998], while avoiding the side lobe effects [Jekeli, 1981; Wahr et al., 1998].

Before introducing the leakage reduction algorithm, we rewrite the Gaussian smoothing equations of Eq. 2-19~2-21. We write the Gaussian function in the form of:

$$G(\psi) = \exp\left(-\frac{\psi^2}{2\sigma_\psi^2}\right) \quad 2-30$$

where σ_ψ is the standard deviation related to the smoothing radius r_ψ in the form of:

$$\sigma_\psi = \frac{r_\psi}{\sqrt{2\ln(2)}} \quad 2-31$$

For the classical isotropic Gaussian filter described above, the smoothed value of $h(\theta, \phi)$ in Eq. 2-19 at the point (θ', ϕ') is defined as:

$$\bar{h}(\theta', \phi') = Y^{-1} \int_0^\pi d\theta \int_0^{2\pi} h(\theta, \phi) G(\psi) \sin\theta d\phi \quad 2-32$$

where:

$$Y = \int_0^\pi d\theta \int_0^{2\pi} G(\psi) \sin\theta d\phi \quad 2-33$$

which is in fact independent of (θ', ϕ') .

The discrete form of Eq. 2-32 can be expressed as:

$$\bar{h}(\theta'_j, \phi'_k) = Y^{-1}(\theta'_j, \phi'_k) \sum_{(\theta_\alpha, \phi_\beta) \in S} h(\theta_\alpha, \phi_\beta) G(\psi_{jk}^{\alpha\beta}) \sin\theta_\alpha \quad 2-34$$

$$Y(\theta'_j, \phi'_k) = \sum_{(\theta_\alpha, \phi_\beta) \in S} G(\psi_{jk}^{\alpha\beta}) \sin\theta_\alpha \quad 2-35$$

where:

$$S = \begin{cases} L, & \text{for } (\theta, \phi) \text{ is over land} \\ O, & \text{for } (\theta, \phi) \text{ is over ocean} \end{cases}$$

and (θ_j, ϕ_k) and $(\theta_\alpha, \phi_\beta)$ are grid points with sampling interval $(\Delta\theta, \Delta\phi)$

$$\begin{aligned}\theta_j &= (j+0.5)\Delta\theta, \quad j = 0, \dots, \pi/\Delta\theta - 1; \\ \phi_k &= k\Delta\phi, \quad k = 0, \dots, 2\pi/\Delta\phi - 1;\end{aligned}\tag{2-36}$$

$$\begin{aligned}\theta_\alpha &= (\alpha+0.5)(\Delta\theta/\mu), \quad \alpha = 0, \dots, \pi/\Delta\theta - 1; \\ \phi_\beta &= \beta(\Delta\phi/\mu), \quad \beta = 0, \dots, 2\pi/\Delta\phi - 1;\end{aligned}\tag{2-37}$$

μ in Eq. 2-37 is an odd number integer which is applied to subdivide the sampling interval, the reason we choose μ to be odd is to make sure the original grid cell centers are still the centers of certain subdivided grid cells. In this study we choose $\mu = 3$.

Eq. 3-34 gives the discrete form of isotropic Gaussian filter without distinguishing land and ocean. For recovering land signal, we suppose (θ'_j, ϕ'_k) is on land, and rewrite the equation with the filter distinguishing land ocean in form of:

$$\bar{h}_L(\theta'_j, \phi'_k) = Y_L^{-1}(\theta'_j, \phi'_k) \sum_{(\theta_\alpha, \phi_\beta) \in L} h(\theta_\alpha, \phi_\beta) G(\psi_{jk}^{\alpha\beta}) \sin\theta_\alpha \tag{2-38}$$

$$Y_L(\theta'_j, \phi'_k) = \sum_{(\theta_\alpha, \phi_\beta) \in L} G(\psi_{jk}^{\alpha\beta}) \sin\theta_\alpha \tag{2-39}$$

With the assumption made above that the signal over ocean is small enough the ocean contribution to the summation in Eq. 3-34 is negligible, we have:

$$\sum_{(\theta_\alpha, \phi_\beta) \in S} h(\theta_\alpha, \phi_\beta) G(\psi_{jk}^{\alpha\beta}) \sin\theta_\alpha \approx \sum_{(\theta_\alpha, \phi_\beta) \in L} h(\theta_\alpha, \phi_\beta) G(\psi_{jk}^{\alpha\beta}) \sin\theta_\alpha \tag{2-40}$$

Hence, we obtain the desired smoothed mass changes over land with reduced signal leakage from Eq. 2-34, 2-38, 2-40:

$$\bar{h}_L(\theta'_j, \phi'_k) = \bar{h}(\theta'_j, \phi'_k) \frac{Y(\theta'_j, \phi'_k)}{Y_L(\theta'_j, \phi'_k)} \tag{2-41}$$

Based on the formulation above, the leakage reduction method could be modified to study mass changes in regions of interests. We apply this leakage reduction approach to estimate ice mass changes in Greenland and Antarctic in Chapter 5 and 6 respectively.

2.3 Uncertainty of GRACE mass estimates

The goal of this study is to use GRACE monthly gravity field to estimate global ice mass changes. The errors in those estimates fall into two categories [Wahr et al., 2006]: (1) those due to measurement and processing errors in the monthly GRACE solutions; (2) those due to changes in the true monthly mass averages caused by other geophysical processes other than ice mass changes. Contributions to category (2) errors are mainly from unmodeled, or poorly modeled, mass variations for other geophysical signals. Theoretically, category (2) errors can be reduced by improved geophysical models. Category (1) errors, on the other hand, cannot be reduced without re-generating the gravity field solutions [Wahr et al., 2006]. Here, we estimate the effects of category (1) errors in GRACE monthly fields, as described in Wahr et al. [2006].

Estimates of “calibrated standard deviations” (square roots of the diagonal elements of the covariance matrix) in the monthly GRACE Stokes coefficients are meant to represent the category (1) errors. However, the Release 05 GRACE data from CSR do not include estimates of “calibrated errors” in the Stokes coefficients anymore. To assess the calibrated errors, we fit and remove a linear trend and an annual cycle from the 115 monthly values of each Stokes coefficient (January 2003 – December 2012). The residuals are assumed to be due to category (1) errors. In fact, this would overestimate those errors, since some of the non-annual variability is surely real. However, there are still no better solutions available for assessing category (1) errors, because it is difficult to use ground truth to validate GRACE mass estimates. Wahr et al. [2006] compared root mean square (RMS) values of the residual coefficients with the calibrated errors provided by the GRACE Project. The general agreement is good. Therefore, it is reasonable to use the GRACE residual coefficients to assess the accuracy of GRACE mass estimates.

Based on Eq. 2-16, we can relate time-variable GRACE Stokes coefficients to mass changes. Here, we rewrite the equation in a concise way. For monthly field i ($i = 1, \dots, N$, where $N=115$), GRACE mass estimates obtained from those gravity fields are expressed as:

$$h_i = \sum_{l,m} [F_{lm} C_{lm}^i + G_{lm} S_{lm}^i] \quad 2-42$$

Where F_{lm} and G_{lm} are time-independent coefficients:

$$\begin{Bmatrix} F_{lm} \\ G_{lm} \end{Bmatrix} = \frac{a\rho_{ave}(2l+1)}{3\rho_w(1+k_l)} \tilde{P}_{lm}(\cos\theta) \begin{Bmatrix} \cos(m\phi) \\ \sin(m\phi) \end{Bmatrix} \quad 2-43$$

Let δh_i , δC_{lm}^i , δS_{lm}^i represent errors in the mass estimates and in the Stokes coefficients. Then we have:

$$\delta h_i = \sum_{l,m} [F_{lm} \delta C_{lm}^i + G_{lm} \delta S_{lm}^i] \quad 2-44$$

The RMS of the mass errors is:

$$\begin{aligned}\Delta &= \sqrt{\sum_{i=1}^N \frac{\delta h_i^2}{N}} \\ &= \sqrt{\sum_{l,m,p,q} \left[F_{lm} F_{pq} \left(\sum_{i=1}^N \frac{\delta C_{lm}^i \delta C_{pq}^i}{N} \right) + 2F_{lm} G_{pq} \left(\sum_{i=1}^N \frac{\delta C_{lm}^i \delta S_{pq}^i}{N} \right) + G_{lm} G_{pq} \left(\sum_{i=1}^N \frac{\delta S_{lm}^i \delta S_{pq}^i}{N} \right) \right]}\end{aligned}\quad 2-45$$

According to Wahr et al. [2006], the inclusion of off-diagonal elements (i.e., where $(p, q) \neq (l, m)$) has little impact on the RMS. If we ignore these elements, the equation of RMS above can be reduced to:

$$\Delta = \sqrt{\sum_{l,m} \left[F_{lm}^2 \left(\sum_{i=1}^N \frac{(\delta C_{lm}^i)^2}{N} \right) + G_{lm}^2 \left(\sum_{i=1}^N \frac{(\delta S_{lm}^i)^2}{N} \right) \right]}\quad 2-46$$

We estimate the mass errors by injecting the Stokes coefficient residuals into the equation above. As mentioned above, the Release 05 GRACE data from CSR do not include estimates of “calibrated errors” in the Stokes coefficients anymore, and Wahr et al. [2006] proved RMS values of the residual coefficients agree well with the calibrated standard deviations provided by the GRACE Project. We choose to use RMS of mass estimates to approximate the standard deviations. Figure 2.8 shows our estimated uncertainties (one RMS) in the GRACE mass estimates, expressed in mm of equivalent water height, when F_{lm} and G_{lm} include Gaussian averaging function W_l with a 300 km Gaussian smoothing radius. The RMS is nearly longitude-independent, by virtue of the averaging over longitudes (Eq. 2-46). Also, it is smaller near the poles than at low latitude, due presumably to denser ground track coverage near the poles [Wahr et al., 1998].

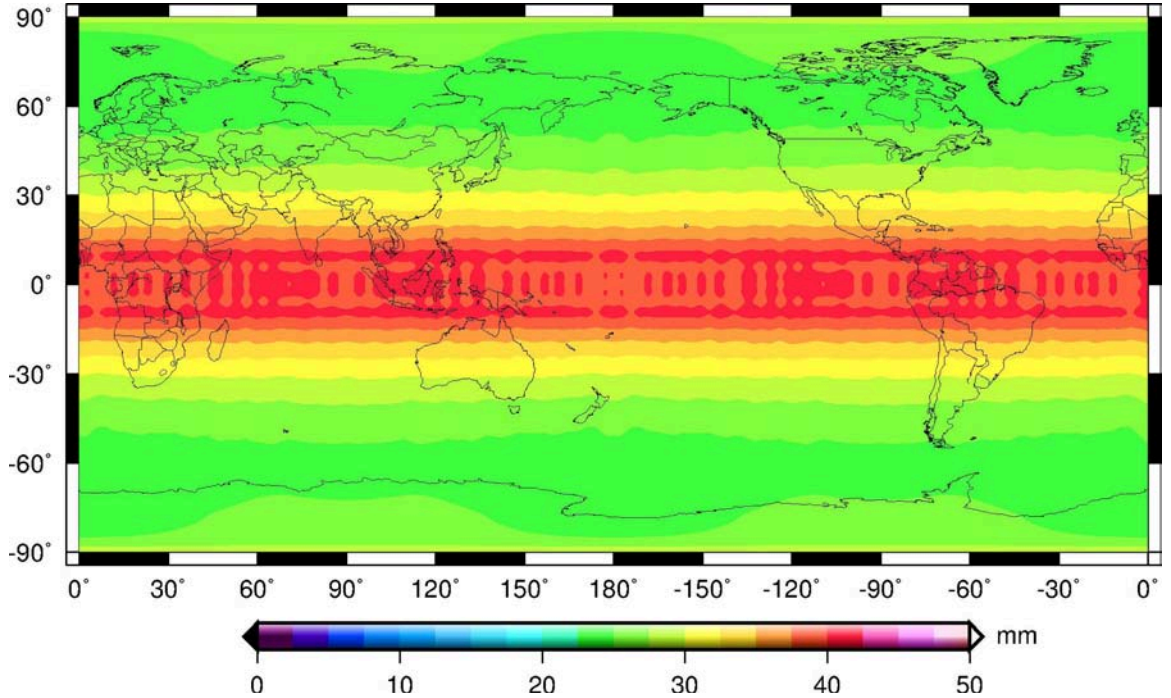


Figure 2.8 Our estimated uncertainties in the GRACE mass estimates, in mm of equivalent water height, for 300 km Gaussian averages and averaged over all 115 months.

For major glacier systems and ice sheets, one should sum up all the ice-covered grid points to calculate their total mass changes:

$$\mathbf{M}_i = \sum_{j=1}^P a^j h_i^j = \mathbf{A} \mathbf{h}_i \quad 2-47$$

$1 \times P$ $P \times 1$

where a^j is the area of the j^{th} grid cell of ice-covered region, and h^j is EWH anomaly in unit of meter that represents the corresponding grid cell. To get the uncertainty of \mathbf{M}_i , we should know the variance-covariance matrix on \mathbf{h}_i , based on the rule of error propagation. Our problem now is to derive the full variance-covariance matrix \mathbf{C}_{hh} of the mass changes in the ice-covered region, starting from the knowledge of the variance-covariance matrix \mathbf{C}_{TT} . We use the RMS of GRACE residual coefficients to approximate the square roots of variance elements in \mathbf{C}_{TT} (here we also use just the diagonal elements, and set all the off-diagonal ones to be zero). We write Eq. 2-42 in matrix form as:

$$\mathbf{h}_i = \mathbf{B}\mathbf{T} \quad 2-48$$

where \mathbf{B} contains the information of F_{lm} and G_{lm} , and \mathbf{T} contains GRACE Stokes coefficients. Based on the rule of covariance propagation, we have:

$$\mathbf{C}_{hh} = \mathbf{B}\mathbf{C}_{TT}\mathbf{B}^T \quad 2-49$$

The GRACE Stokes coefficients are up to the maximum degree of 60, which means 3717 coefficients are to be considered. Hence the dimension of matrix \mathbf{C}_{TT} is 3717×3717. For ice-covered region with P number of grid points, the dimension of matrix \mathbf{B} is $P \times 3717$. The definition of \mathbf{B} is not unique, but depends on the order chosen of the Stokes coefficients and of the grid points [Albertella et al., 2008]. Here, we show our definition. First, we re-write F_{lm} and G_{lm} as:

$$\begin{Bmatrix} F_{l,m}^j \\ G_{l,m}^j \end{Bmatrix} = \frac{a\rho_{ave}(2l+1)}{3\rho_w(1+k_l)} W_l \tilde{P}_{lm}(\cos\theta_j) \begin{Bmatrix} \cos(m\phi_j) \\ \sin(m\phi_j) \end{Bmatrix} \quad 2-50$$

Then, we define \mathbf{B} as:

$$\mathbf{B} = \begin{bmatrix} F_{2,0}^1 & F_{3,0}^1 & \cdots & F_{2,1}^1 & F_{3,1}^1 & \cdots & G_{2,1}^1 & G_{3,1}^1 & \cdots & G_{60,60}^1 \\ F_{2,0}^2 & F_{3,0}^2 & \cdots & F_{2,1}^2 & F_{3,1}^2 & \cdots & G_{2,1}^2 & G_{3,1}^2 & \cdots & G_{60,60}^2 \\ \vdots & \vdots & \ddots & \vdots & \vdots & \ddots & \vdots & \vdots & \ddots & \vdots \\ F_{2,0}^P & F_{2,0}^P & \cdots & F_{2,1}^P & F_{3,1}^P & \cdots & G_{2,1}^P & G_{3,1}^P & \cdots & G_{60,60}^P \end{bmatrix} \quad 2-51$$

Once we get \mathbf{C}_{hh} , we can calculate the variance of M_i as $\sigma_{M_i}^2 = \mathbf{A}\mathbf{C}_{hh}\mathbf{A}^T$.

To estimate the mass change rate, we fit a linear trend and an annual cycle from the 115 monthly values of each glacier/ice-sheet system:

$$M_i = a + b(t_i - t_0) + c * \cos[2\pi(t_i - t_0)] + d * \sin[2\pi(t_i - t_0)] \quad 2-52$$

where a is a constant, b is the linear trend rate, t_0 is the arithmetic average of time period t , c and d represent the amplitude of annual changes. Or, the equation can be written as:

$$\mathbf{M} = \mathbf{E}\xi \quad 2-53$$

Where ξ is 4×1 vector of unknown parameters (a, b, c, d), and \mathbf{E} is 115×4 coefficient matrix:

$$\mathbf{E} = \begin{pmatrix} 1 & t_1 - t_0 & \cos[2\pi(t_1 - t_0)] & \sin[2\pi(t_1 - t_0)] \\ 1 & t_2 - t_0 & \cos[2\pi(t_2 - t_0)] & \sin[2\pi(t_2 - t_0)] \\ \vdots & \vdots & \vdots & \vdots \\ 1 & t_{115} - t_0 & \cos[2\pi(t_{115} - t_0)] & \sin[2\pi(t_{115} - t_0)] \end{pmatrix} \quad 2-54$$

Standard least-squares solution is given as:

$$\hat{\xi} = (\mathbf{E}^T \mathbf{E})^{-1} \mathbf{E}^T \mathbf{M} \quad 2-55$$

And we can estimate the variance components based on error propagation:

$$\mathbf{C}_{\hat{\xi}} = (\mathbf{E}^T \mathbf{E})^{-1} \sigma_{\mathbf{M}}^2 \quad 2-56$$

Chapter 3 Uncovered Spurious Jumps in the GRACE De-aliasing Data

In GRACE data processing, the effect of high-frequency mass variations in the atmosphere and ocean is taken into account during temporal gravity field modeling in order to minimize temporal and spatial signal aliasing. We find two spurious jumps in the atmosphere and ocean de-aliasing level-1b (AOD1B) data product, which occurred from January to February in both 2006 and 2010. These jumps attain about 7 cm of equivalent water thickness (EWT) change in some regions including the Qinghai-Tibetan Plateau and South America, and appear to be spurious biases caused by the resolution change in the European Centre for Medium-Range Weather Forecasts (ECMWF) model at the beginning of 2006 and 2010 respectively. These uncovered jumps are unlikely to be real atmospheric signals primarily because they are absent in the ECMWF Re-Analysis (ERA-Interim) model. Here, we show that these spurious jumps, uncovered in both the Release 04 (RL04) and the Release 05 (RL05) AOD1B data, would produce jumps of the same magnitude with opposite signs, thus may contaminate the GRACE data products in specific regions of the world. As a consequence, estimates of regional mass changes including glacier mass balance could potentially have errors.

3.1 Introduction

The Gravity Recovery and Climate Experiment (GRACE) [Tapley et al., 2004] twin-satellite mission launched in March 2002 is measuring Earth's time-variable gravity field with unprecedented accuracy and temporal and spatial resolutions. The monthly GRACE measurements of Earth's gravity field provide accurate information on large-scale mass redistribution within the Earth system [Wahr et al., 1998]. A large variety of scientific problems in diverse disciplines have been studied using GRACE data, including ice mass balance of polar ice sheets and mountain glaciers, ocean bottom pressure and global sea level rise, hydrologic fluxes and earthquake induced seismic deformation [Velicogna et al., 2006; Chen et al., 2006; Jacob et al., 2012; Rodell et al., 2009; Chambers et al., 2004; Morison et al., 2012; Swenson et al., 2006; Han et al., 2006].

The data products from the GRACE mission include monthly average geopotential models in the form of spherical harmonic series except degree 0 and 1, which are known as the level 2 (L2) data product. To more accurately solve for the monthly average geopotential, it is essential to remove the effects of tides and the non-tidal time-varying mass variations in the atmosphere and ocean, especially the high-frequency variations, from GRACE observations. The correction is necessary because the high-frequency effects alias into the observations due to the space-time sampling characteristics of the GRACE twin-satellite orbits. Consequently, in the L2 data, effects of time-varying geophysical phenomena better determined from techniques other than GRACE, such as solid Earth and oceanic tides and pole-tide, are removed. Furthermore, effects of high-frequency atmospheric and oceanic processes are also removed based on models, which

are referred to as the atmosphere and ocean de-aliasing level-1b (AOD1B) data product [Flechtner et al., 2007, Zenner et al., 2010, Zenner et al., 2012].

However, the de-aliasing data could be a potential error source of GRACE geopotential solutions if they are not accurately calculated. In this study, we present an analysis of the AOD1B de-aliasing data products, for both the Release 04 (RL04) and the RL05 data, spanning as long as 9 years, between January 2003 and December 2011. We find two large jumps in the AOD1B atmospheric data, which appear to be spurious other than real atmospheric signals. Because of subtraction of AOD1B signal during processing, these spurious jumps would incur jumps of the same magnitude with opposite sign in the GRACE level 2 (L2) data inferred mass changes such as glacier melting, consequently contaminating regional mass transport estimates from GRACE data. These jumps may attain ~ 7 cm of equivalent water thickness (EWT) change in certain regions, e.g., in Qinghai-Tibetan Plateau and the western part of South America with voluminous ice coverage. We use South America as an example to quantitatively illustrate how the glacier mass balance estimates using GRACE L2 data could be contaminated by the jumps.

These jumps are likely caused by the horizontal and/or vertical resolution change in the European Center for Medium-range Weather Forecasts (ECMWF) operational atmospheric model adopted for deriving the AOD1B data. We find that the jumps occurred on February 1, 2006 and January 26, 2010, respectively (http://www.ecmwf.int/products/data/operational_system/evolution/).

3.2 Systematic Biases in the AOD1B Data

We examined both the Release 4 (RL04) and 5 (RL05) of the Level-2 data (GAA and GAC products) applied by all three official GRACE data product centers: the University of Texas at Austin Center for Space Research (CSR), the German Research Center for Geosciences (GFZ), and the Jet Propulsion Laboratory (JPL). Since all these 3 centers are using the same AOD1B product delivered by GFZ, the differences among them are insignificant for our purpose. The difference between RL04 and RL05 AOD1B products is that an updated ocean model is adopted for RL05 products. Considering that RL04 data are available for longer time span than RL05 data at the moment, and the same atmospheric data are used in both RL04 and RL05 products. we choose to present our results based on CSR AOD1B L2 GAC and GAA RL04 data for 9 years spanning 2003/01-2011/12, and focus mainly on the continental area.

The L2 GAC data are the monthly means of the geopotential due to variations in the atmosphere and oceans computed from 6-hourly AOD1B atmospheric and oceanic models, which have the same time span as the L2 monthly geopotential solutions, while the GAA data represent the geopotential variations due to atmosphere only [Flechtner 2007]. Each monthly GAC/GAA solution consists of a set of spherical harmonic (Stokes) coefficients from degree 0 up to a maximum degree 100, but only the coefficients from degree 2 onwards are used.

We first present a global view of the jumps, although the jumps could be more pronounced regionally such as at or around the Qinghai-Tibetan Plateau, which will be presented below. We use the changes of the averages of two consecutive years of the GAC solutions to more definitively detect the jumps, since signal of seasonal changes is

usually diminished in the yearly average. As both jumps occurred from January to February, we compute the yearly averages using monthly solutions from February to January in next year, so that no jumps due to real signals, i.e., seasonal variations, are included in the yearly averages. We roughly call the average from February 2003 to January 2004 the yearly average of 2003 and so forth. The jumps are presented in Figure 3.1 using EWT computed according to Wahr et al., [1998]. We present the changes from 2005 to 2006 (top panel) and from 2009 to 2010 (bottom panel) when the jump happened. As compared to the “normal interannual changes” (i.e., changes from 2003 to 2004, from 2004 to 2005 and so forth), the top and bottom panels include substantial spatially short wavelength changes. These short wavelength changes are likely caused by the jumps in the AOD1B data, which happened from January to February in both 2006 and 2010. We see that the short wavelength jumps are present over land. While zooming to very large scale maps, we see that the largest jumps seem to occur at locations with steep terrain elevation changes, e.g., the Tibetan Plateau and Tianshan in China, the Andes in South America and the Rocky Mountains in North America. Ripples over the oceans are more likely caused by spherical harmonics truncation used to represent GAC.

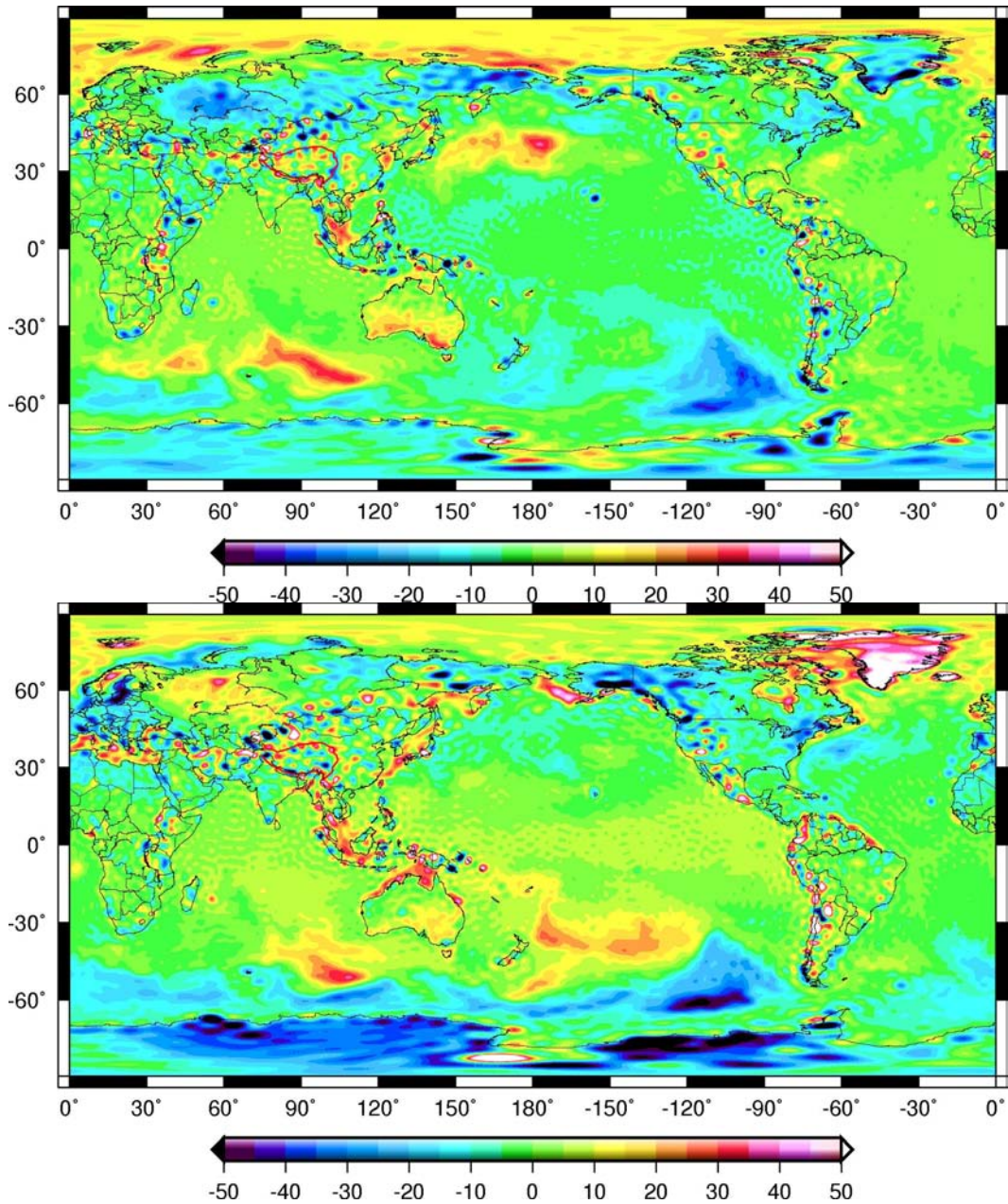


Figure 3.1 Changes of yearly averages of surface mass anomaly from monthly GAC data (in terms of equivalent water thickness in mm) showing a global view of the jumps in the de-aliasing product from January to February in both 2006 and 2010. TOP: the change from 2005 to 2006: BOTTOM: the change from 2009 to 2010.

Since we could not find any evidence to support the hypothesis that this kind of terrain-related jumps are real climate signals, we argue that they are most likely systematic biases in the atmospheric model adopted. Because surface pressure is the most important parameter in the computation of GAA/GAC products, if the jumps are real

signals, they should be reflected in changes of surface pressure values. To test our hypothesis, we have also used the reanalyzed monthly surface pressure data of the ECMWF Re-Analysis (ERA-interim) products (<http://ecmwf.int/research/era/Project/Plan>, 2000), which are generated with consistent resolutions, to show the corresponding yearly changes as shown in Figure 3.1 for comparison (Figure 3.3). The ERA-interim surface pressure data are converted into surface load in terms of height of water column by following Flechtner [2007]. All figures are similar to the top panel of Figure 3.1. The short wavelength features did not show up in the ERA-interim data, thus supports the hypothesis that the jumps in the GAC data are spurious. Actually, the jumps are very likely related to the changes of resolution in the atmospheric model, which will be further discussed later.

We have chosen the Tibetan Plateau, since the jumps are relatively larger over there, and that the quantification of the mountain glacier mass balance over there remains one of the major research interests (e.g., [Matsuo et al., 2010], [Jacob et al., 2012]). It can be readily inferred from Figure 3.2 how much glacier mass balance could be contaminated by the spurious jumps, as these spurious jumps would produce corresponding jumps in mass changes with the same magnitudes but with opposite signs.

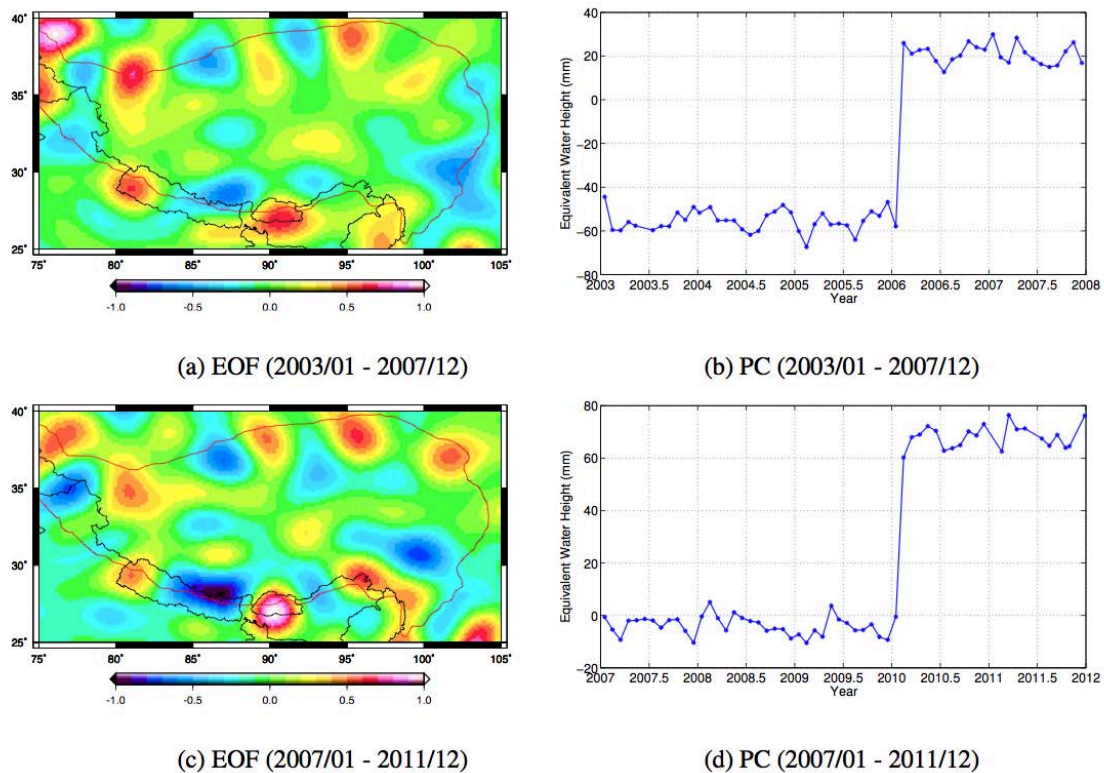


Figure 3.2 (a) Spatial pattern of the 3rd EOF over the Tibetan Plateau during 2003/01-2007/12; (b) its PC time series; (c) spatial pattern of the 3rd EOF over the Tibetan Plateau during 2007/01-2011/12; (d) its PC time series.

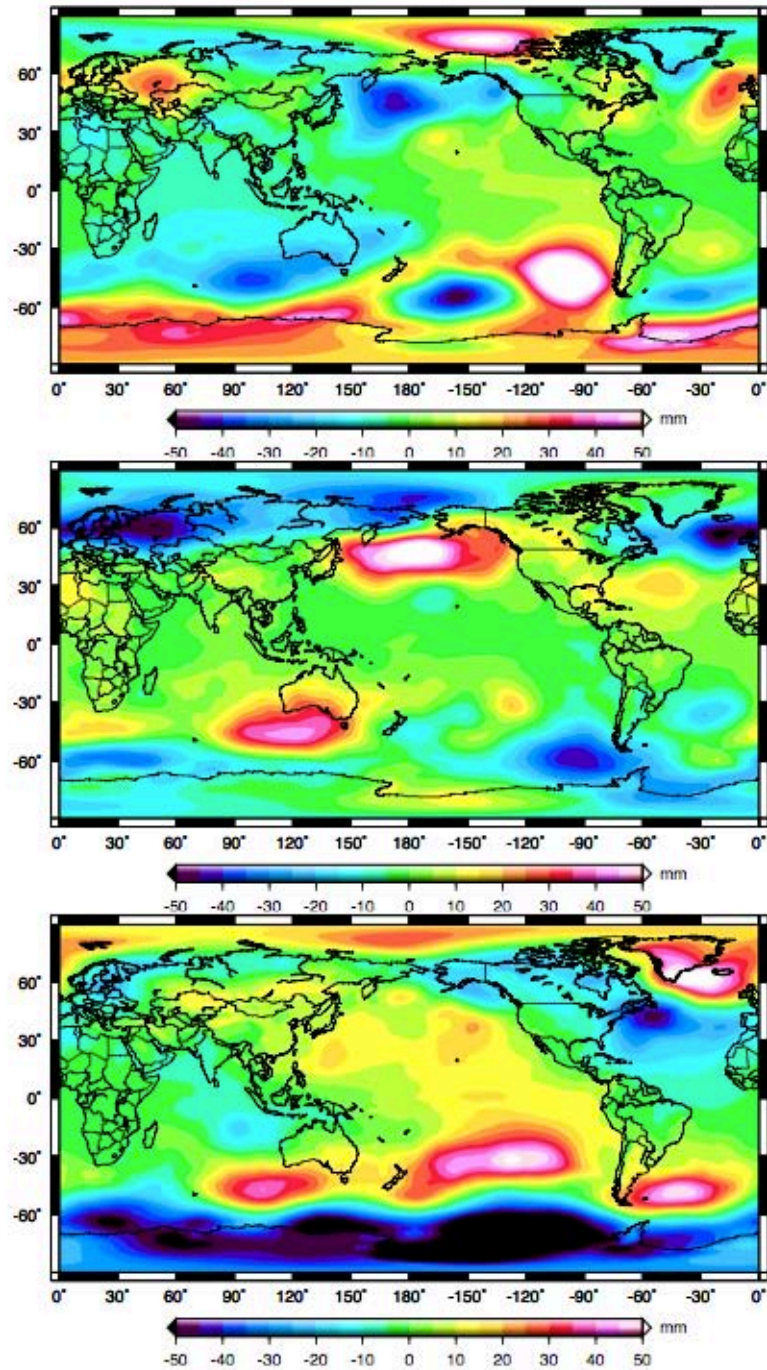


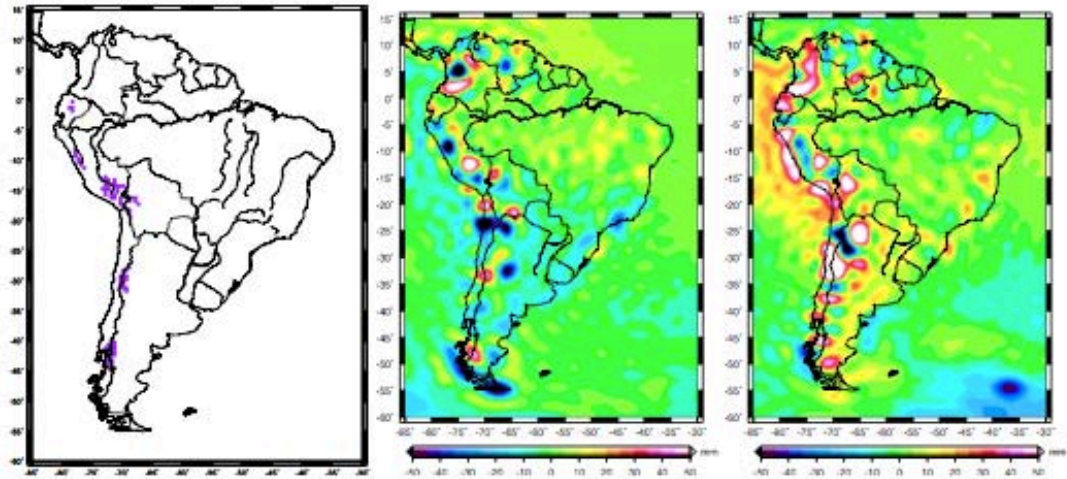
Figure 3.3 Year-to-year changes of annually averaged surface mass anomaly from the ERA-interim surface pressure product, from top to bottom are the changes from 2006 to 2007, from 2005 to 2006 and from 2009 to 2010, respectively.

3.3 Potential Impacts of the Systematic Biases

It can already be inferred from Figure 3.2 that the mass balance of Asian high mountain (AHM) glaciers, or study of hydrologic processes in or near the high-altitude regions using GRACE data may be contaminated by the jumps. Here we choose a simpler case of mountain glaciers in South America to illustrate the existence of jumps in mass balance estimates concurrent to the jumps in AOD1B data. Figure 3.4a shows the glacier distribution in South America except Patagonia, i.e., the Andes mountain glaciers, which is identical to the Region 16 of Jacob et al. [2012]. Figure 3.4b and 3.4c show the changes of yearly averages from 2005 to 2006 and from 2009 to 2010, which are approximately the jumps in AOD1B data as shown in the last section. It is clear that the glaciers are unfortunately located in the areas affected by the jumps in the AOD1B data.

Mountain glacier mass balance is estimated after removing mass variations which have not yet taken into account during GRACE level-2 modeling such as the glacial isostatic adjustment (GIA). Since estimations of mass balance using GRACE monthly geopotential data largely depends on the post-processing techniques applied, and our goal is to show the effects of the jumps in AOD1B data instead of more accurately estimating mass balance, therefore, we just apply a 350km Gaussian filtering [Wahr et al., 1998] to the GSM data. For the atmospheric pressure over land, computed from the GAC products and expressed in EWT, no filtering is applied. Both the mass balance computed using the GSM models and the atmospheric pressure computed using the GAC models are expressed over a 1×1 degree regular grid. The spatial average over the Andes mountain glacier region depicted in Figure 3.4a are computed by averaging the grid values within the region.

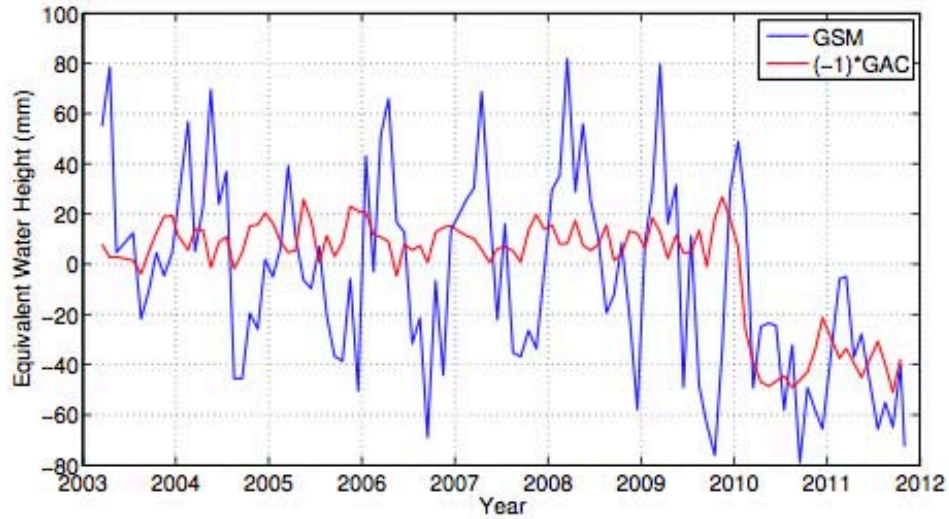
The results are shown in Figure 3.4d. We see that the jump from January to February 2006 does not have an apparent influence on the results. However, there is a sudden drop in the mass balance from January to February 2010. We also draw in this figure the atmospheric pressure variation, computed from the GAC products and expressed in EWT and multiplied by -1, which show practically the same drop from January to February. As the GSM data are computed after removing the AOD1B data, the concurrence of drops in both data sets is the evidence revealing that the drop in glacier mass balance estimate is actually a distortion due to the spurious jump in AOD1B data. From the time series of glacier mass balance in Figure 2 of Jacob et al. [2012], we can see the mass balance rate of -6 ± 12 Gt/yr for this region is the result of the sudden drop in early 2010. Hence, we claim that the spurious jump in early 2010 was misinterpreted as real glacier mass changes in Jacob et al. [2012].



(a) Glacier location

(b) 2005-2006 changes

(c) 2009-2010 changes



(d) Concurrent jumps

Figure 3.4 (a) Ice-covered regions in South America, from the Figure 1 in Jacob et al. [2012] (Courtesy Dr. John Wahr); (b) year-to-year change of GAC surface mass anomaly between 2006 and 2005 over South America; (c) year-to-year change of GAC surface mass anomaly between 2010 and 2009 over South America; (d) mass changes during 2003-2011 for ice-covered region 16 in Fig. 3.4a, blue line shows mass change from monthly GSM solutions, red line shows surface mass anomaly from monthly GAC data with sign changed (multiplied by -1).

3.4 Chapter Summary

We find two large jumps with magnitudes attaining about 7 cm of EWT change in the AOD1B atmospheric pressure variation data for both the RL04 and RL05 AOD1B data products from January to February in both 2006 and 2010, respectively.

A global view of the jumps are shown using the changes of the two yearly averages of atmospheric pressure just before and after the jumps in contrast to a case without the jumps, as seasonal changes are usually reduced in the yearly averages. The jumps have a short wavelength spatial feature, which is demonstrated in more detail for the Qinghai-Tibetan Plateau based on an EOF analysis. They are likely largest in regions with steep changes in terrain altitude over a short distance.

As we could not find any causes in atmospheric processes which could cause these jumps, we argue that they are spurious facts in the atmospheric data product. In support of our conjecture, no jumps are found in the corresponding times in the reanalyzed monthly ERA-interim atmospheric pressure data. Hence, the jumps appear only in the ECMWF operational model adopted for AOD1B. We find that the spurious jumps are likely related to resolution changes in the atmospheric model. On Feb 1, 2006, there is an increase of both vertical and horizontal resolutions, and on Jan 26, 2010, there is an increase of horizontal resolution. In both cases, when the jumps occurred, the horizontal resolution of the operational atmospheric model was increased, from T511 to T799 (from 40km to 25km) in 2006 and from T799 to T1279 (from 25km to 16km) in 2010. This implies that the orography (geopotential height) used in the atmospheric model was increased accordingly. Surface pressure, which is the most important parameter in the computation of the AOD1B products, changes with height. Therefore, with increased orography resolution, surface pressure values would be changed, especially in such areas with high terrain variability.

As the spurious jumps in the atmospheric de-aliasing product cause uncertainties in the monthly GRACE geopotential solutions, which in turn cause uncertainties in mass transfer estimates on Earth, for example for mountain glacier mass balance. Therefore, quantifying and correcting the impacts of the systematic biases in the GRACE de-aliasing products is critical. We propose a post-processing correction approach of the jumps for regional mass balance studies based on an EOF analysis. Take for example the jump from January to February 2006 in Tibetan Plateau shown in Figure 3.2. We first compute the averages of PCs during two years before and after the jump, respectively. We then subtract the average before the jump from the average after the jump. Finally we multiply the difference with the EOF to obtain the jump as function of location, which is referred to as true signal jump (TSJ). To remove the effect of the jump from GSM data, the TSJ should be added to all monthly GSM data after the jump.

Chapter 4 Glacier Mass Balance in High Mountain Asia

4.1 Introduction

The Tibetan Plateau (TBP) and surroundings in High Mountain Asia (HMA) contain the most extensive glaciers outside the Antarctic and Arctic, with a total area of about 100,000 km² glaciers coverage [Yao et al., 2012; Jacob et al., 2012; Bolch et al., 2012]. The more recent estimate of the glaciated area in this region is more than 20% different: 120,163 km² with ~5% uncertainty [Graham Cogley, pers. com.], and based on the recently available RGI 3.0. Melt water released from these glaciers supplements several major river systems in Asia, including the Indus, Ganges, Brahmaputra, Yangtze and Yellow river, which provide water for drinking, irrigation and other uses for over one billion people. Most of the glaciers in HMA have retreated and lost mass since the mid-19th century under the climate of global warming. However, annual amount of ice and snow melt along with the contribution of precipitation to discharge are all uncertain because of insufficient numbers of in situ measurements [Bolch et al., 2012].

Geodetic estimates derived from satellite gravimetric measurements, Gravity Recovery and Climate Experiment (GRACE), have provided glacial mass balance in HMA with unprecedented spatial coverage. However, substantial uncertainties exist mainly due to different data processing techniques and model corrections, hence yield controversies interpreting GRACE-derived glacial mass balance in HMA. Matsuo and Heki, [2010] reported the average ice loss rate of -47 ± 12 Gt/yr between April 2002 and April 2009. While Jacob et al. [2012] claimed that substantial groundwater signal over Indian plains was folded in the ice loss signal in Matsuo and Heki, [2012], thus caused an overestimated glacier mass loss. Total HMA ice change rate estimated by Jacob et al. [2012] is -4 ± 20 Gt/yr between January 2003 and December 2010. However, Yao et al. [2012] using *in situ* observation data pointed out the result of a positive glacial mass balance of ~ 7 Gt/yr in Tibet and Qilian Shan in Jacob et al. [2012] might be from uncertainty or misinterpretation of GRACE data. The necessity is then emphasized for a comprehensive study of the gravimetrically derived results with auxiliary information on existing mass balance data and other independent measurements, such as precipitation data, and satellite altimetry. Here we present our results by revisiting glacier status in HMA observed by GRACE.

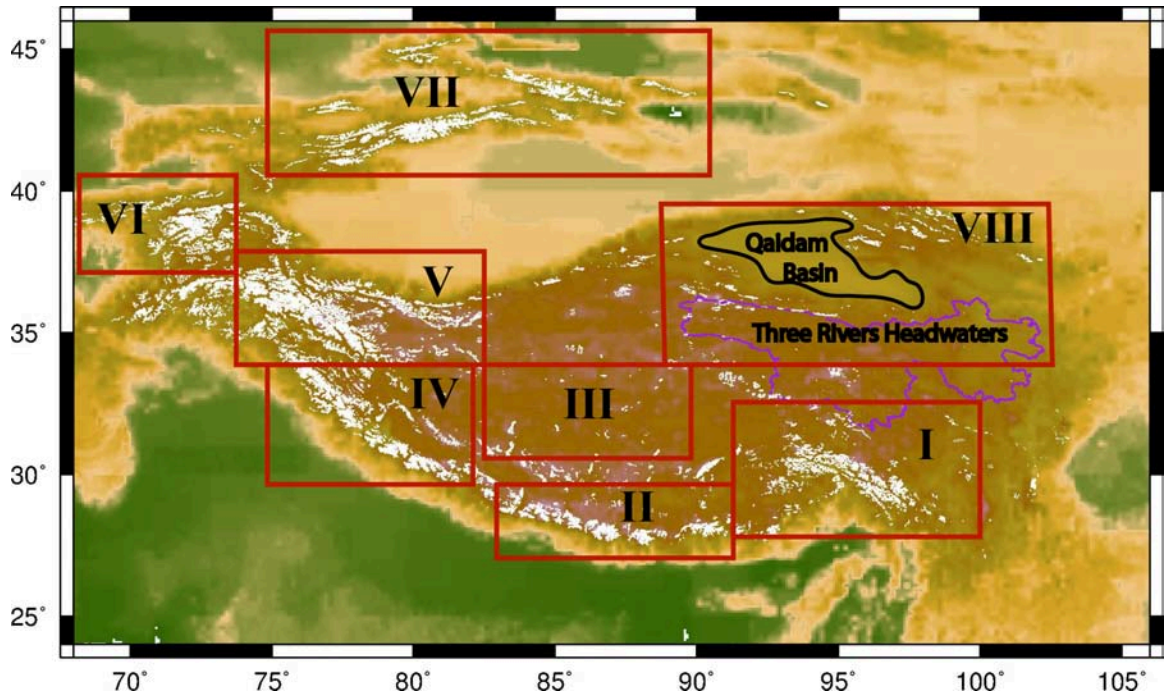


Figure 4.1 Glacier distributions in High Mountain Asia based on the most updated Randolph Glacier Inventory.

Zone Name	Covered Regions
Region I	East Himalaya, Hengduan Shan, Nyenchen Tanglha Mountains
Region II	East and Central Himalaya
Region III	South Qiangtang Plateau
Region IV	West Himalaya
Region V	Karakoram Mountain and West Kunlun Mountain
Region VI	East Pamir
Region VII	Tien Shan
Region VIII	Tibet Interior and Qilian Shan

Table 4.1 Information and covered regions of the 8 zones in Figure 4.1

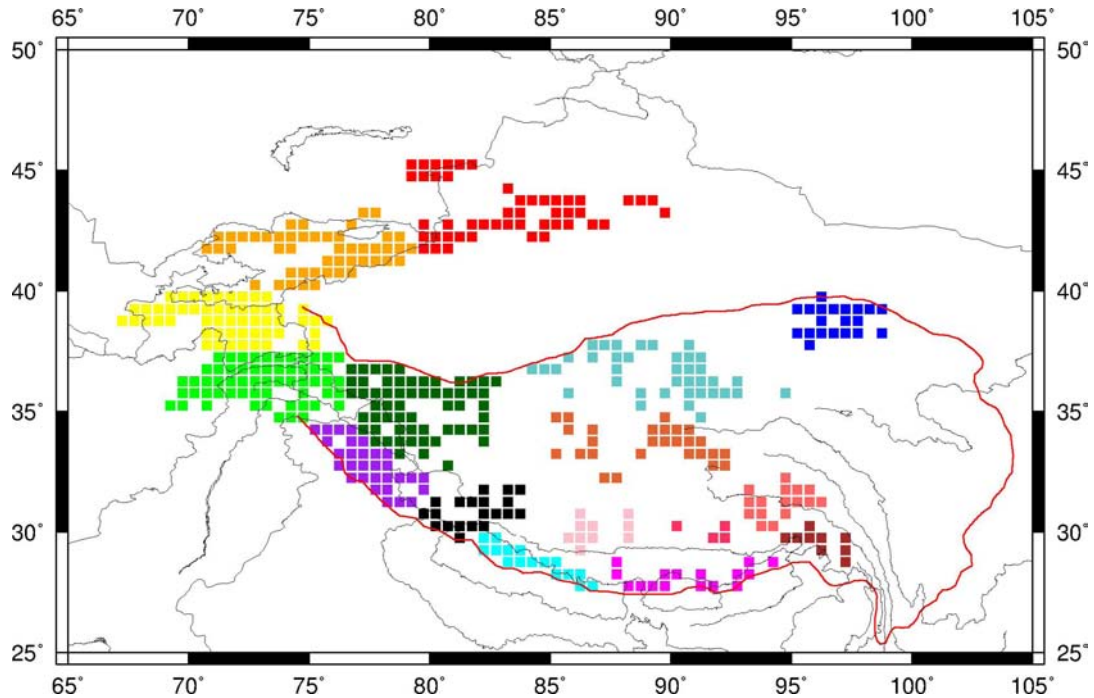


Figure 4.2 Ice-covered regions in HMA, from the Figure 1 in Jacob et al. [2012]. Squares with different colors represent different “mascons” for ice-covered regions. (Courtesy: Dr. John Wahr [Jacob et al., 2012])

4.2 Methods Summary

The Tibetan Plateau and its surroundings are influenced by Indian monsoon in the summer, and by westerlies in the winter. These two circulation systems, along with the huge topographic landform of these regions, exert climatic controls on the distributions of existing glaciers [Yao et al., 2012]. Hence, glaciers have different responses to climate changes according to their locations within HMA. To comprehensively analyze the glacier mass variations derived from GRACE, we divided the glaciers in HMA into eight regions, indicated clockwise as I-VIII in Figure 4.1. White areas in Figure 4.1 are glaciated regions according to the recently updated Randolph Glacier Inventory (RGI 3.0). Table 4.1 gives some information about their locations. To compare our results with those of Jacob et al. [2012], we also plot the “mascons” (small, arbitrarily defined regions of Earth [Jacob et al., 2012]) for the ice-covered regions in their study as Figure 4.2 shows. The classification is based on, but different from Yao et al. [2012], which allows for an ideal geographic representation of glaciers in HMA, and focuses on 2 regions in which recent debates on glacier melt rates rooted (region III and VIII). Regions I, II and IV are influenced by Indian monsoon and show extreme glacial shrinkage both in glacier length and glacier area based on in situ measurements [Yao et al., 2012]. Regions V and VI, which cover Karakoram, Western Kunlun and eastern Pamir, are mainly under the dominance of westerlies, and characterized by the least glacial retreating, area reduction and even positive mass balance for some glaciers. Tien Shan glaciers are located in Region VII according to our classification. Regions III and VIII have relatively sparse

glacier distributions, and are less influenced by the Indian monsoon and westerly; these two regions also contain most of Chinese's endorheic basins where precipitation that falls within does not flow out but may only leave the drainage system by evaporation and seepage. The total area of large lakes and open water bodies with a surface area larger than 0.1 km² reaches 40,000 km² based on the Global Lakes and Wetlands Database [Lehner and Döll, 2004] (Figure 4.3). The features of endorheic basins and vastly distributed wetlands in TBP play a key role interpreting the controversial result of a positive glacial mass balance.

The GRACE Release 5 (RL05) monthly solutions have lower noise level compared to those RL04 data used in Jacob et al. [2012] and Matsuo and Heki [2010]. We use 112 monthly GRACE global gravity fields from the University of Texas Center for Space Research, spanning January 2003 to December 2011. Each monthly solution consists of fully normalized Stokes coefficients to degree and order 60. Since the C₂₀ coefficients in GRACE monthly gravity field are poorly determined, we replace GRACE determined C₂₀ coefficients by independent estimates from satellite laser ranging [Cheng et al., 2004]. Although replacing C₂₀ results in insignificant difference for mass estimates over TBP because of its relatively low latitude and small area, we applied this correction anyway just for completeness. To suppress noise at high degrees and orders, we apply an enhanced destriping filter introduced in Chapter 2 and 150 km Gaussian smoothing to the monthly Stokes coefficients. After filtering and smoothing, monthly Stokes coefficients are then transformed to gridded surface mass variations.

What GRACE senses is the relative changes of total mass stored at all levels as a function of time $M(t)$. For HMA, GRACE-observed total mass changes mainly include glacier mass changes, hydrological water storage changes (i.e. soil moisture, groundwater, surface water, and snow cover), net increase of mass caused by GIA and post Little Ice Age (LIA) rebound. Therefore, geophysical models have to be applied to remove other geophysical effects and thus isolate the rate of glacier mass changes, dM_{glacier}/dt :

$$dM_{\text{glacier}}/dt = dM_{\text{GRACE}}/dt - dM_{\text{hydrology}}/dt - dM_{\text{GIA}}/dt - dM_{\text{LIA}}/dt - dM_{\text{other}}/dt \quad 4-1$$

where GIA is a slow uplift progress of the solid Earth as a delayed viscous response to past ice melting after the Last Glacial Maximum [Clark et al., 2009; Matsuo and Heki, 2010]. The removal of the ice weight led to slow uplift or rebound of the land, and the return flow of mantle material back under the deglaciated area is accompanied with net mass changes that can be detected by GRACE. LIA was defined by NASA as a cold period between AD 1550 and AD 1850 when heavy snowfalls were much more frequent than today. The effect of post-LIA rebound in HMA, which is not included in GIA correction, should also be taken into account here. dM_{other}/dt includes contributions from other geophysical signals, which are not modeled here, including tectonic uplift and those introduced in Section 4.3. According to Matsuo and Heki, [2010], such tectonic uplifts are slow enough to go on without severely disturbing isostatic equilibrium, and would

only make small gravity changes. It would require a long observing period and significant accuracy improvement of GRACE mission to detect the present day geoid height change of tectonic uplifts. Therefore, dM_{other}/dt and its uncertainty is not estimated in this study.

We remove GIA contribution using the Paulson07 GIA model [Paulson et al., 2007]. The effect of post Little Ice Age (LIA) rebound in HMA, which is not included in GIA correction, is corrected here simply by adopting the values used in Jacob et al. [2012]. Hydrology signals, as the source of largest uncertainties, are also corrected here. We correct hydrological water storage changes by averaging outputs of two hydrology models: the NOAH model simulations from the Global Land Data Assimilation System (GLDAS) [Rodell et al., 2004], and the WaterGAP Global Hydrology Model (WGHM) [Döll et al., 2003; Güntner et al., 2007]. Both model products provide monthly global land surface water storage parameters except Greenland and Antarctic. The spatial resolution is $0.25^\circ \times 0.25^\circ$ for GLDAS/NOAH, and $0.5^\circ \times 0.5^\circ$ for WGHM hydrology model (Data courtesy, Andreas Güntner, GFZ). For consistency, we transform the gridded model outputs into Stokes coefficients and applied the same filtering process as for GRACE data.

To determine the uncertainties of glacier mass change rates, we follow the rule of error propagation. In this study, uncertainties are given at the 95% (2 standard deviation, 2σ) confidence level. Since all the model corrections in Eq. 4-1 are independent with each other, we have:

$$u_{\text{glacier}}^2 = u_{\text{GRACE}}^2 + u_{\text{hydrology}}^2 + u_{\text{GIA}}^2 + u_{\text{LIA}}^2 \quad 4-2$$

We described how to calculate the uncertainty of GRACE mass estimates in Chapter 2.3. For the hydrology correction, we calculate the differences between those two models. We randomly pick several grid cells, and plot the differences as Figure 4.3 shows. One can see that the differences between those two models have some random aspect. Hence, we can choose to determine the uncertainty of hydrology correction from their differences. To do this, we follow the same procedure we applied to determine the uncertainty of GRACE mass estimates. What we need is just to replace the GRACE residual coefficients ($\delta C_{lm}^i, \delta S_{lm}^i$) with the differences of those two hydrology models ($C_{GLDAS}^i - C_{WGHM}^i, S_{GLDAS}^i - S_{WGHM}^i$).

The uncertainty from GIA correction is hard to estimate based on Paulson07 GIA model only. We introduced in another most commonly used model in GRACE community, Peltier's ICE-5G (VM2) model [Peltier, 2004]. We calculate the EWH differences between those two models for each grid cell located in HMA, then calculate their standard deviation, σ_h . $2\sigma_h$, multiplied by the area of glaciated regions, can be used to represent the uncertainty of GIA correction.

We discussed spurious jumps in GRACE atmospheric de-aliasing data product, which would potentially contaminate estimates of regional mass changes including mountain glacier mass balance. Here, we simply correct this effect by adding back the GAC jumps part. Numerical forward simulation approach [Chen et al., 2006] is adopted in this study to estimate regional mass change rates of each region or grouped regions by using geographical and other information. For Himalaya glaciers, because of their geographical distributions and GRACE resolution (larger than 330 km for CSR monthly gravity field), it is difficult to isolate glacier mass changes signal from surrounding groundwater depletion signals. To get more robust estimate, it is reasonable to isolate Himalaya glacier mass change rate by removing the contribution of surrounding groundwater depletion from GRACE observed total mass loss. We numerically estimate the total mass loss rate in those regions (-49 Gt/yr for the period Jan 2003 - Dec 2012), then adopt the mascon fitting approach from Jacob et al. [2012] to calculate the contribution of ground water depletion signal in Indian plains, which is -30 Gt/year for the same time span.

The effect of post-LIA rebound in HMA, is corrected here by simply adopting the values used in Jacob et al. [2012].

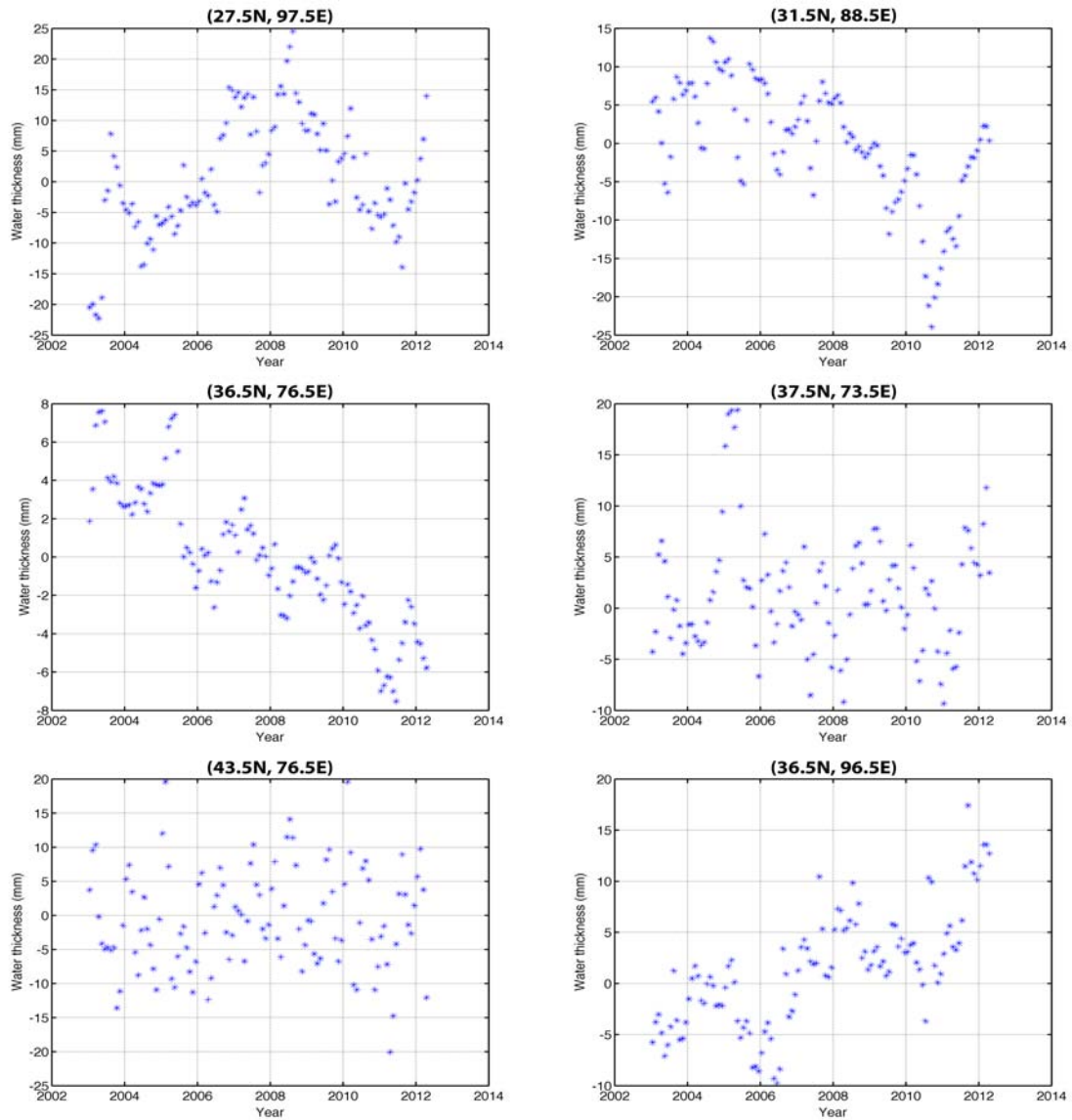


Figure 4.3 The differences between GLDAS/NOAH and WGHM hydrology models for randomly selected grid cells.

4.3 Main Uncertainty Sources

Corrections computed using corresponding geophysical models mentioned above are necessary. These models, on the other hand, are the major sources of large uncertainties. Besides model corrections of hydrology, GIA and LIA, there are still other error sources that we will show in this section. Some of the error sources cannot be modeled and corrected using current knowledge. However, taking them into account can avoid misinterpreting GRACE-observed mass changes.

4.3.1 Lakes and Wetland

The Tibetan Plateau (TBP) contains the largest area of high-altitude inland lakes in the world. There are more than 1000 lakes, with area larger than 1 km^2 , distributed within the TBP with total area of around $41,800 \text{ km}^2$. Here we show the major lakes and permanent open water bodies within TBP according to the new Global Lakes and Wetlands Database (GLWD) created by combining the best available sources of lakes and wetlands on a global scale. The GLWD comprise three coordinated levels on 1) large lakes and reservoirs, 2) smaller water bodies, and 3) wetlands. Blue shoreline polygons in Figure 4.4 show the geographical distributions of large lakes (area $\geq 50 \text{ km}^2$) and permanent open water bodies with a surface area $\geq 0.1 \text{ km}^2$. There are 138 large lakes distributed on the plateau, with a total area of $31,250 \text{ km}^2$, and the total area of permanent water bodies reaches $7,250 \text{ km}^2$. We can see that most of the lakes and water bodies are located in central TBP, including Qiangtang Plateau and Three Rivers' Headwaters, i.e. region III and VIII in our study. The total area of large lakes and water bodies only is 3 times larger than that of total glacierized areas in these regions, let alone vastly distributed wetlands.

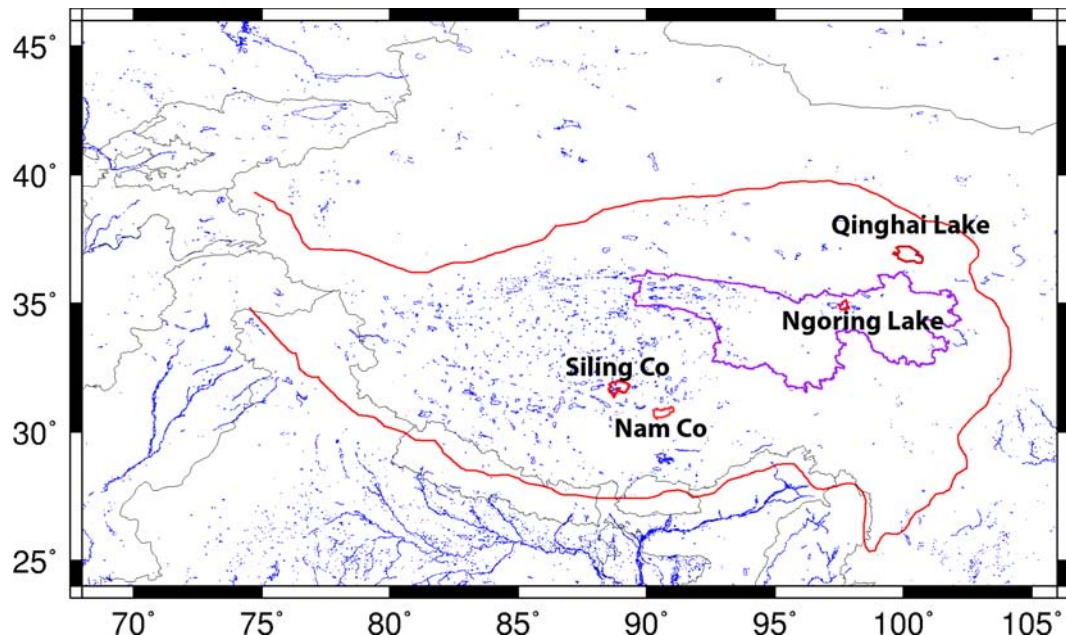


Figure 4.4 Lakes and open water distributions within TBP based on the new Global Lakes and Wetlands Database (GLWD).

4.3.2 Precipitation

Precipitation plays an important role to the total water storage variations for the TBP that contains large areas of lakes and glaciers, it is also the important forcing input data for hydrology model simulation, which affect the spatial-temporal variations of resulting water storage components. Neglecting the long term trend that precipitation from 1979 to 2010 decreased in the Himalaya and increased in the eastern Pamir regions [Yao et al.,

2012], we focus only on the variations of total precipitation during the GRACE time span. Here, we calculate the total precipitation of each year, then plot their yearly differences as Figure 4.5 shows. Large scale increased precipitation in 2005 over TBP interior, Eastern Kunlun and Karakoram confirms the mass gain anomaly observed by GRACE and lake level rising monitored by satellite altimetry. Increased precipitation in 2008 and 2011 over region III, and in 2007 and 2009 over region VIII are also evident. On the other hand, precipitation decrease over Himalaya and surrounded plains reveal the cause of mass loss in these regions.

Precipitation is also one of the most important forcing inputs to hydrology models. For the hydrology models we applied, we also plot the yearly differences of the precipitation data used in these two models, and show them in Figure 4.6 and 4.7 respectively. From the figures, we can see that although these 3 products in general show similar pattern over Indian plains, there are large differences in TBP interior, especially for 2004/2005, 2007/2008 yearly differences. The discrepancy among the precipitation data is directly reflected in mass change rate maps derived from those two hydrology models (Figure 4.10), e.g. mass gain rate of GLDAS/NOAH model, with its center located in (37°N, 98°E), is the response of abrupt high precipitation in 2005 from its precipitation input.

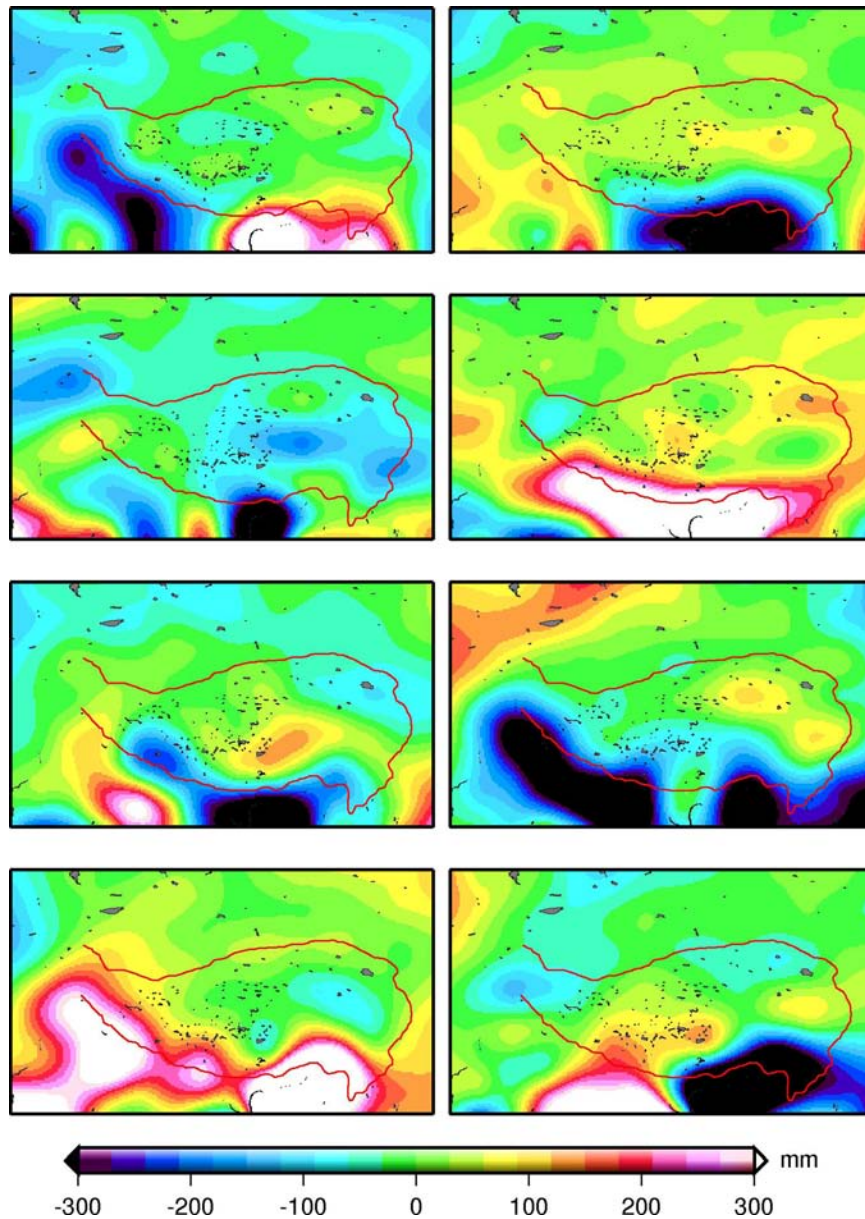


Figure 4.5 Yearly differences (from 2003 to 2011) of total annual precipitations observed by TRMM, same filtering+smoothing process is applied as GRACE data post-processing. Top panel represents the changes from 2003 to 2004 (left) and from 2004 to 2005 (right), the second panel shows the changes from 2005 to 2006 (left) and from 2006 to 2007 (right), the third panel similarly gives the 2007/2008 and 2008/2009 changes, the left and right map in the bottom panel represents the 2009/2010 and 2010/2011 differences respectively.

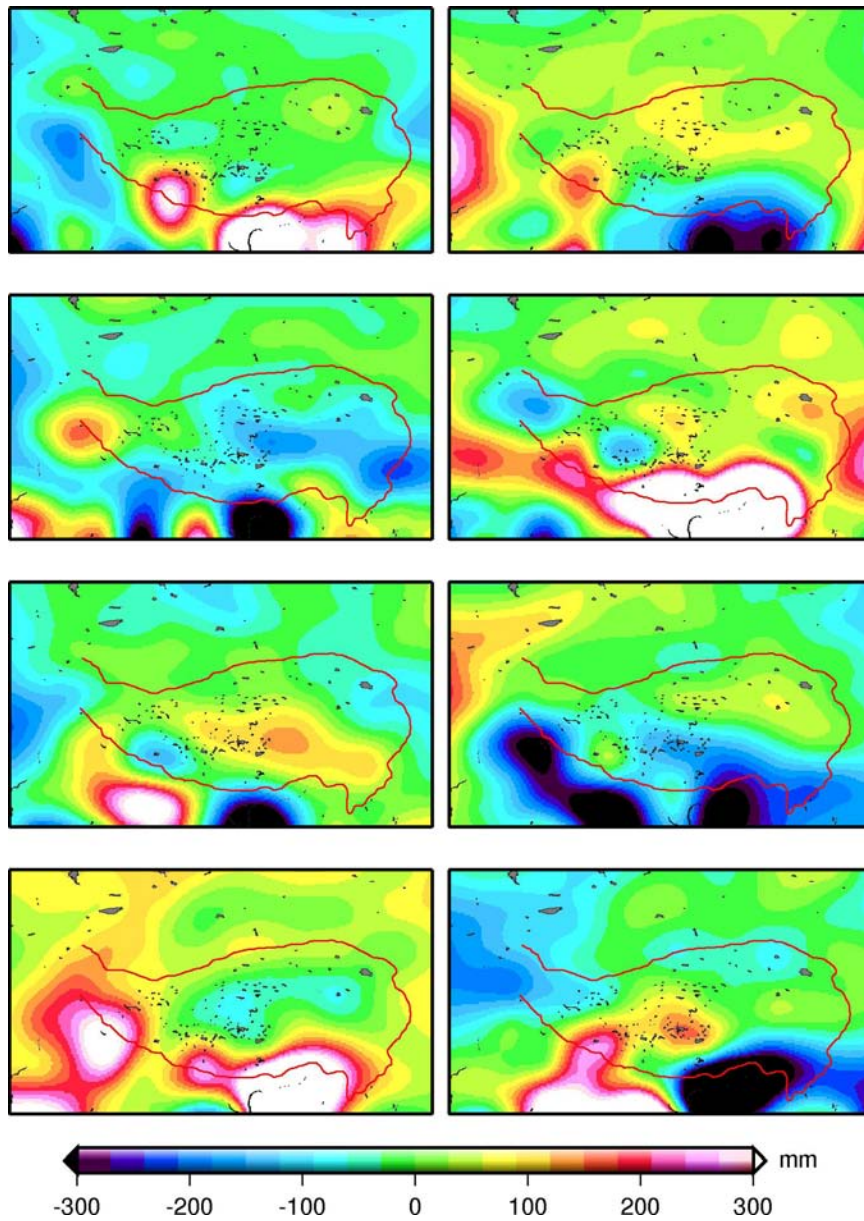


Figure 4.6 Same as Figure 4.4, but from GPCC data product, which is used as input source of WGHM hydrology model.

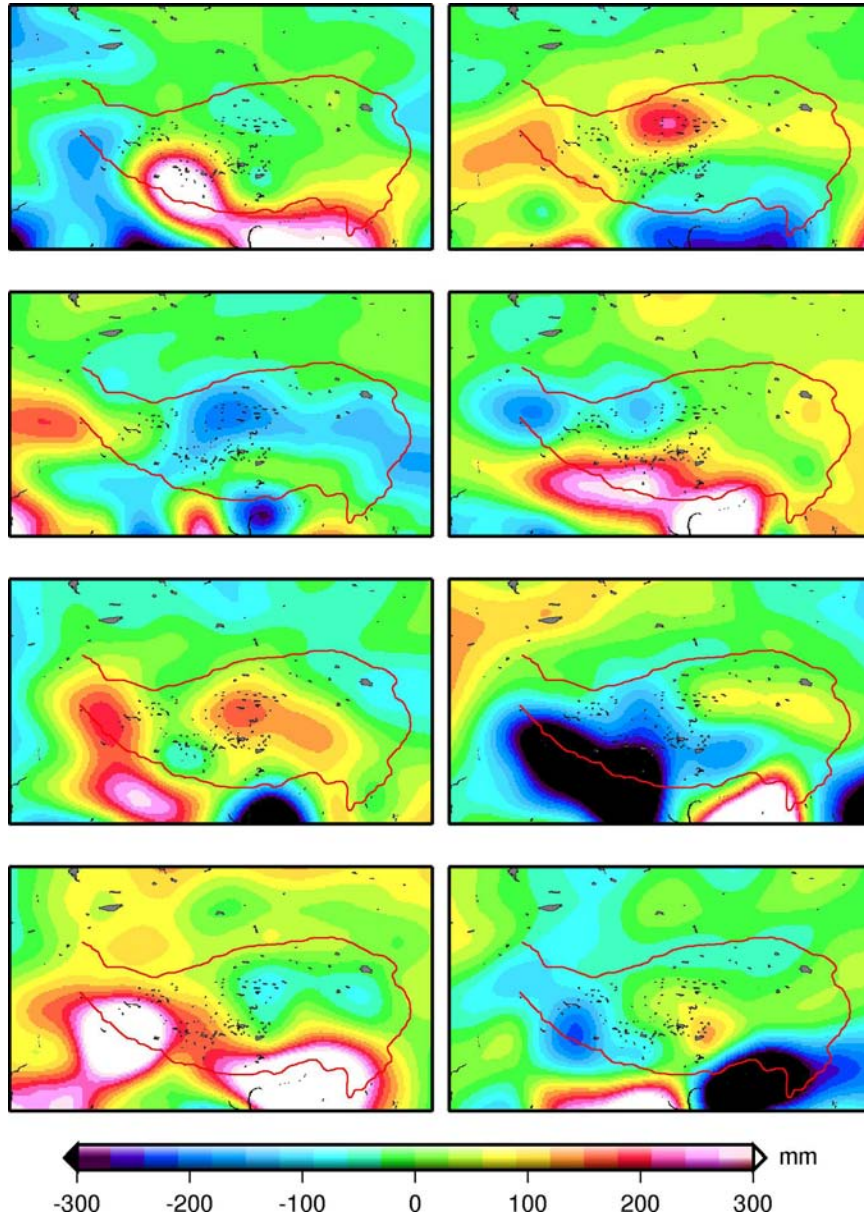


Figure 4.7 Same as Figure 4.4, but from precipitation data used as input source of GLDAS/NOAH hydrology model.

4.3.3 Hydrology Models

Hydrology correction is still the source of largest uncertainty for estimating glacier mass balance over HMA by using satellite gravimetry. Here, we also use hydrology models to remove hydrology contribution. Two land surface models used here are: the GLDAS/NOAH (version 2.7.1) and WaterGAP Global Hydrology Model (WGHM). Different from GLDAS/NOAH, which provides monthly soil-water storage and snow estimates only, the WGHM represents water storage including soil-water, groundwater, snow and surface water in rivers, lakes and wetlands. Figure 4.8 shows the trend maps determined from the two hydrology models during the same time span as of GRACE, the models are also filtered and smoothed as what we apply to the GRACE data for consistency. These two maps show no evident similarities with each other. For region III and III that contain vast area of lakes and wetlands, both models cannot fully explain GRACE observed mass gain signals. There is no surprise that GLDAS/NOAH does not show similar pattern as GRACE since no surface water compartment is simulated. WGHM shows similar mass gain trend in region VIII as GRACE trend map, but with much smaller magnitude. By further comparing the non-smoothed WGHM data, we see most of grids with large lakes covered show increasing mass trend, for lakes large enough to cover one or more than one WGHM grid, we compare the WGHM time series with satellite altimetry observed lake level changes as Figure 4.9 shows. Despite large magnitude differences, WGHM simulated total water storage (TWS) variations do not represent the contribution of 2005 annual precipitation as large as GRACE and satellite altimetry observed. For region III, WGHM simulated mass balance from 2006 to 2008 shows significant drop compared to increasing lakes level, which implies large uncertainties existing in this region, where extremely harsh climate conditions and remote locations restrict in situ meteorological stations distribution in the whole Qiangtang Plateau.

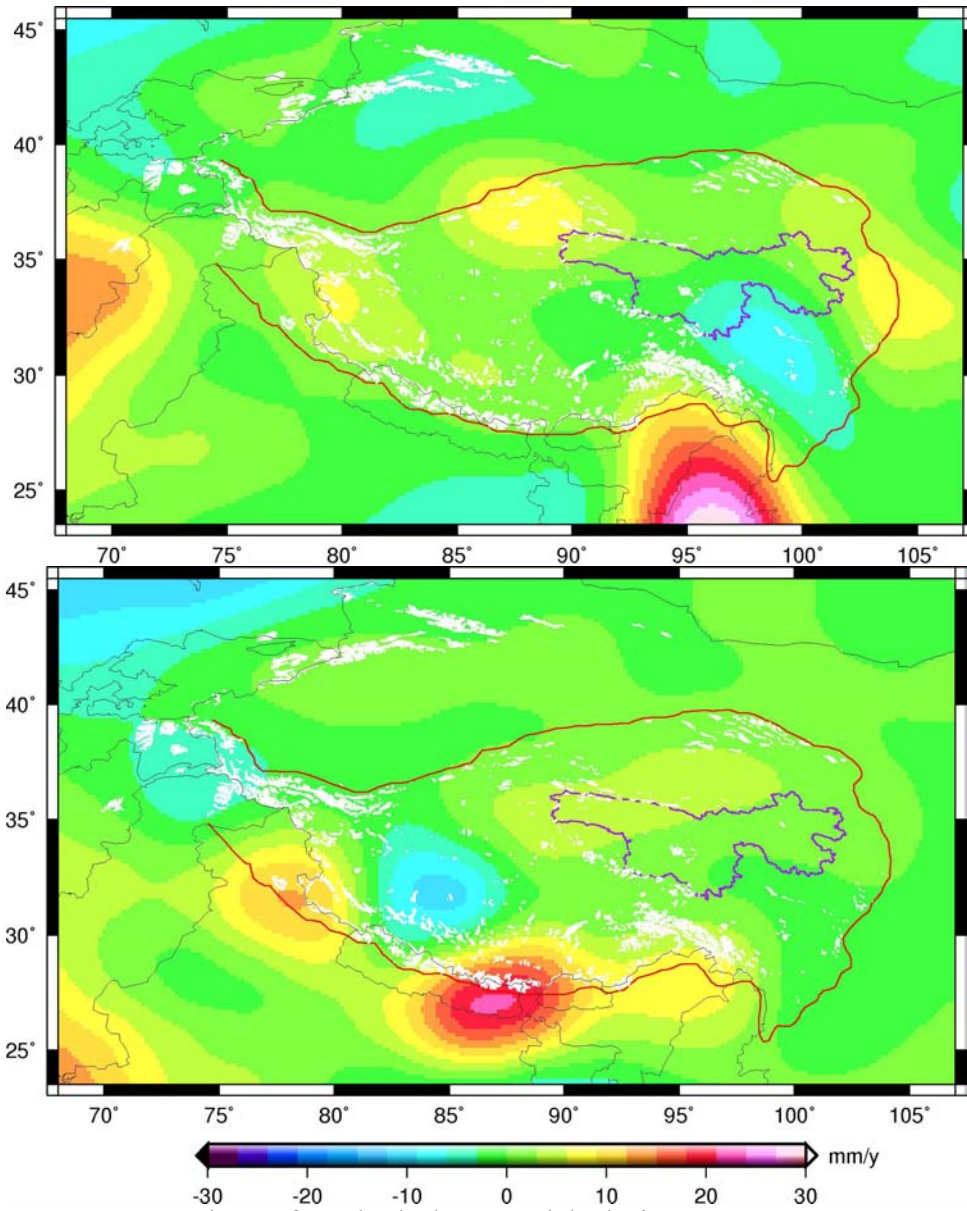


Figure 4.8 Mass trend map from hydrology models during Jan 2003 – Dec 2011, same filtering+smoothing process is applied as GRACE post-processing. TOP: GLDAS/NOAH model; BOTTOM: WaterGAP Global Hydrology Model.

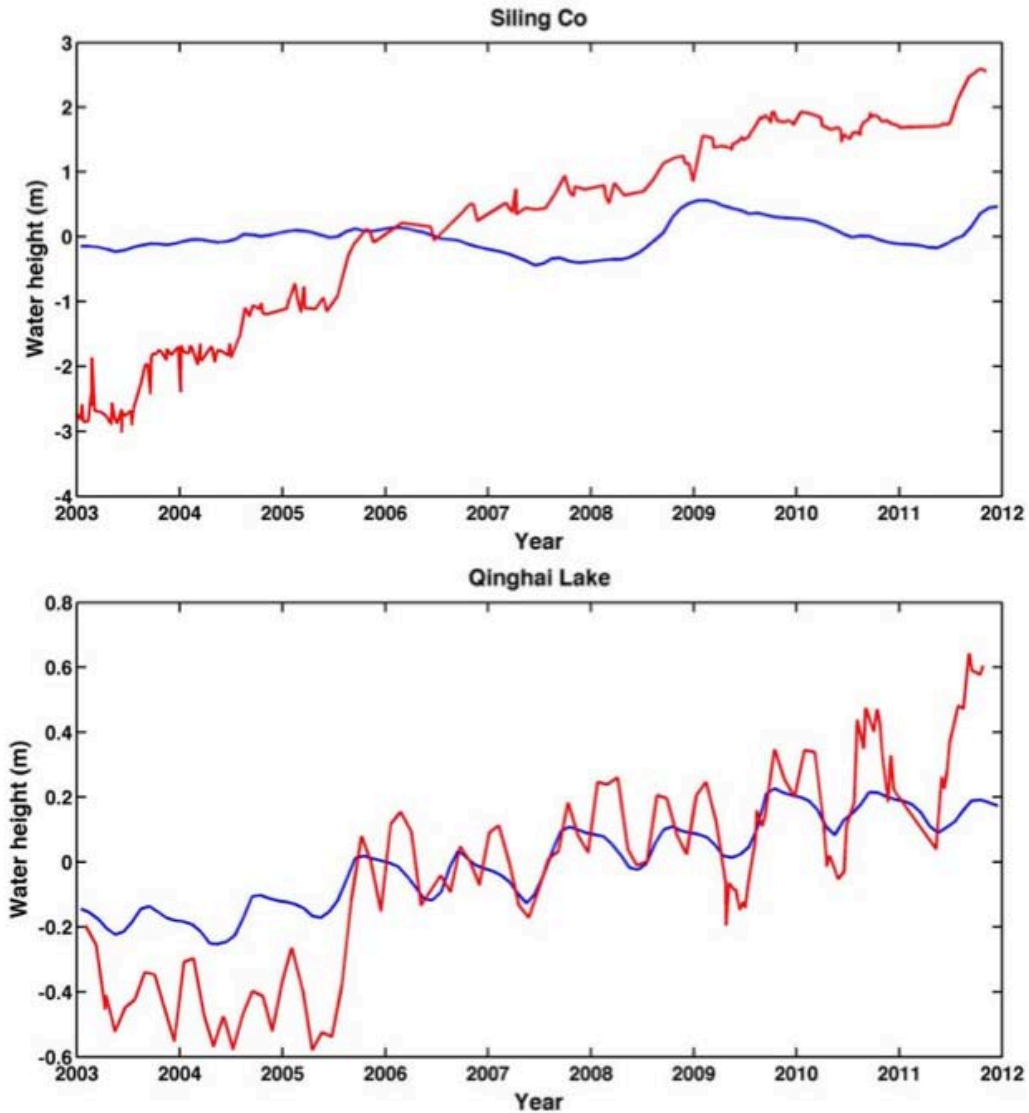


Figure 4.9 Comparisons between WGHM total water storage and satellite altimetry observed lake levels for lakes with areas larger than WGHM's grid resolution ($0.5^{\circ} \times 0.5^{\circ}$). TOP: Siling Co marked in Fig. 4.3; BOTTOM: Qinghai Lake. Red line shows the lake level changes observed by satellite altimetry, and the blue line shows the WGHM total water storage changes in the same regions.

4.3.4 Spurious Jumps in GRACE Atmospheric De-aliasing Data

In GRACE data processing, the effect of high frequency mass variations in the atmosphere and ocean is taken into account during temporal gravity field modeling in order to avoid temporal and spatial signal aliasing. In Chapter 3 we discussed two spurious jumps in the GRACE atmosphere and ocean de-aliasing level-1b (AOD1B) data

product, which would contaminate the GRACE data product in HMA. Here, we examine the effects of those two jumps, occurred in 2006 and 2010, to see how they would affect our estimates of glacier mass balance in HMA. We calculate the 2005/2006 and 2009/2010 differences of GAC and GSM respectively after applying the same filtering+smoothing process. The results are shown as Figure 4.10. The 2006 jump in GAC product does not reflect directly in the GSM derived geophysical mass changes; the 2010 jump, on the other hand, has noticeable effect on the GSM mass changes. We mark the locations where potentially are affected by 2010 GAC jump with black polygons in Figure 4.10b and Figure 4.10d respectively. Note different color scales applied, and since the GAC was removed during GRACE data processing, spurious jumps would produce jumps in GSM with opposite signs. Theoretically, the GAC jumps would cause jumps of the same magnitude in GSM product, and it is beyond the scope of this work to quantify them since this problem is related to how GRACE L2 data products are computed. Here, we just correct the jumps by adding back the GAC jumps, we then check their influences on mountain glaciers in Tien Shan. We roughly sum up mass loss signals corrected for GAC jumps in region VII, and compare the time series with the mascon solution result we duplicated according to Jacob et al. [2012]. As Figure 4.10e shows, our solution agrees well with the mascon solution before 2010 except that it is smoother since de-striping filter was applied. For the data after 2010, the difference with and without GAC jump correction is evident, a -9.4 Gt/yr mass loss rate (Jan 2003-Dec 2011) is fitted based on our estimate, compared to -6.5 Gt/yr using the mascon solution without GAC jump corrected.

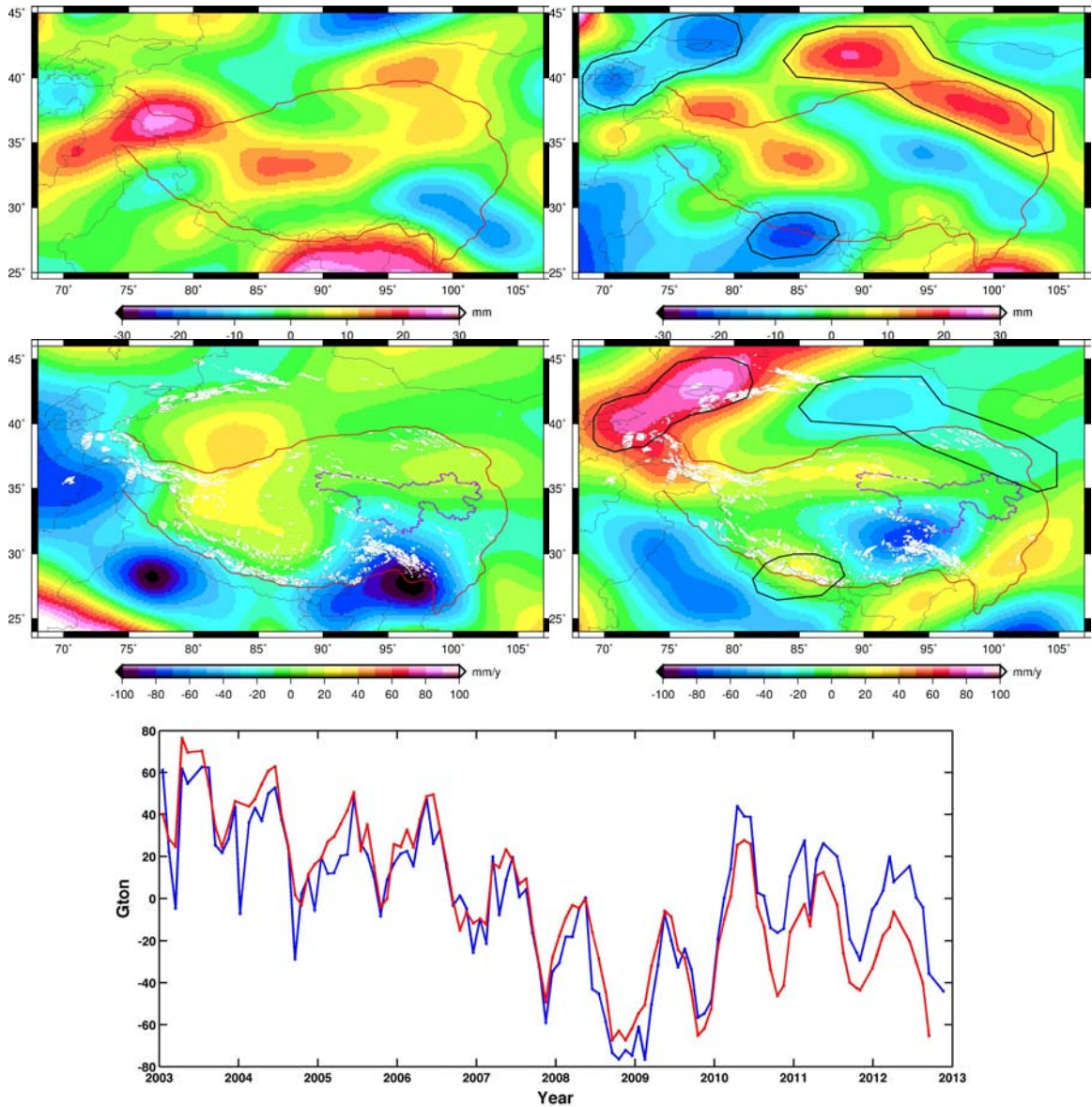


Figure 4.10 TOP: 2005/2006 (left) and 2009/2010 (right) differences of yearly average of GAC de-aliasing product expressed in mm of equivalent water height (EWH); MIDDLE: 2005/2006 (left) and 2009/2010 (right) differences of yearly averages of GRACE L2 GSM mass changes in mm of EWH; BOTTOM: case study for Tien Shan glaciers to show how the GAC jumps would affect glacier mass change estimation. Red line shows our estimate of mass change in region VII after GAC jump corrections, blue line shows mascon solution for the same region but without GAC jumps corrected.

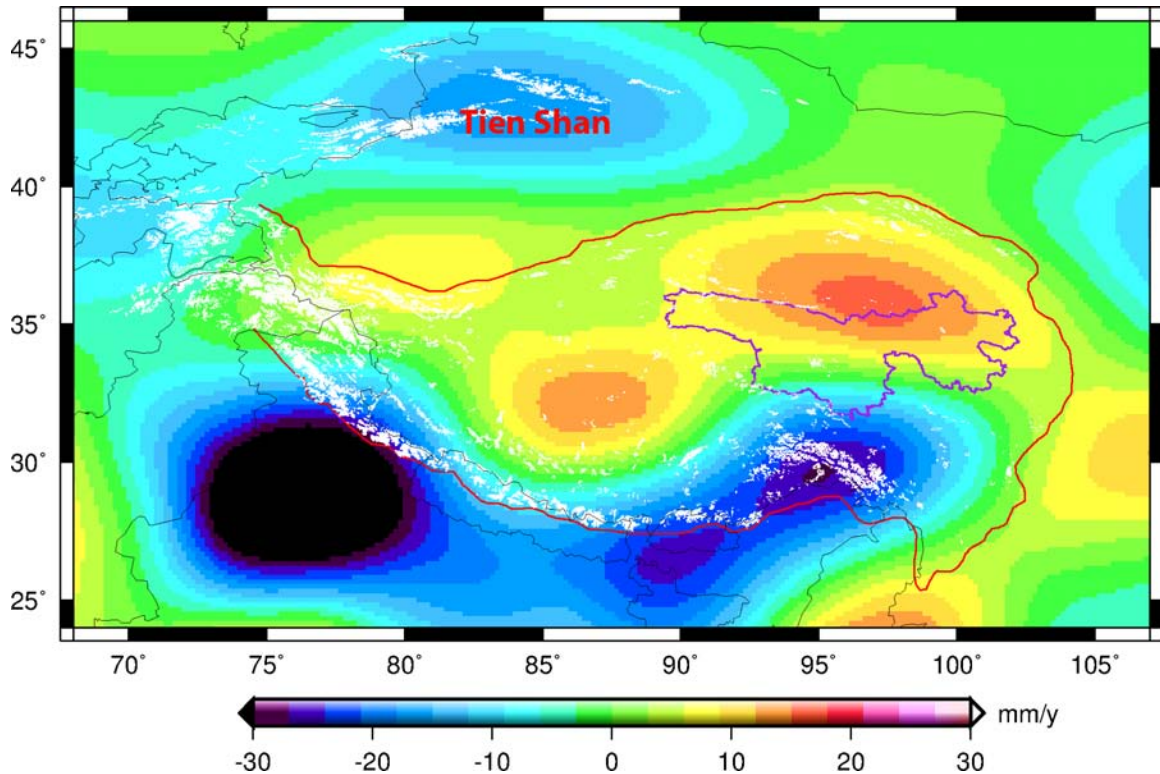


Figure 4.11 Mass trend map from GRACE during the period from January 2003 to December 2011.

4.4 Glacier Mass Balance in HMA

Figure 4.11 shows the GRACE derived mass rate over the HMA and surroundings corrected for GIA only. Largest decreasing signal occurs in North India, which is reported as groundwater depletion [e.g. Rodell et al., 2009]. For HMA glacier-covered regions, largest mass loss signal occurs in southeastern TBP, where Region I locates according to our classification. This agrees with the conclusion of Yao et al. [2012] based on in situ measurements that glacier shrinkage is most pronounced in the southeastern TBP. And the decreasing mass rate is getting smaller towards the west along the Himalayas with weakening Indian monsoon influences from east to west. Relatively small rate value over the east Pamir indicate the stability status of the glaciers in this region. The shrinkage of Tien Shan glaciers is also obvious based on our mass rate map. Compared to regions above with decreasing mass rates which are proved by in situ measurements, mass gain trends occur in Regions III, V, and VIII. Independent observations, both from in situ data and elevation changes observed from space, indicate slight mass gain of Karakoram glaciers [Yao et al., 2012; Gardelle et al., 2012], and in situ measurements from Yao et al. [2012] show the stable and even advancing characteristics in west Kunlun Mountains. Glacier mass change rate for each region are shown in Table 4.2. The second column shows GIA-corrected total mass change rates for each region, the third and fourth column gives the hydrology and post-LIA rebound correction respectively. We described in Section 2.3 and 4.2 how to determine the

uncertainties for hydrology corrections, and the uncertainties here are at the 95% (2 standard deviation, 2σ) confidence level. For the post-LIA rebound correction, we simply adopt the 2σ uncertainty estimates applied in Jacob et al. [2012]. After applying corrections in column 3 and 4 to GIA-corrected total mass change rates, we get the estimates of glacier mass changes showing in column 5. Interpreting the positive mass rate in Region III and VIII remains the biggest challenge then, since attributing these mass gain signals purely to the sparsely distributed glaciers in these 2 regions will draw controversies, especially when in situ data show an opposite result (Figure 4.13).

Regions	GRACE+GIA	Hydrology Correction	LIA	Rate
Region I+II+IV	-19±5	-2±3	-1±1	-22±6
Region III	+3±1	-0.5±0.6	-0.5±0.5	+2±1
Region V	+1.7±0.5	-0.2±0.3	-1±1	0.5±1
Region VI	-1.9±1.2	+0.6±0.6	0±0	-1.3±1.3
Region VII	-9.4±1.2	+1.6±0.7	0±0	-7.8±1.4
Region VIII	+7±1	-1±0.6	-0.5±0.5	+5.5±1.3
TOTAL				-23±7
Total excl. III+VIII				-31±6

Table 4.2 Mass Change Rates for each region (Gt/yr) (2003~2012).

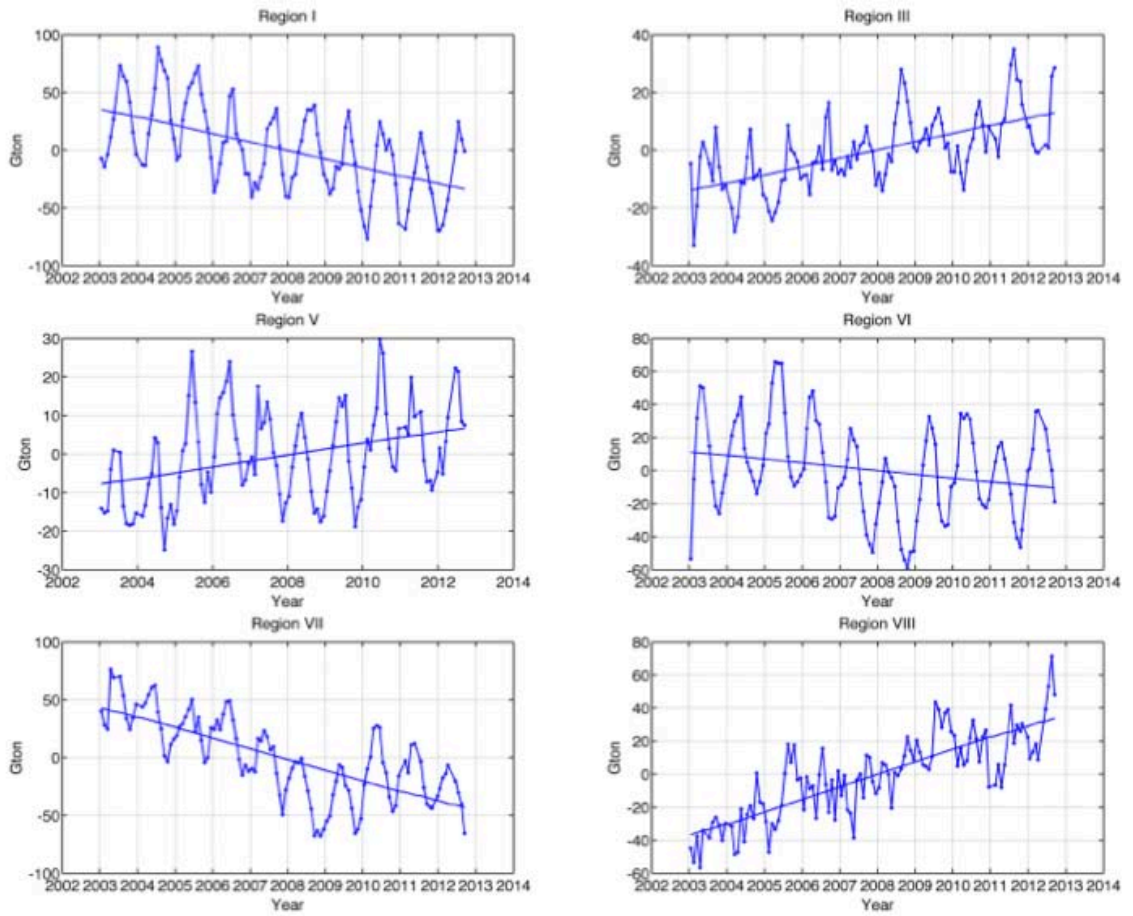


Figure 4.12 GRACE observed mass change for regions in Figure 4.1 except for region II and IV where glacier shrinkage signals are contaminated by ground-water depletion signals over India plains, no corrections are applied except for GIA.

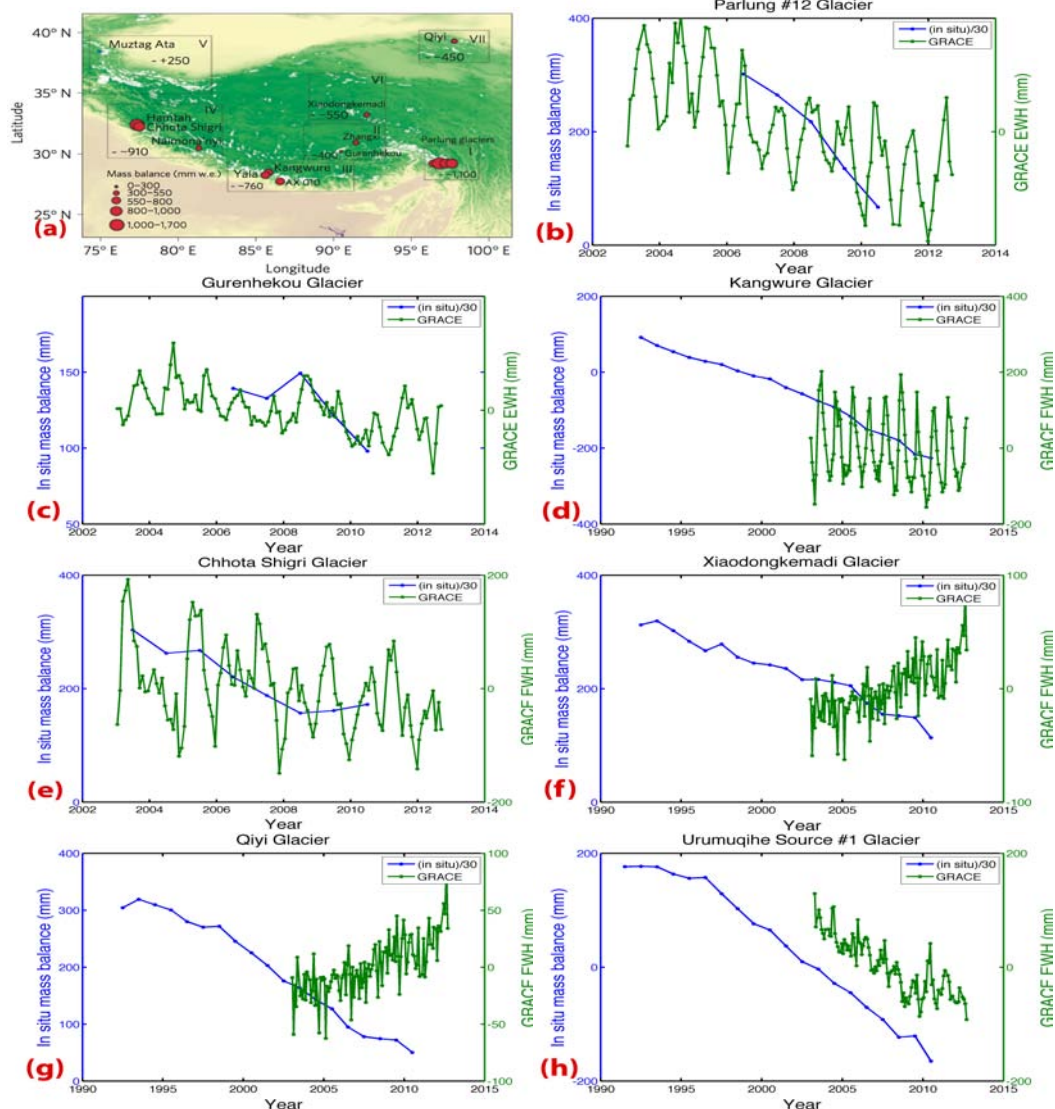


Figure 4.13 a) snapshot from Yao et al., [2012], which shows the distribution of in situ mass balance measurements; green line in b-h) represents GRACEobserved mass changes (mm of EWH) for each $3^{\circ} \times 3^{\circ}$ grid where in situ data locate, blue line shows mass balance from Yao et al. [2012], some random scale factor is applied (1/30 here) just to make the comparison more readable, since GRACE estimates cannot be directly compared to in situ measurements, what we want to show is just how these two kinds of measurements agree with each other representing glacier status in HMA. Note Urumuqihe Source No.1, which is located in Tien Shan and not shown in a) is also included here.

Region III locates in the Qiangtang Plateau, a characteristic endorheic basin. Over 25,000 km² of lakes distribute in the Qiantang Plateau, most of them with area large enough to be detected by satellite altimetry, have shown lake level rising since the early twenty-first century. The lake level of Siling Lake, with surface area of ~ 1865 km² rose

over 5 meters during the GRACE time span (Figure 4.16). Lei et al. [2013] shows six closed lakes (Siling Lake, Nam Cuo, Pung Co, Darab Co and Zigo Tangco) expanded by 20% in area, by 8.7 m in water depth, and by 37.7 Gt in the total storage between 1976 and 2010, with remarkable acceleration after 1999. The main cause for this increasing surface-water trend is increased precipitation in this region for the past decade and decreased lake evaporation. Glacier mass loss also contributed to the lake level rise of glacier-fed lakes (Siling Lake, Nam Co and Pung Co). GRACE observed time series over this region reflect mainly the interannual variability related to yearly precipitation (Figure 4.12b), e.g., the GRACE 2011 anomaly, which has obvious contribution to the least-square-fitted trend estimation, is a direct response of increased precipitation in 2011 based on the yearly difference of total precipitation between 2011 and 2010 observed by Tropical Rainfall Measuring Mission (TRMM) [Huffman et al., 2007] (Figure 4.5).

Region VIII includes the Qaidam basin and part of the Three Rivers' Headwaters (TRH, i.e. the headwaters of Yangtze, Yellow and Mekong rivers). Despite the tectonic process of the Qaidam basin and surrounding mountain ranges as the margin area of TBP [Molnar and Tapponnier, 1978], increasing precipitations in this endorheic basin and the surroundings would contribute to the mass gain signal in Region VIII measured by GRACE. Three Rivers' Headwaters, the *Water Tower of China*, has large area of rivers, lakes and swamps distributed. The total area of wetland in TRH exceeds 70,000 km², and it has been keep expanding since 2005, after years of shrinkage, as a result of increased precipitation. The mass gain rate map in Region VIII actually contains two different processes with respect to those two geographic characteristics. The time series over Qaidam basin and the surroundings (Figure 4.17) show a steadily increasing trend. No obvious seasonal variations in the time series is because of the dry desert climate over this region and the limitation of the accuracy of GRACE monthly solutions. Precipitation data from Global Precipitation Climatology Project (GPCP) [Adler et al., 2003] and TRMM confirm the increasing precipitation in this region since 2005 (Figure 4.14 and 4.15). Area with positive mass rate located in the TRH has the similar time series pattern as those of Region III, Years with increased precipitation (2005 and 2009) are the main reason that yields the positive mass rate. Satellite detected lake level changes [Crétaux et al., 2011] also show lake level rise with respect to increased precipitation, especially in year 2005 (Figure 4.16). Although 300 km apart from each other, the Qinghai Lake and Ngoring Lake both show similar pattern of lake level rise as of GRACE observed mass variations in region VIII, which indicates that the vastly distributed lake wetlands have been recovering, recharged by increased precipitation in 2005, after years of shrinkage.

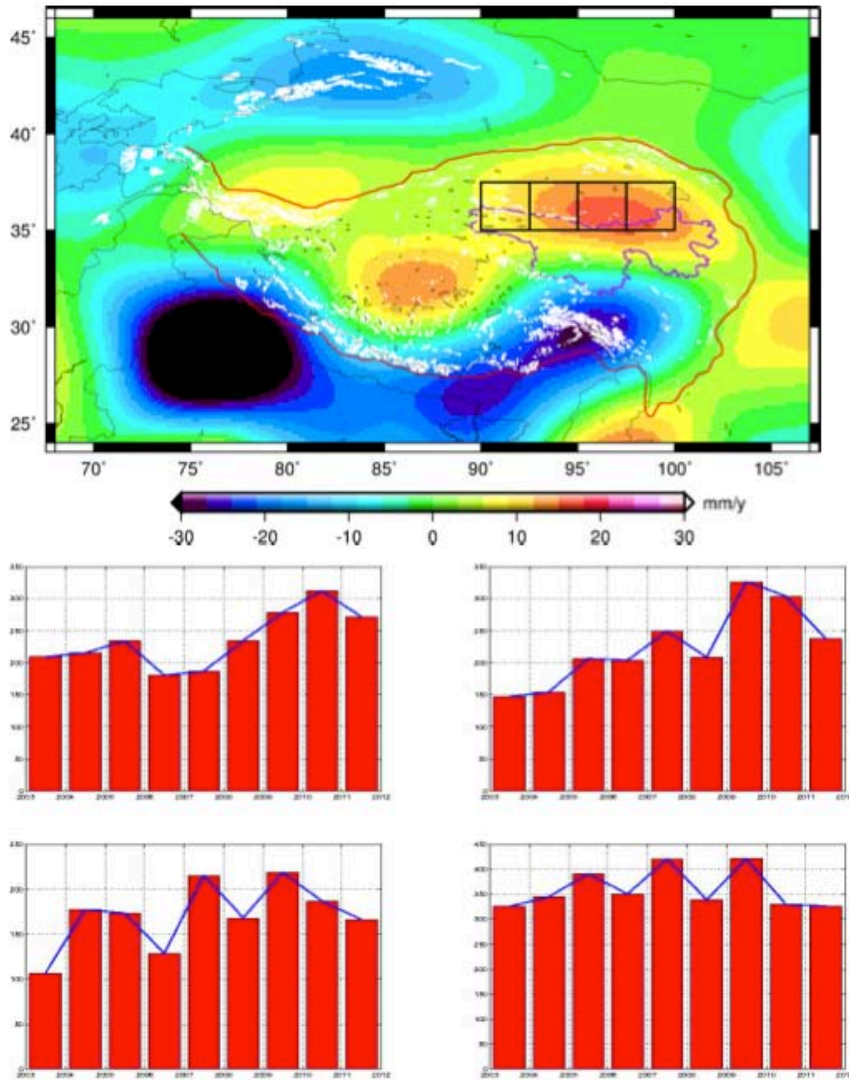


Figure 4.14 Precipitation changes in region VIII. a) shows GRACE observed mass trend map with 4 black boxes chosen to show how annual precipitation changes in this regions, the size of each box is $2.5^{\circ} \times 2.5^{\circ}$, which is the original resolution of GPCP product. b), c), d) and e) represent yearly total precipitation changes from GPCP for each box from left to right.

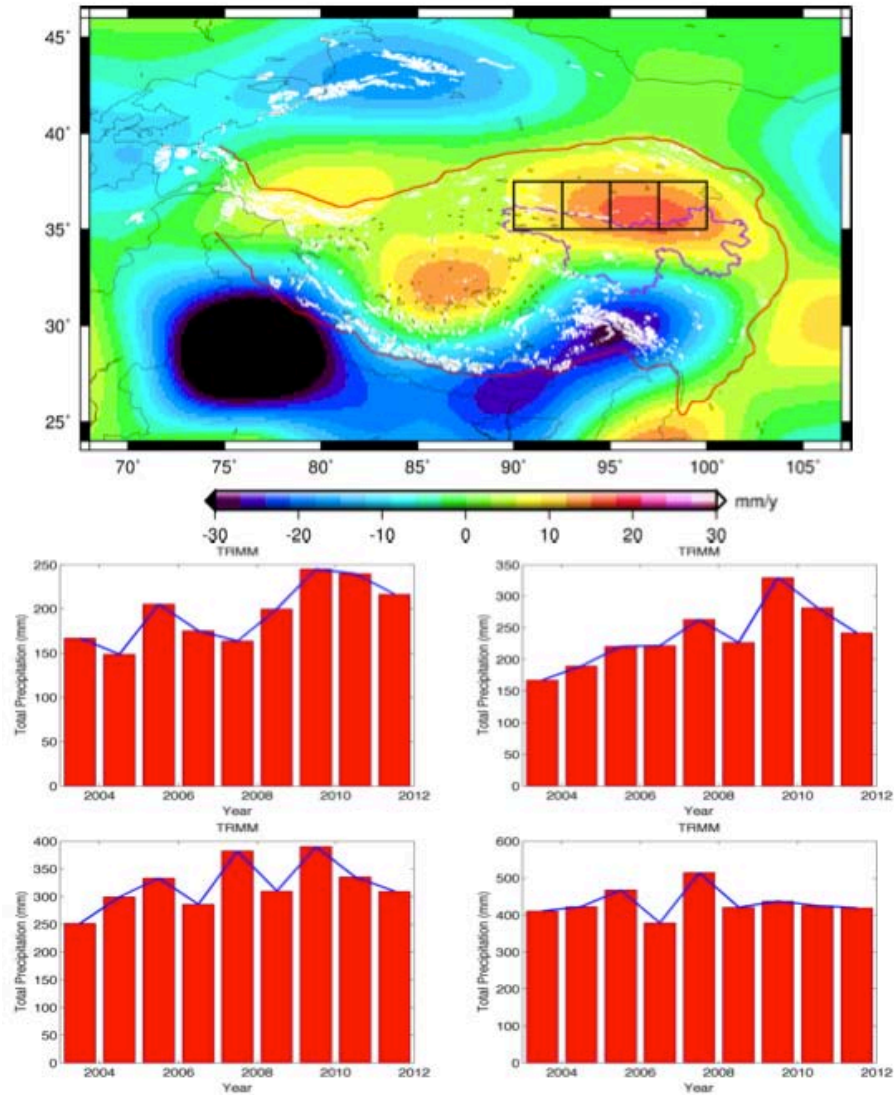


Figure 4.15 Same as Fig. 4.7, but showing precipitation changes from TRMM.

Total mass gain rate of Regions III and VIII is +10 Gt/year based on our estimation, our mass change time series match well with the mascon solution for “Tibet and Qilian Shan” region in Jacob et al. [2012] (Figure 17). The glaciated area of these two regions is around 10,000 km² according to the most updated Randolph Glacier Inventory (RGI). Glacier mass gain rate of +7.5 Gt/year (the sum of Region III and VIII in Table 4.2) means at least 700 mm of precipitation over all the glacier covered regions should be transformed into glacial ice each year, which is not possible, given the total annual precipitation (less than 300 mm on average) over these regions. Lakes and wetlands over these regions have much larger area than glaciated regions, their responses with respect to increasing precipitation are not, or at least not totally, simulated in those

hydrology models. Altimetry detected lake levels, although sparsely distributed, represent the overall trend of increasing water contents within these endorheic basins. Therefore, we conclude that the +7.5 Gt/yr mass gain signal in Region III+VIII is from hydrology contributions which are not correctly simulated in the hydrology models we applied. And the positive glacier mass balance of ~ 7 Gt/yr in Jacob et al. [2012] is from the misinterpretation of GRACE-derived mass changes for the same reason. Unfortunately, there are still no hydrology models that can supply reasonable hydrologic mass changes estimates over Tibetan interior, partially because of poorly determined precipitation. And, limited number of altimetry-observed lake level changes are not enough for us to isolate glacier mass changes from surface water contribution. Hence, we cannot give a mass balance estimate for those two regions in this study.

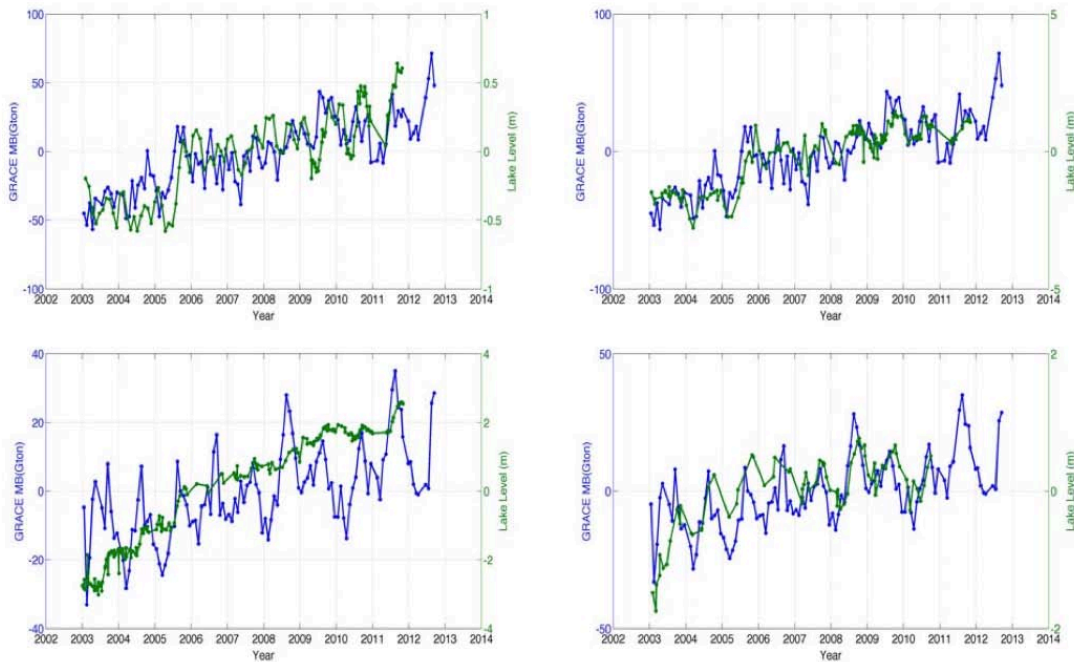


Figure 4.16 Satellite altimetry observed lake level changes, a) Qinghai Lake, b) Ngoring Lake, c) Siling Co, d) Nam Co. Green line shows the lake level changes observed by satellite altimetry, blue line shows GRACE observed mass changes in region VIII (for a and b) and region III (for c and d). Lake level change data credit: HYDROWEB (http://www.legos.obs-mip.fr/en/soa/hydrologie/hydroweb/Page_2.html).

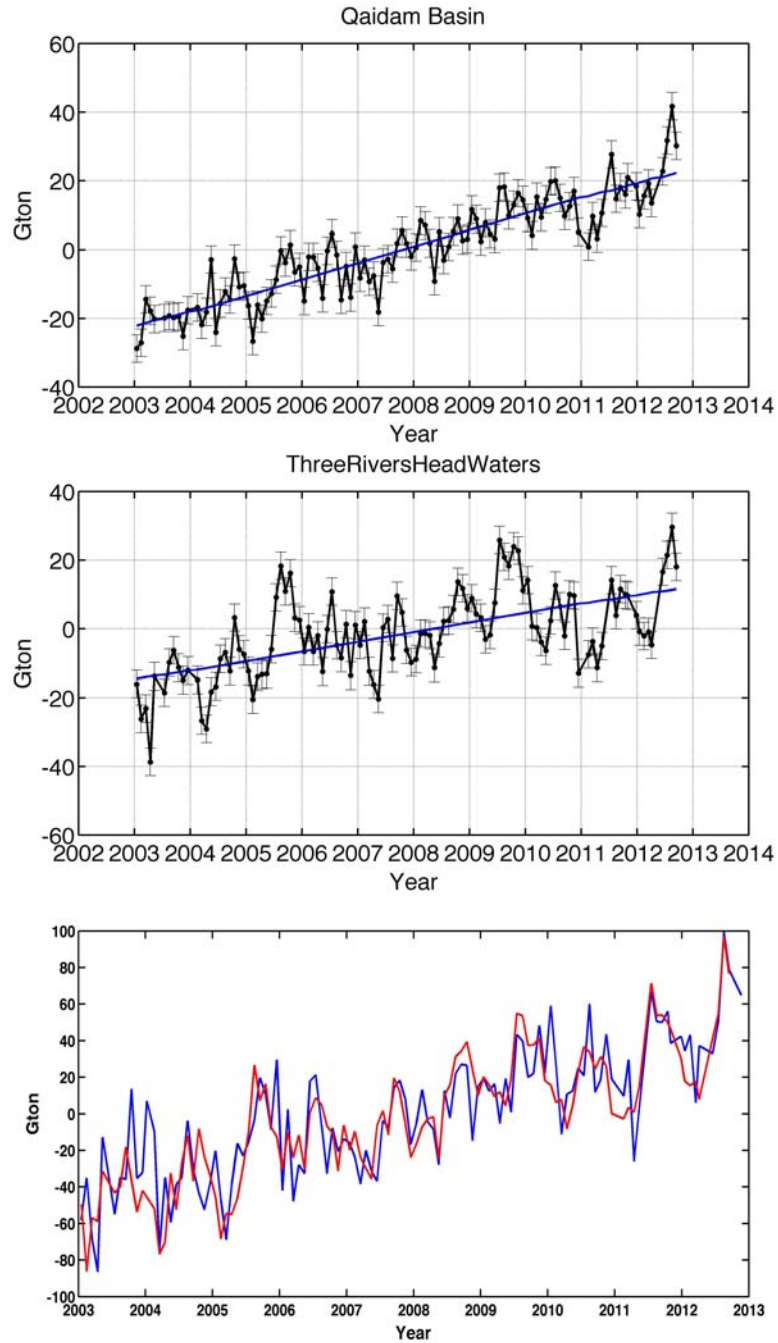


Figure 4.17 GRACE observed mass changes for the Qaidam Basin and the Three Rivers' Headwaters. TOP: Qaidam Basin; MIDDLE: Three Rivers' Headwaters; BOTTOM: red line shows the sum of the top and middle panels, blue line shows the mascon solution of “Tibet and Qilian Shan” in Jacob et al. [2012] we duplicated.

Most of the glaciers in Region I are influenced by high precipitation from Indian monsoon. GRACE observations reveal the most negative mass rate over this region for glacier-covered regions in HMA. Decreased precipitation in 2005 and 2009 contributes

most to mass loss rate (Figure 12a). Limited number of *in situ* measurements from Yao et al. [2012] also confirm the most negative mass balance occurred in 2009 for Parlung glaciers located in this region. Different from glaciers in western Himalaya where estimates of ice mass change are contaminated by leakage from groundwater depletion signals in north-central India, anthropogenic groundwater depletion in this region is relatively small because of low population density and agricultural irrigation water usage. Trend maps derived from NOAH and WGHM hydrology model show decreased water storage in 2005, which is followed by increasing variations. Both models give a slightly increasing trend during GRACE time span (Figure 4.8). Our estimate of mass loss over this region, based on models-corrected GRACE measurements, is -8 Gt/year. Glacier signals in region II and IV are mixed with groundwater depletion signals from the plains of northern India, Pakistan and Bangladesh [Jacob et al., 2012; Rodell et al., 2009; Tiwari et al., 2009]. It is arguably not separable because of the spatial resolution of GRACE monthly gravity fields [Matsuo and Heki, 2010]. We calculate the total mass change rate of region I, II, IV and plains (-49 Gt/year), then remove the plains signal (-30 Gt/year) calculated by adopting the mascon fitting method of Jacob et al. [2012]. Our estimate of total glacier loss over region I, II, and IV is -22 Gt/year.

After several years of continuously decreased precipitation, increased precipitation in 2009 and 2010 slowed down the glacier loss rate in Tien Shan (Figure 4.12e), which is also confirmed by *in situ* measurements (Figure 4.13h). Our GRACE estimate is -7.8 Gt/year for the period January 2003 - December 2011. For glaciers in region V and VI, our results are consistent with contemporary studies which concluded that glaciers in Eastern Pamir, Western Kunlun and Karakoram are relatively stable and in near balance. Glaciers in Region VI have the similar response with respect to inter-annual precipitation variations (Figure 4.12d), we estimate a mass budget of -1.9 Gt/year for this region. As a direct response to increased precipitation in 2005 and 2010, GRACE observed mass changes in Western Kunlun and Karakoram give a net gain of +1.7 Gt/year (Fig. 4.12c).

4.5 Chapter Summary

The status of extensive glaciers in High Mountain Asia (HMA) has been a major public concern because they supplement several river systems in Asia which affect over one billion people. Here we revisit satellite gravimetry derived glacier mass balance by further analyzing possible uncertainties. Our results show that glaciers in this region retreated at a rate of -31 ± 7 Gt/year from January 2003 to December 2011. In addition to the confirmation of most intensive shrinkage in southeastern Tibetan Plateau (TBP) and Tien Shan, and relative stability of Eastern Pamir, Western Kunlun and Karakoram, we find that vastly distributed lakes, wetlands within TBP and their responses as natural reservoirs with respect to abnormal high precipitation in certain years are the main reason causing mass gain signals observed by GRACE, and this effect is not simulated, or at least not fully simulated, in current hydrology models. Therefore, the positive “glacier” mass balance of ~ 7 Gt/yr in Jacob et al. [2012] is from the misinterpretation of GRACE-observed mass changes.

Chapter 5 Mass Balance in Greenland

5.1 Introduction

Changes in Greenland ice mass balance under the climate of global warming is of greatest concern because, as the Antarctic ice sheet, they affect global sea levels and climate changes. Recent studies have confirmed increasing ice melting over Greenland ice sheet since 1990s. Time-variable gravity fields observed by GRACE have been employed to estimate the relative mass changes of Greenland ice sheet since 2002. Compared to other geodetic techniques, advantages of the GRACE satellite mission are that it measures the effect of mass fluctuations directly, provides regional averages of mass changes without the need for spatial interpolation, and permits monthly temporal sampling [Shepherd et al., 2012]. Previously published studies, based on GRACE measurements, have shown that the Greenland ice sheet is losing mass at rapid rate [e.g. Velicogna and Wahr, 2006; Chen et al., 2006; Luthcke et al., 2006; Wouter et al., 2008; Velicogna, 2009; Rignot et al., 2011; Schrama and Wouters, 2011]. Although these estimates of mass balance of Greenland ice sheet are relatively not affected by GIA corrections [Huang et al., 2013], discrepancies still exists between them. Such estimates of the total have varied from -100 to -250 Gt/yr [Harig and Simons, 2012]. A significant share of these differences is due to different time spans of GRACE data those studies applied. Since most of those time spans were short, the best-fitting trends tend to be quite sensitive to variability that was not truly secular, which acted to increase the dependence on the time span. Moreover, different post-processing techniques and analysis methods also contribute to the discrepancies. Since 2012, studies using about one decade of GRACE have revisited estimates of Greenland ice sheet mass balance. Harig and Simons [2012] reported total ice mass change rate of -199.72 ± 6.28 Gt/yr between April 2002 and August of 2011, by applying so-called Slepian functions [Simons, 2009]. Reconciled estimate from Shepherd et al., [2012] showed final GRACE trend result of -230 ± 27 Gt/yr, for the January 2003 – December 2010 time period. The trend result is the average of the trends from six separate groups that computed their time series values, as well as their trends and uncertainties using their own analysis methods. Most recent estimates are from Velicogna and Wahr [2013] and Chen et al. [2013]. Velicogna and Wahr [2013] applied an empirical amplitude scaling factor to correct smoothing-caused signal leakage (see Chapter 2) while estimating Greenland mass changes. Their trend result of mass change for Greenland is -258 ± 41 Gt/yr for January 2003 through Nov 2012. Chen et al. [2013] used a trial-and-error forward modeling approach to avoid leakage effect in their estimate of ice mass changes. They showed the Greenland ice sheet changed in mass by -250 ± 18 Gt/yr between January 2005 and December 2011.

Most of the studies above employed empirical ways to estimate ice mass changes for Greenland, except for Harig and Simons [2012] which shows largest difference with other studies. Here in this study, we present a detailed analysis of Greenland ice mass

changes. To accurately estimate total mass changes for Greenland ice sheet, we employ an efficient leakage reduction method (see Chapter 2.2.3) to reduce signal leakage of mass changes between Greenland ice sheet and its surrounding ocean. This leakage reduction technique can efficiently recover leakage signals by re-scaling the Gaussian-smoothed mass changes mathematically, without introducing in empirical information.

5.2 Study Region

Figure 5.1 shows the Greenland ice sheet drainage divides developed by the Goddard Ice Altimetry Group from ICESat data [Zwally et al., 2012]. The Greenland ice sheet is fringed almost completely by coastal mountains through which it is drained by many glaciers [Rignot and Thomas, 2002]. Based on the coarse spatial resolution of GRACE data, it is unlikely to separate the mass variations of ice sheet from its surrounding small glaciers and ice caps (GIC). Moreover, GRACE observed ice mass loss signals are even not exactly located within the land area, because there are still mass loss signals located in coastal ocean based on our non-smoothed trend map (Figure 5.2). Hence, to best estimate total ice mass variations over Greenland, we expand the mask file used in the leakage repair solution which is introduced in Chapter 2. Also, the Canadian Arctic Archipelago, which are close to the northwestern shore of Greenland, hold one-third of the global land ice outside the polar ice sheets, especially those GICs on the Northern Ellesmere Island. The Baffin Bay between Greenland and Baffin Island is only about 600 km wide. To better determine the ice mass changes in these regions, we combine Greenland together with GICs of the Canadian Arctic Archipelago and Iceland, then calculate their total ice mass balance, the mask file is shown as Figure 5.3.

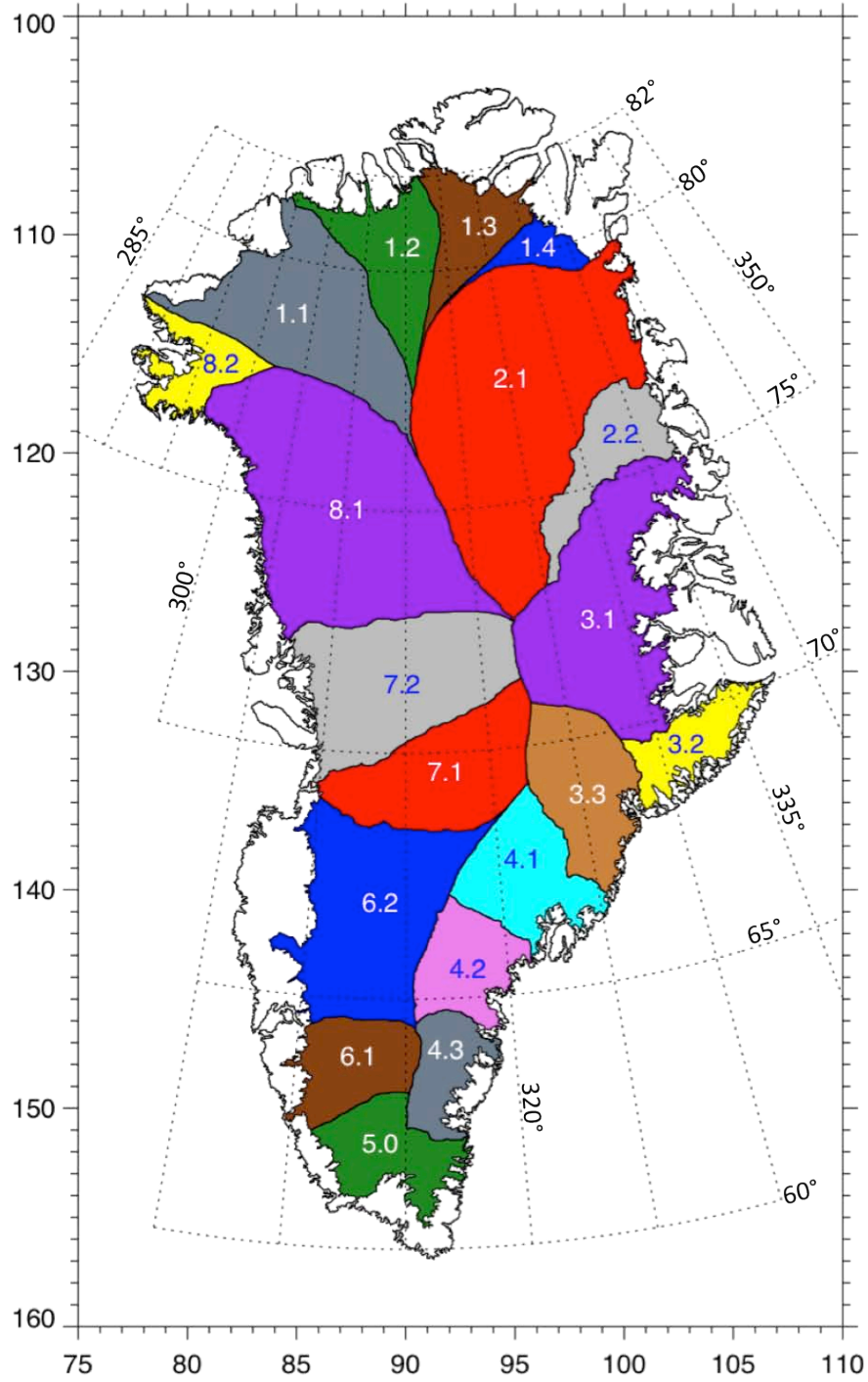


Figure 5.1 Greenland ice sheet drainage divides developed by the Goddard Ice Altimetry Group from ICESat data [Zwally et al., 2012].

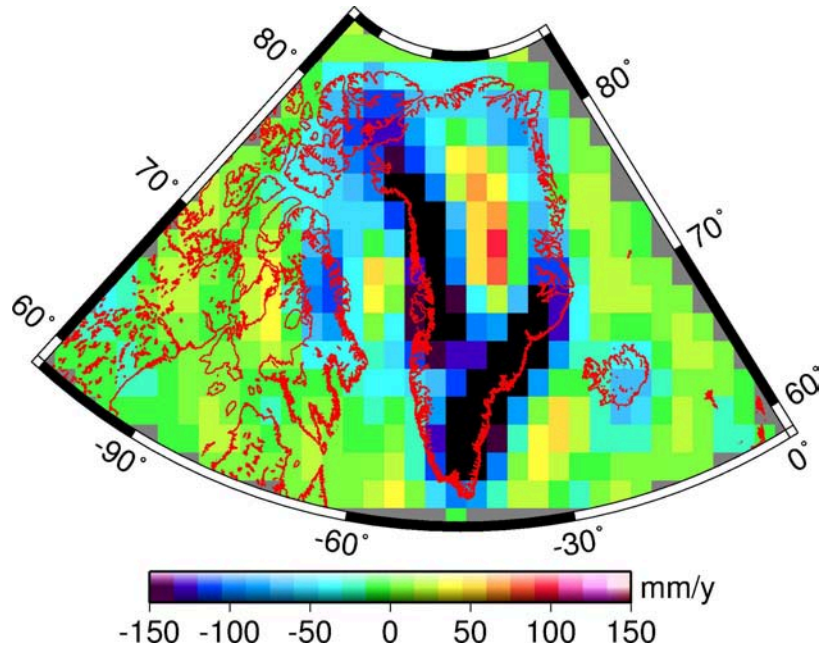


Figure 5.2 Trend map of surface mass changes over Greenland and its surrounding derived from CSR products during Jan 2003~Dec 2012, 3-degree pixels are shown to represent the spatial resolution of GRACE monthly gravity fields.

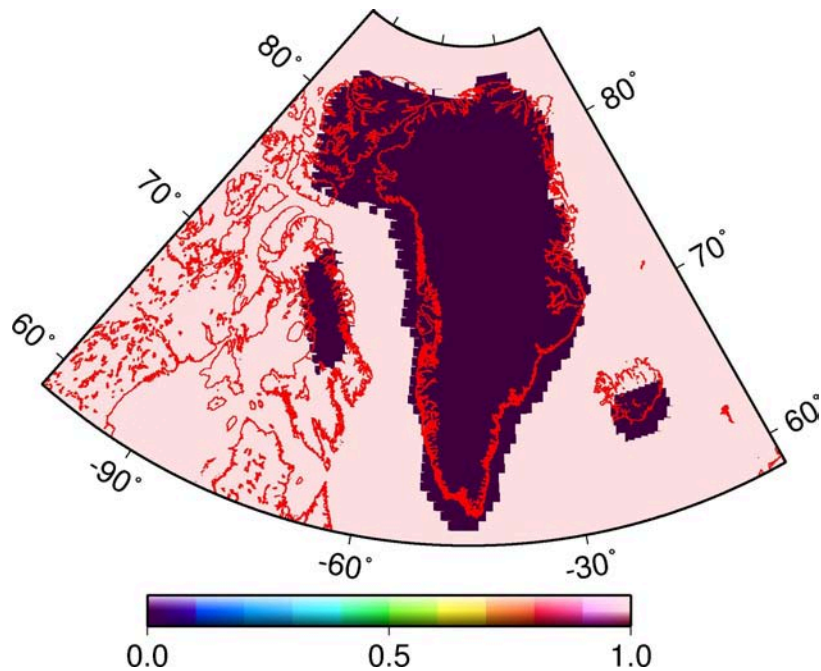


Figure 5.3 Mask file used to correct signal leakage caused by Gaussian smoothing.

5.3 GRACE-determined mass changes

For the GRACE RL05 monthly gravity fields, the noise level is relatively smaller compared to those of RL04, hence we only apply a 200 km Gaussian smoothing to GRACE monthly solutions. Figure 5.4 shows the trend map of ice mass changes during the period between January 2003 and December 2012. From the trend map, we can see that ice mass loss is concentrated along the coast, especially in the southeast and northwest, which is consistent with previously published results using other satellite geodetic techniques, such as satellite radar/laser altimetry. In the interior of Greenland with high elevation, it is evident that there is significant mass gain in those regions. This part is not depicted in previous studies using GRACE to estimate Greenland mass balance. The main reason is that a so-called decorrelation technique is usually applied to remove high-frequency stripes noise in GRACE data, and this technique will cause signal distortion for high-latitude regions. Mass gain signal in Greenland interior is hence removed as decorrelation technique is applied.

Compared to Antarctica, Greenland is strongly affected by surrounding land climate and the North Atlantic. The average accumulation rate reaches about 30 cm/yr, which is twice that for Antarctica [Rignot and Thomas, 2002]; and summer melting occurs over half of the ice sheet surface. To better understand Greenland ice change process, we apply the Empirical Orthogonal Function/Principal Component (EOF/PC) analysis technique to the GRACE data over Greenland region. We expect the main EOFs could depict the spatial patterns of Greenland ice changes and corresponding PC scalars describe their time evolution. We solve 10 EOF/PC modes for Greenland; only the first three modes are of significance in terms of total variance explained, which are presented in Figure 5.5. The leading mode is actually showing the same spatial pattern as the trend map showed in Figure 5.4; its corresponding PC evolution then non-surprisingly gives area-averaged EWH time series. The second mode reflects totally different responses of east and west coasts, its PC evolution reveals the slowdown of ice loss in southeast Greenland, and accelerated mass loss in northwest and northeast portion. The third mode, however, is complicate to explain, hence we calculate the yearly differences, and show them in Figure 5.6.

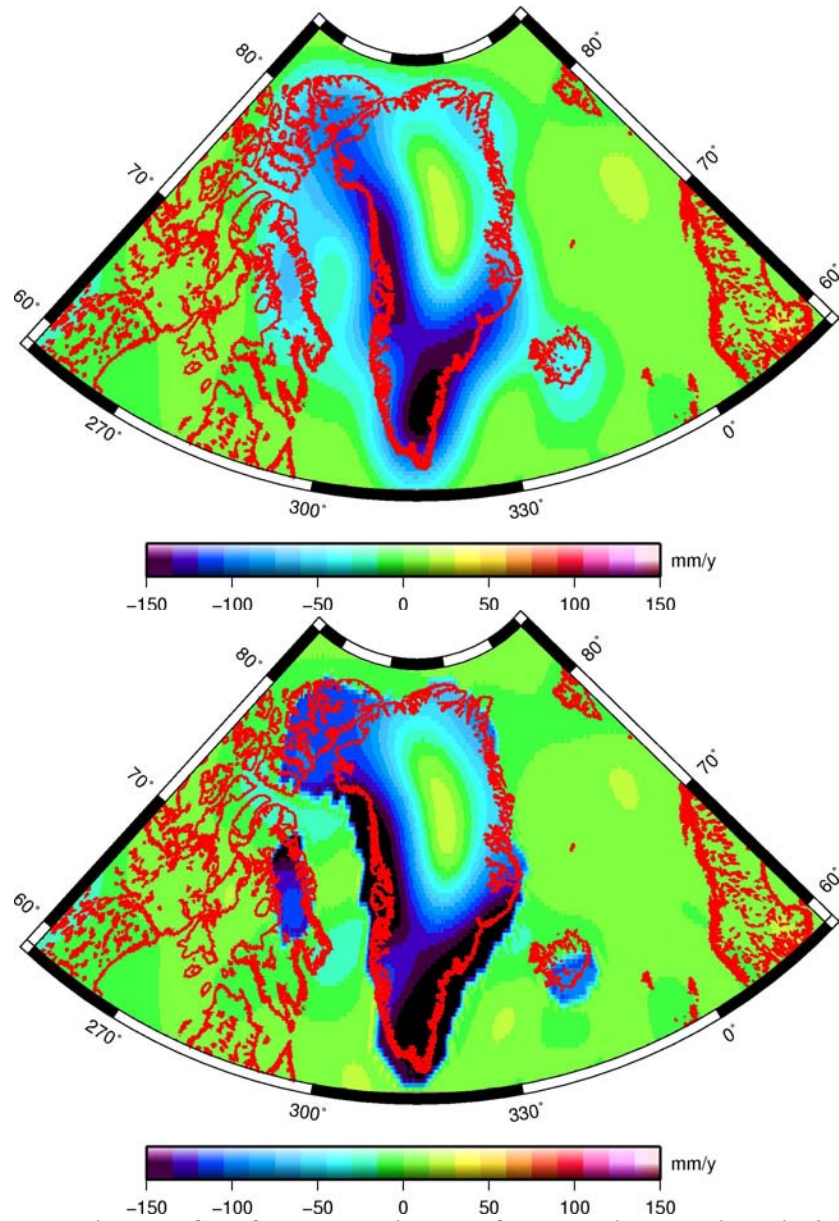


Figure 5.4 TOP: trend map of surface mass changes for CSR data product during Jan 2003~Dec 2012 after 200km Gaussian smoothing; BOTTOM: same trend map but with leaked signal recovered.

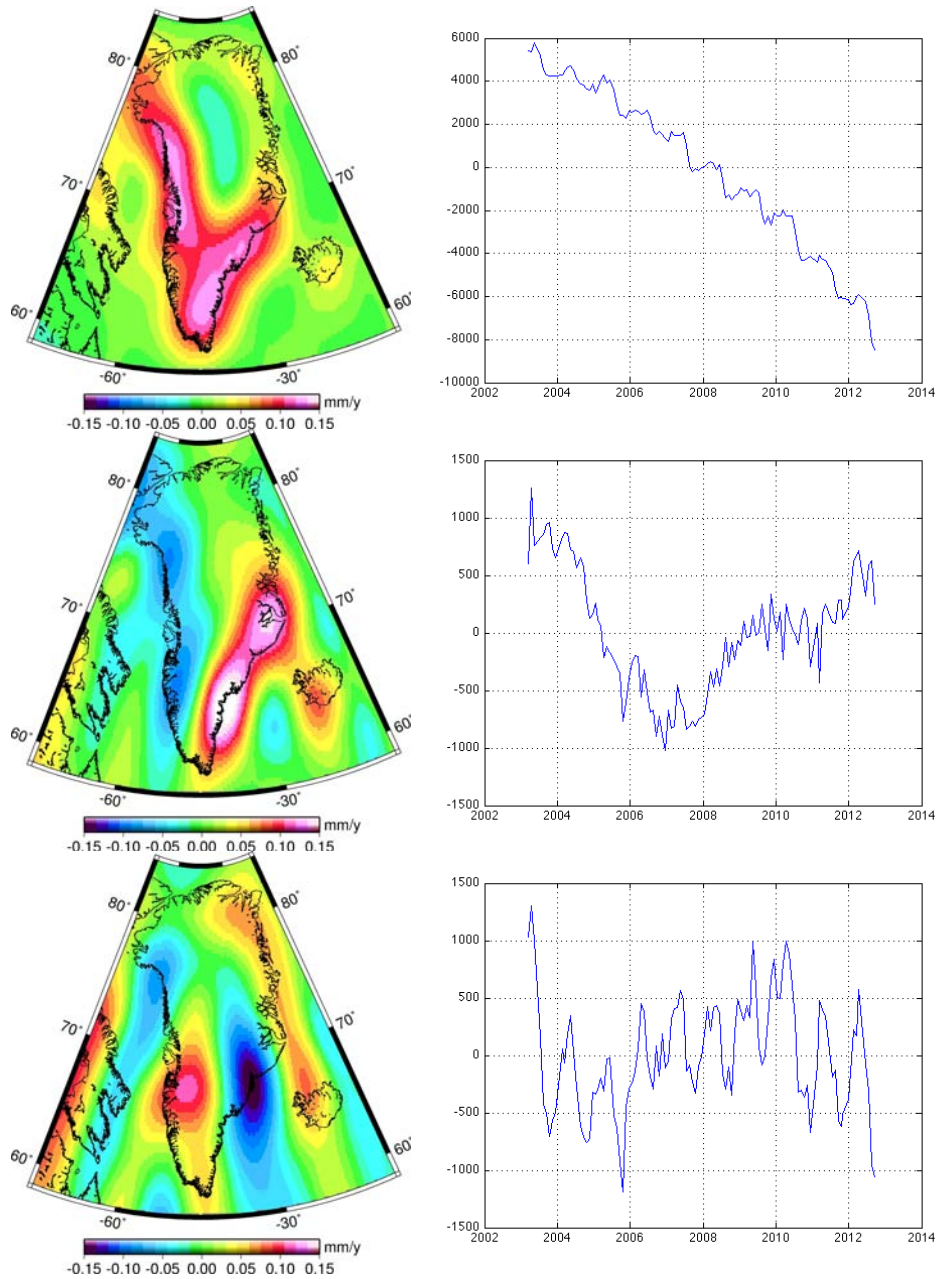


Figure 5.5 The leading three EOFs and their corresponding PC evolutions.

The yearly differences can clearly show the evolution progress of Greenland ice mass changes. From Figure 5.6, we can see that ice sheet and GICs over southeast coast had experienced an accelerated retreating process until 2008. This is especially for basin 3.1, 3.2 and 3.3 in Figure 5.1. We will examine its cause by comparing GRACE measurements with ERA-interim derived P-ET term below. For basin 4.1, 4.2 and 4.3, the slowdown did not last long. Accelerated ice retreat returned in 2010 with the first record-high ice retreat in the 21th century. The 2010 abrupt ice retreat is represented in

both 2009-2010 and 2010-2011 differences in Figure 5.6. Because the yearly difference maps represent the differences of yearly-averaged mass changes, ice loss occurred in the latter half of year 2010 is more pronounced in 2010-2011 difference. For the west coast, ice loss acceleration starts from northwest coast since 2006, then spreads to southwest. After 2010, southwest Greenland dominates the ice losses. Yearly differences with long-term trend removed give more evident views about ice loss evolution in Figure 5.9. We also calculate and plot the yearly differences using GFZ and JPL data sets, the results are shown as Figure 5.7 and 5.8 respectively. Although the results from GFZ and JPL have more noises compared to CSR data, especially for JPL data, they show generally similar ice sheet evolution.

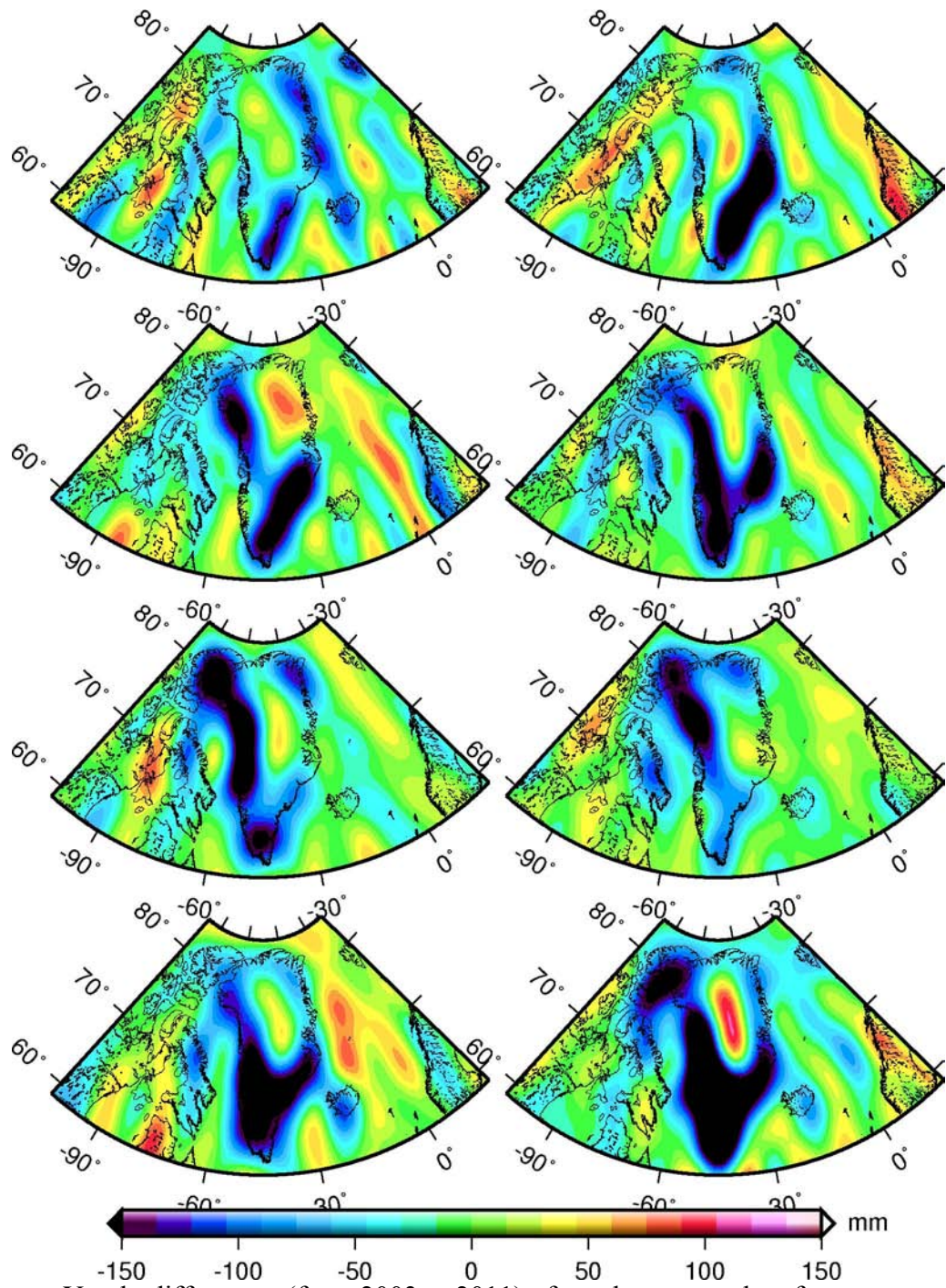


Figure 5.6 Yearly differences (from 2003 to 2011) of yearly-averaged surface mass anomaly (in terms of equivalent water thickness in mm), from CSR data products.

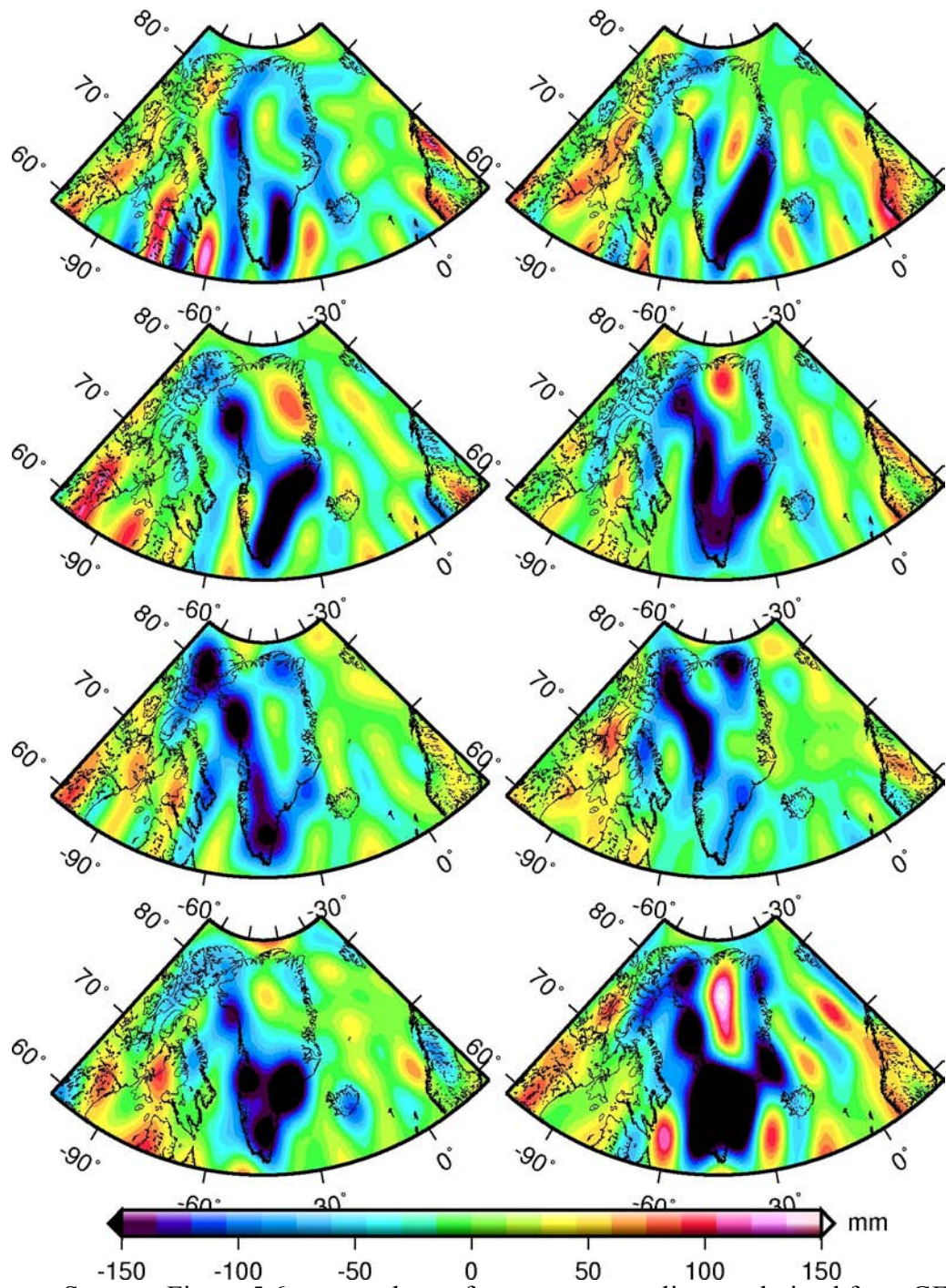


Figure 5.7 Same as Figure 5.6, except the surface mass anomalies are derived from GFZ data products.

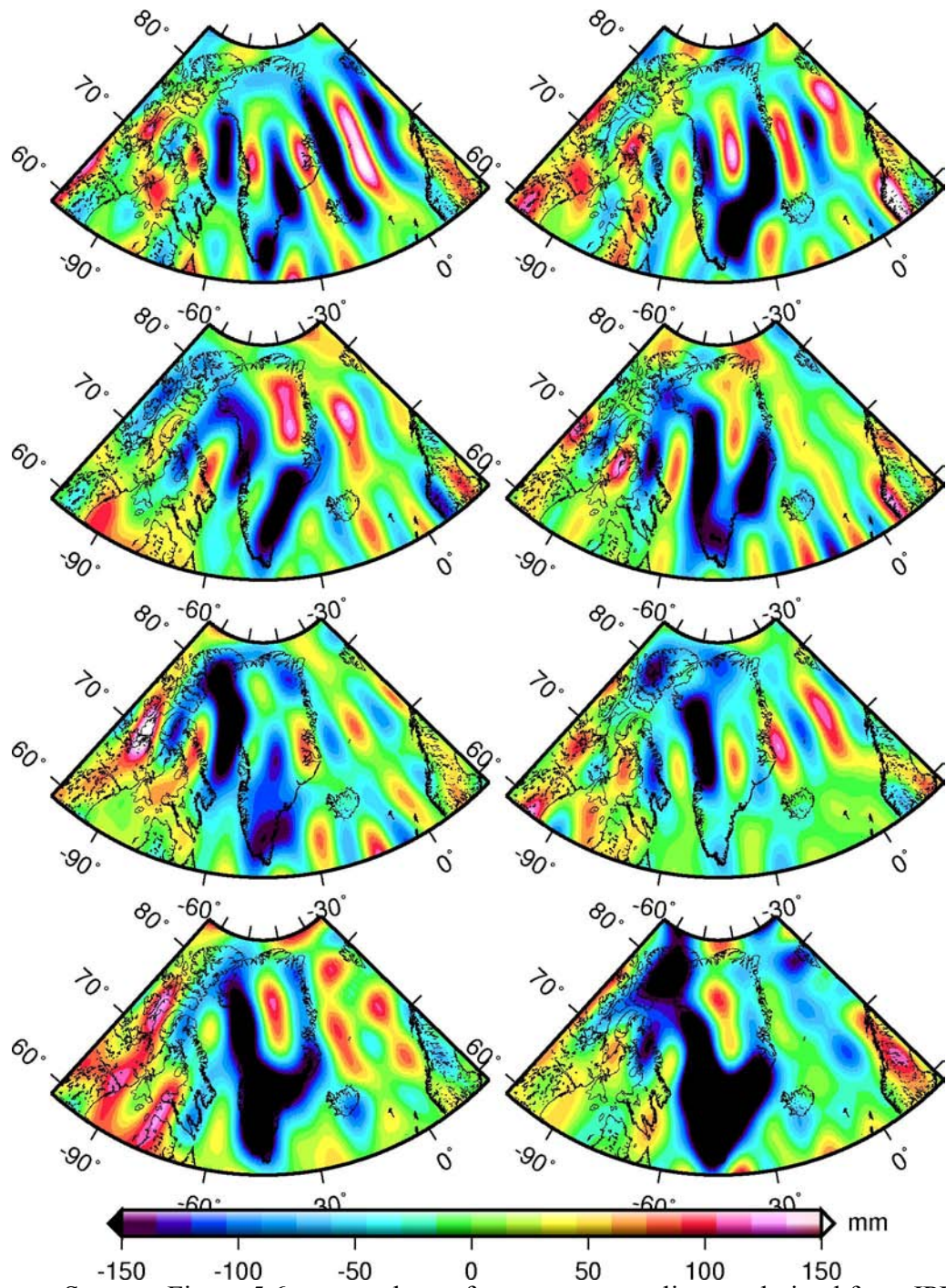


Figure 5.8 Same as Figure 5.6, except the surface mass anomalies are derived from JPL data products.

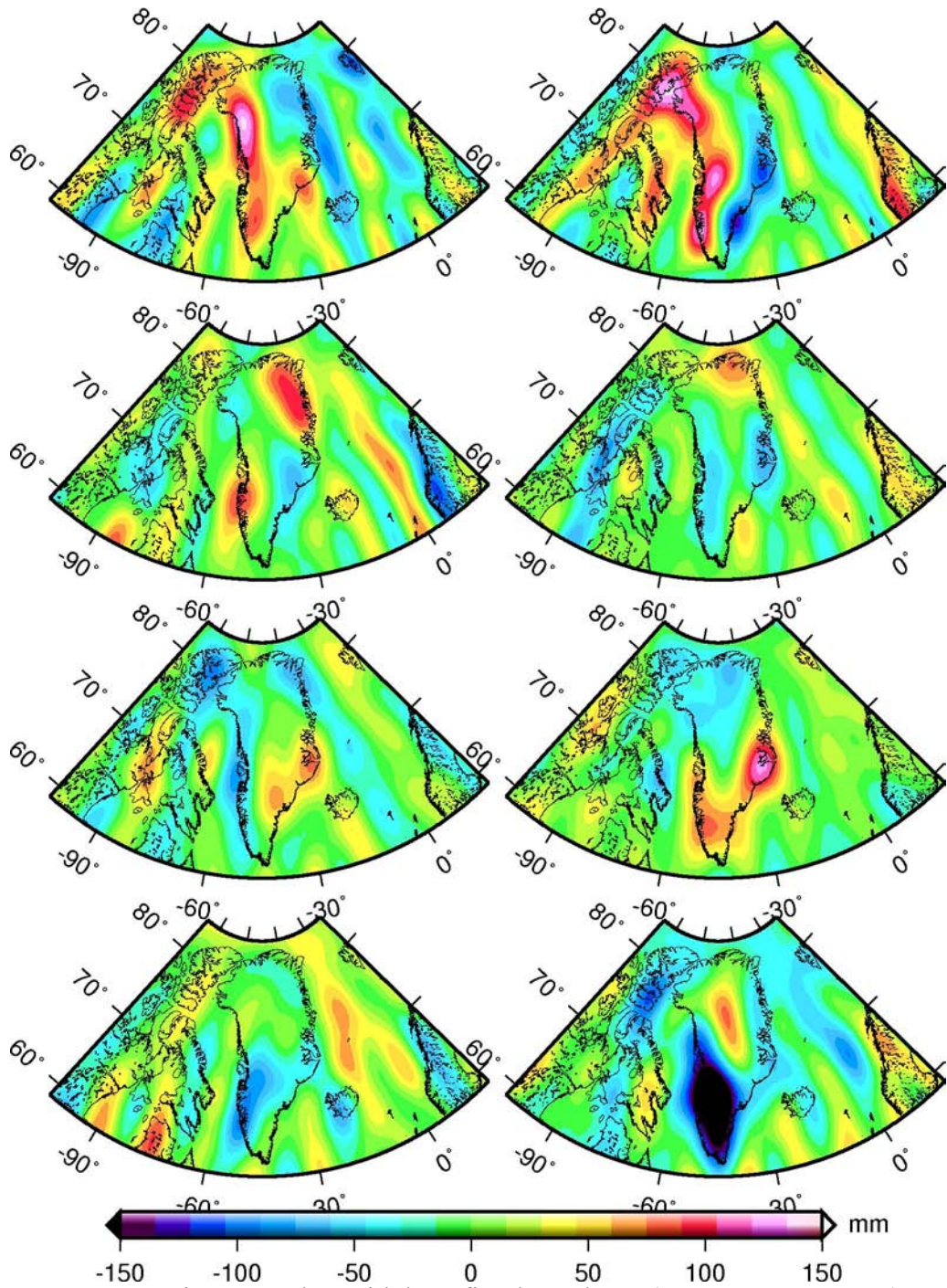


Figure 5.9 Same as Figure 5.6, but with best-fitted trend rate (Jan 2003~Dec 2012) removed from each yearly difference.

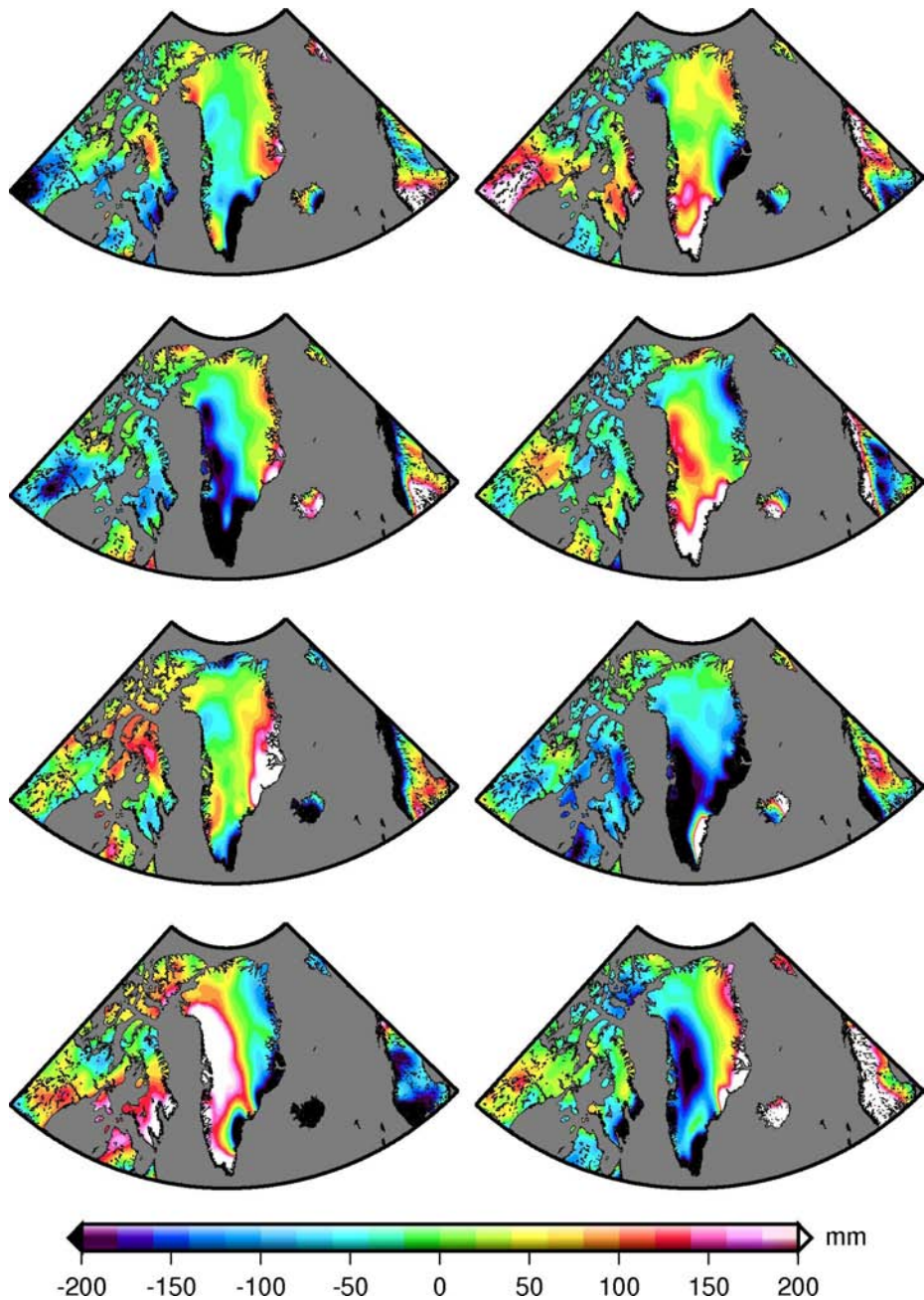


Figure 5.10 Yearly differences (from 2003 to 2011) of annually accumulated precipitation (in terms of equivalent water thickness in mm), from ERA-interim data products.

5.4 Surface Mass Balance

As we mentioned in Chapter 4, what GRACE measures is the relative mass changes as a function of time. For ice sheets, after correction for non-ice effect (i.e., GIA contributions), GRACE-observed mass changes represent ice mass changes $M(t)$. And ice mass balance is defined as the time derivative of $M(t)$, i.e. $dM(t)/dt$. Cogley et al.

[2011] recommend the term ice mass balance for the sum of the surface mass balance (SMB) and the internal mass balance. The surface mass balance is the sum of surface accumulation and surface ablation. Three budgets determine the mass balance of an ice sheet. Neglecting basal melting of grounded ice and assuming the grounding line position to remain unchanged, $dM(t)/dt$ is governed by the difference between SMB and the ice discharge across the grounding line (D) [van den Broeke et al., 2009]:

$$dM(t)/dt = SMB - D \quad 5-1$$

SMB represents net precipitation accumulation (P including snow and rain) minus surface ablation (sublimation (S) and runoff (R)):

$$SMB = P - S - R \quad 5-2$$

SMB data simulated from climate models can help verify remotely sensed data, and extend them into a long climatic perspective, based on meteorological models. However, by definition, SMB estimates do not take into account the mass loss from iceberg calving and basal melting, for which only crude estimates can currently be given. For Greenland, iceberg calving is roughly equivalent to the amount of annual runoff whereas the basal melting is relatively small [Hanna et al, online report: http://www.arctic.noaa.gov/report07/essay_hanna.html]. In this study, we just use the P-S from ERA-interim model output as “pseudo” SMB to evaluate GRACE measurements over Greenland. To do this, we apply a 13-month moving smoothing to dM/dt derived from P-S and GRACE respectively. From the yearly differences of annual total precipitation shown as Figure 5.10, we can see the inter-annual variations of total precipitation are large, especially for low-altitude coastal regions. Based on the spatial characters of GRACE trend map and yearly differences of precipitation, we choose six basins to show the comparisons, which are: Basin 1.1, Basin 2.1, Basin 3.1, Basin 4.2, Basin 6.2 and Basin 8.1. The results are shown as Figure 4.11. We can see that these two data products generally agree well with each other for each basin, except that GRACE data are much noisier. However, for Basin 6.2, GRACE observed mass balance shows large differences compared to P-S since 2009, especially for year 2010 and 2011, which means P-S only is not enough or not accurate enough to explain the mass loss over this region any more. Tedesco et al. [2011] analyze MODIS data, surface observations and outputs from regional atmosphere model, and point out new records in 2010 for surface melt and albedo, runoff, and number of days when bare ice is exposed and surface mass balance of the Greenland ice sheet, especially over its west and southwest regions, i.e., where Basin 6.1 locates. According to Tedesco et al. [2011], early melt onset in spring, triggered by above-normal near-surface air temperatures during May 2010 (up to +4°C above the mean), contributes to accelerated snowpack metamorphism and premature bare ice exposure, hence rapidly reducing the surface albedo; reduced accumulation in 2010,

and anomalously warm June and July temperature anomalies (+1.5°C above the 1979~2009 average) persisted with the positive albedo feedback mechanism contributing to large negative SMB anomalies. Moreover, summer snowfall, which helps to increase surface albedo, was below average; melt during August and September was also exceptional, consistent with low albedo and near-surface temperature anomalies of up to +3 °C, which yields a long ice-melting season.

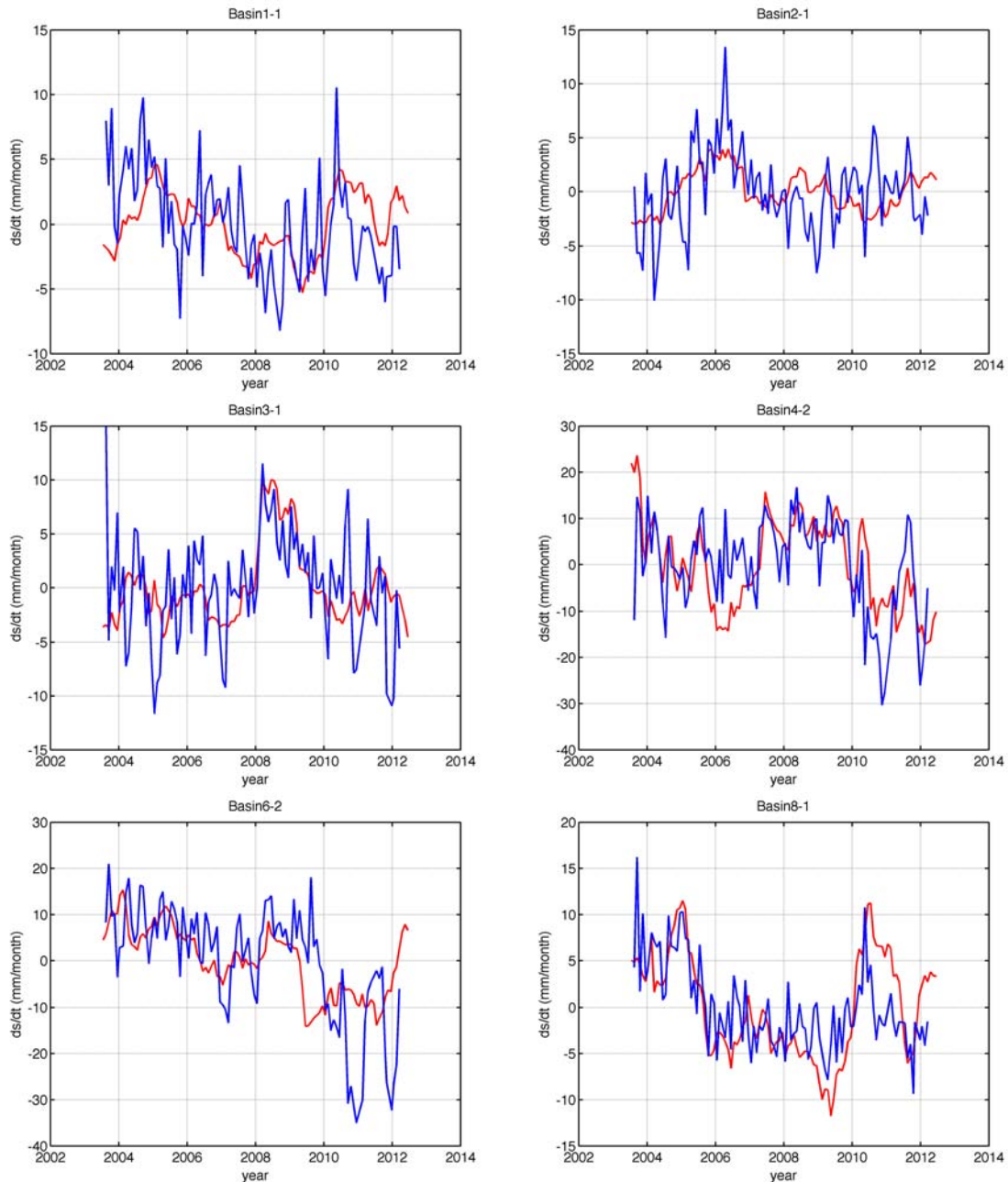


Figure 5.11 Comparison between GRACE derived $dM(t)/dt$ and P-S anomaly from ERA-interim, for selected drainage basins in Greenland, all the time series are averaged using a 13-month sliding window.

5.5 Results

Figure 5.12 shows time series of ice mass changes for Greenland estimated from 3 GRACE data products for period Jan 2003 ~ Dec 2012. Although JPL product seems the noisiest data by comparing yearly differences above, the time series show better agreement with CSR product, and the ice mass loss rate, -265 Gt/yr, agree well with CSR estimate of -267 Gt/yr. With about 10 Gt/yr difference from CSR and JPL estimates, the ice mass balance we estimated using GFZ data is -256 Gt/yr. To get the final estimate of mass change rate of Greenland ice sheet, we choose the CSR estimate as our final result. We follow the same procedure described in Chapter 2.3 to calculate the standard deviation of GRACE-derived ice mass change rate, and choose 2σ value as the uncertainty. As described in Chapter 4.2, the uncertainty from GIA correction is estimated based on the differences between Paulson07 and Peltier's ICE-5G (VM2) GIA model. We calculate the EWH differences between those two models for each grid cell located in the area ($55^{\circ}\text{N}\sim 88^{\circ}\text{N}$, $105^{\circ}\text{W}\sim 20^{\circ}\text{E}$), then calculate their standard deviation, σ_h . $2\sigma_h$, multiplied by the area of Greenland ice sheet, is used to represent the uncertainty of GIA correction. Our final estimate of ice mass change rate over Greenland, from Jan 2003 to Dec 2012, is -267 ± 10 Gt/yr, which is equivalent to sea level rise of 0.74 ± 0.03 mm/yr (assuming that 360 Gt ice corresponds to 1 mm of sea level rise [Shepherd et al., 2012]).

To determine the yearly mass balance values determined by GRACE, we calculate the differences between the beginning and end of each year. For year 2004 to 2011, we calculate the mean value of last December, this January and February, and the mean value of November, December and next January, the difference between them is considered as mass balance of this year. For year 2003, the mass balance is calculated as the difference between the mean values of the first three months of 2003 and 2004. Difference between the mean values of the last three months of 2011 and 2012 is considered as 2012 mass balance. Final mass change results are shown in Table 5.1 below. We can see obviously accelerated ice melt in 2010, 2011 and 2012. The mass loss estimates are around twice those for years before 2010. Ice mass retreat in 2012 reaches a new record-low value of -517 Gt based on the estimate from CSR product.

Harig and Simons [2012] also estimated the values of mass change per year based on their estimates by using the Slepian function. However, their results show almost the same ice mass balance for 2008, 2009 and 2010. Previous publications already confirmed that the year 2010 had record ice-sheet melt and runoff [Box et al., 2010; Mernild et al., 2011; Tedesco et al., 2011 and Hanna et al., 2013], Hence, it is unlikely to be true that year 2010 has the same ice mass balance as 2008 and 2009. Also, the Slepian solution might underestimate Greenland's ice loss between April of 2002 and August of 2011 (-199.72 ± 6.28 Gt/yr).

Time series of glacier mass changes over Iceland and Canadian Arctic are also calculated and shown in Figure 5.12 to Figure 5.14. Ice mass balance rates from three data center generally agree well with each other for different glacier system. Total estimate of glacier mass change rate reaches -70 Gt/yr for 2003~2012.

Other major mountain glacier systems show small discrepancies in previously published estimates, and the results are less controversial. We estimate glacier mass

balance and 2σ uncertainties of Alaska and Patagonia glacier systems by applying the same procedure as for HMA. The final results including major mountain glacier systems are shown in Table 5.2.



Figure 5.12 Time series of ice mass changes for Greenland estimated from 3 GRACE data products for period Jan 2003 ~ Dec 2012.

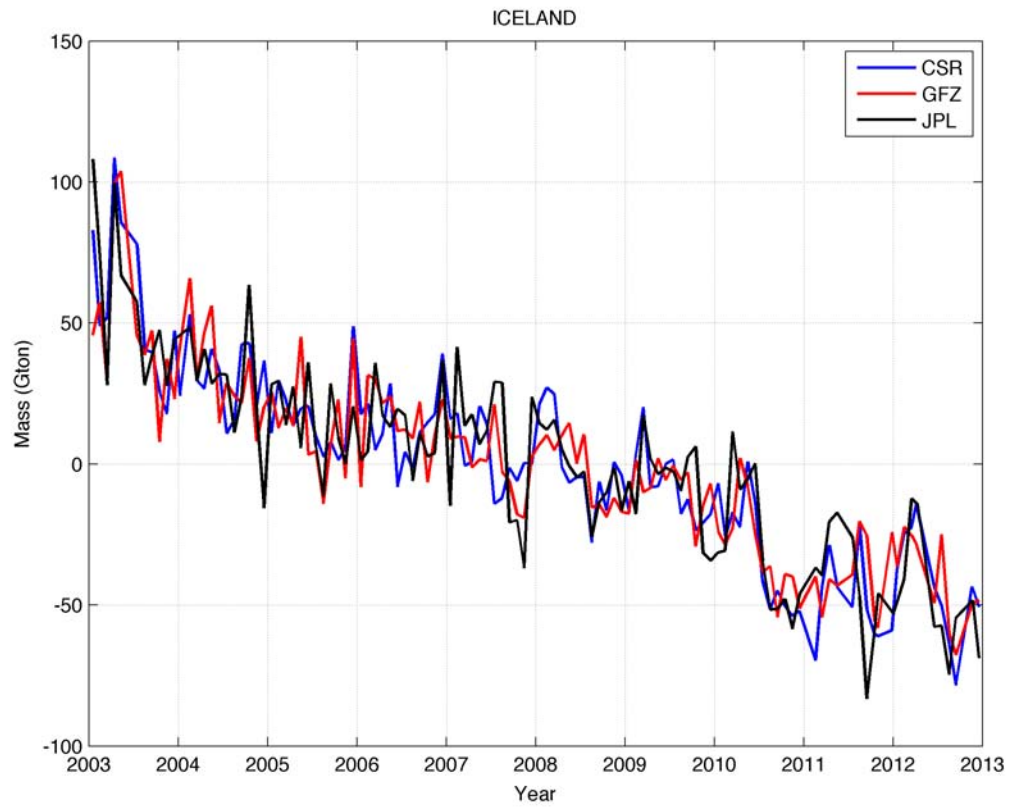


Figure 5.13 Time series of ice mass changes for Iceland glaciers estimated from 3 GRACE data products for period Jan 2003 ~ Dec 2012.

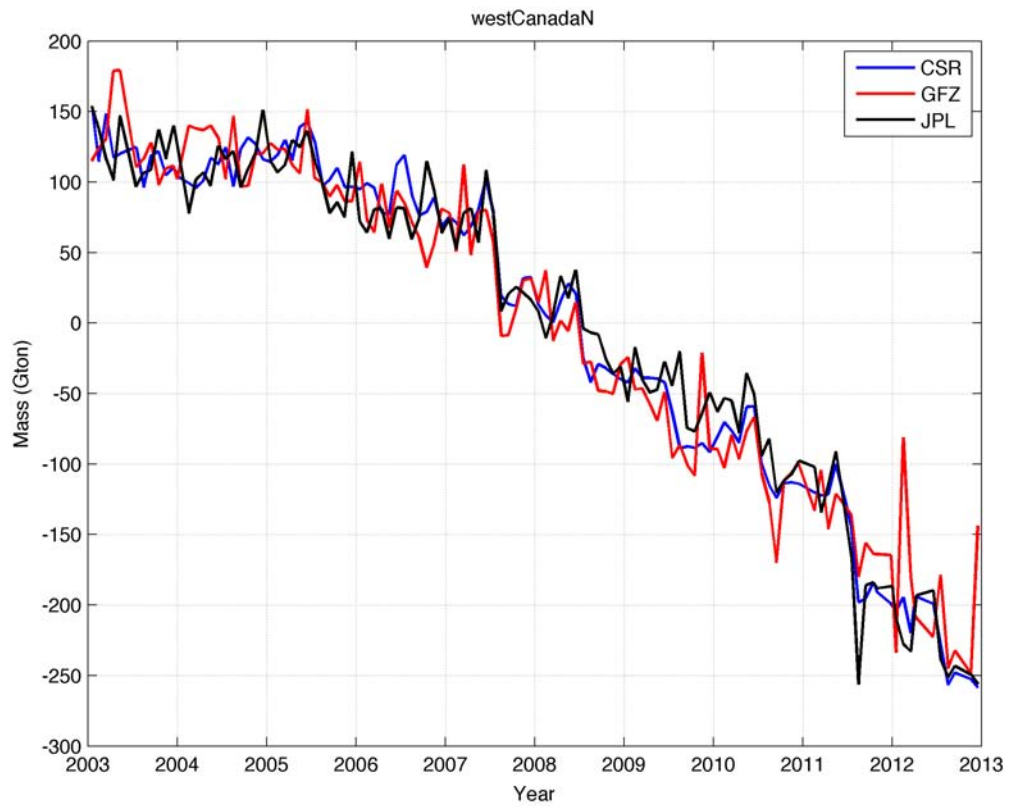


Figure 5.14 Time series of ice mass changes for glaciers over North Canadian Arctic (Ellesmere Island) estimated from 3 GRACE data products for period Jan 2003 ~ Dec 2012.

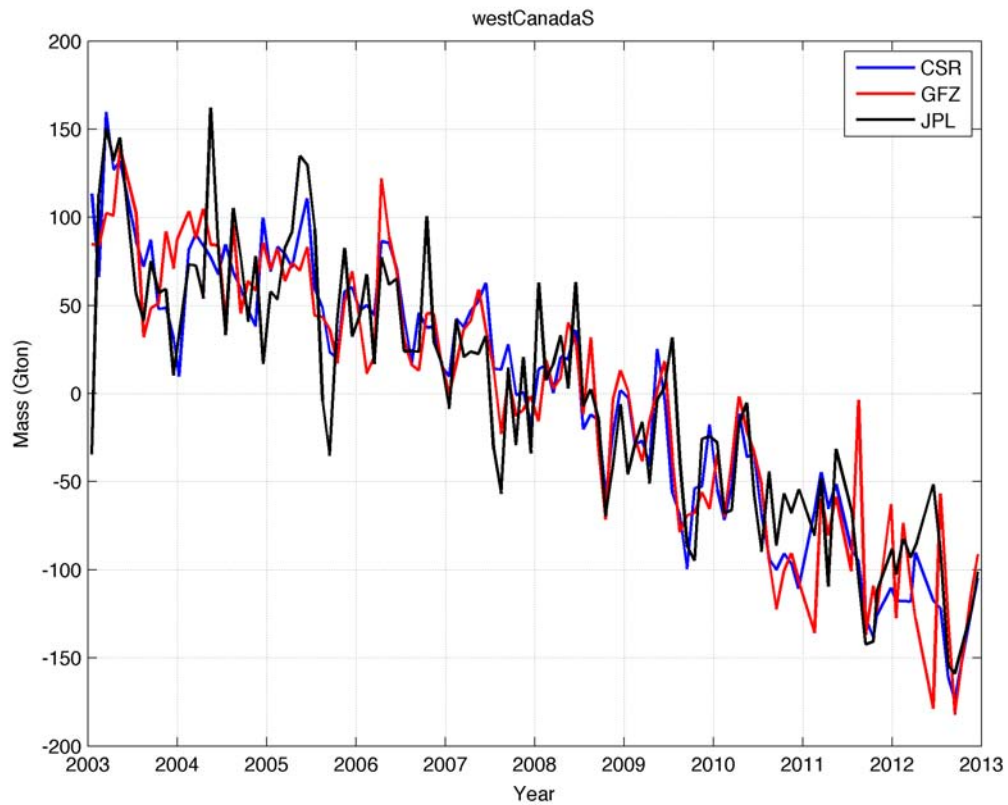


Figure 5.15 Time series of ice mass changes for glaciers over South Canadian Arctic (Baffin Island) estimated from 3 GRACE data products for period Jan 2003 ~ Dec 2012.

	2003	2004	2005	2006	2007	2008	2009	2010	2011	2012
CSR	-181	-191	-196	-234	-250	-189	-265	-430	-405	-517
GFZ	-262	-175	-206	-266	-298	-177	-261	-336	-324	-422
JPL	-125	-227	-206	-217	-201	-207	-249	-457	-389	-496

Table 5.1 Yearly Resolved Ice Mass changes over Greenland (Gt).

Region	Mass Budget (Gt/yr)	Sea Level Rise (mm/yr)
Alaska	-44±4	0.12±0.01
Iceland	-11±2	0.03±0.00
Canadian Arctic	-63±4	0.18±0.01
High Mountain Asia	-31±6	0.09±0.02
Patagonia	-22±3	0.06±0.01
TOTAL	-171±9	0.48±0.02

Table 5.2 Estimates of major glacier mass changes from GRACE for Jan 2003–Dec 2012.

Chapter 6 Antarctic Ice Mass Balance

6.1 Introduction

The Antarctic ice sheet (AIS) holds more than 30 million km³ of ice, which is 90% of the world's ice or ~70% of global fresh water. Complete melting of the Antarctic ice sheet can raise global sea level by 60 m. Hence, quantifying Antarctic ice mass balance is of considerable societal importance, and is a key issue in understanding changes in global mean sea level rise. Compared to Greenland, Antarctic ice sheet mass balance is even harder to estimate because it is far larger, more remote, and not well covered by most of existing satellites [Rignot and Thomas, 2002]. Satellite geodesy techniques provide most of the contemporary continent-wide observations for Antarctic ice sheet mass. Antarctic ice-sheet contributed global sea level rise ranges from -0.12 to 0.17 mm/yr based on previous studies using InSAR and satellite radar altimetry [Davis et al., 2005; Thomas et al., 2004; Wingham et al., 2006; Zwally et al., 2005].

GRACE has its advantages to measures AIS mass fluctuations directly with unprecedented spatio-temporal resolutions near-global coverage. However, a key challenge is to discriminate ice mass fluctuations from other geophysical causes, which mainly refer to Glacial Isostatic Adjustment (GIA). GIA correction introduces considerable uncertainty (up to 130 Gt/yr) into AIS mass balance estimates determined by GRACE, when different GIA models are used for correction [Shepherd et al., 2012]. Earlier estimates of AIS mass balance have varied from -140 to -250 Gt/yr depending on different GIA model corrections. In 2012, two new models (W12a [Whitehouse et al., 2012] and IJ05_R02 [Ivins et al., 2013]) were introduced for GIA correction over Antarctic, with much smaller magnitude compared to previous models. King et al. [2012] estimated a continent-wide ice mass change of -69 ± 18 Gt/yr (from August 2002 to December 2010) by using W12a GIA model; and reconciled estimates from Shepherd et al. [2012] show Antarctic ice sheet changed in mass by -81 ± 33 Gt/yr (from January 2003 to December 2010) based on W12a and IJ05_R2 models. Velicogna and Wahr [2013] followed this trend and reported changes of -83 ± 49 Gt/yr (from January 2003 to November 2012) based on IJ05_R2 model applied. On the other hand, Chen et al. [2013] remained their previous estimates and reported Antarctic rate of -180 ± 94 Gt/yr (from January of 2005 to December of 2011).

Besides large uncertainties caused by GIA correction, different analysis methods and other error sources also limit the accurate estimates of AIS mass balance. In this Chapter, we aim to produce appropriate estimates of AIS mass balance, along with detailed analysis of major error sources.

6.2 Ice Mass Balance Observed by GRACE

Ten-year GRACE monthly gravity field data are available now for estimating Antarctic ice sheet mass balance. To analyze GRACE estimated ice mass changes, we use common definitions of the East Antarctic Ice Sheet (EAIS), West Antarctic Ice Sheet,

and Antarctic Peninsula Ice Sheet (APIS). Figure 6.1 shows Antarctic drainage basin systems and the segregation of the AIS into EAIS (shown in red in Figure 6.1b), WAIS (shown in green) and APIS (shown in blue) according to Rignot et al. [2008], based on a 500m resolution ICESat DEM [Zwally et al., 2012]. Same as for Greenland, we do not separate the peripheral glaciers and ice caps from ice sheets while calculating ice mass changes using GRACE because of its coarse spatial resolution.

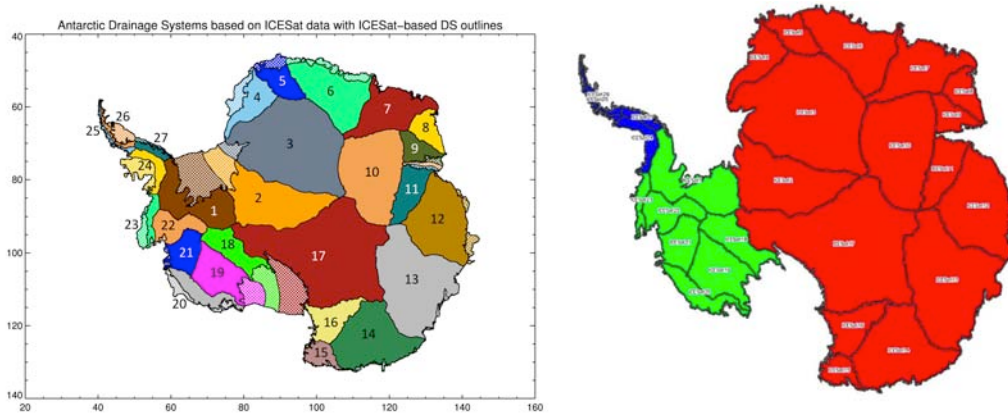


Figure 6.1 Left: Antarctic drainage systems based on ICESat data; Right: the division of the ice sheet into the EAIS (red), WAIS (green) and APIS (blue). Credit: Goddard Ice Altimetry Group [Zwally et al, 2012].

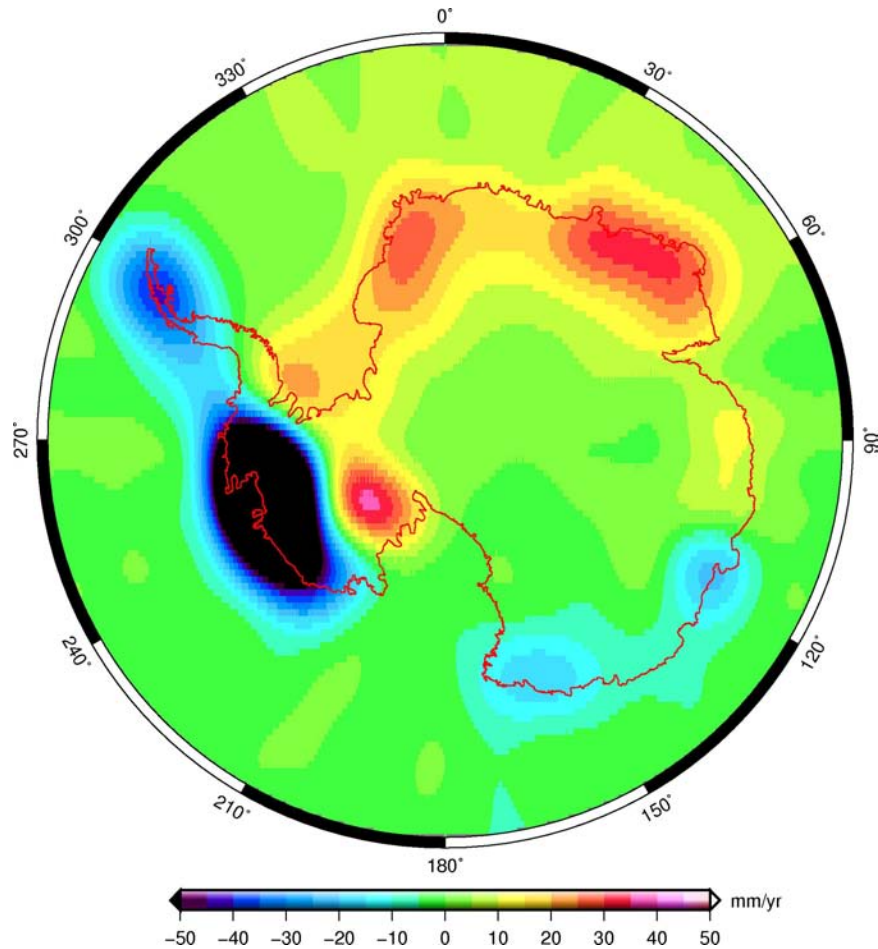


Figure 6.2 Trend map of surface mass changes, in mm/yr of EWH, determined from CSR GRACE monthly gravity fields for Jan 2003 ~ Dec 2012, no GIA correction applied.

We apply 300km Gaussian filtering only to the monthly gravity fields and fit the trend map as Figure 6.2 shows. The trend map shows WAIS and APIS are losing ice during the past decade, while EAIS are gaining mass. We try to examine the spatial-temporal variations of AIS by looking at the yearly differences. Figure 6.3 shows the yearly differences from 2003 to 2011, we can see ice loss in Amundsen Sea sector has been increasing over time, especially after 2007. In contrast, the EAIS, which occupies over 75% of AIS and was in approximate balance throughout the 1990s [Shepherd et al., 2012], has experienced mass gains during recent years, especially in year 2009 and 2011. The abrupt mass increase in EAIS along the coast of Dronning Maud land was caused by anomalously high precipitation events during the Southern Hemisphere winter [Boening et al., 2012]. We will analyze ERA-interim derived P-S over this region later. Yearly difference maps from GFZ and JPL (shown as Figure 6.4 and 6.5 respectively) show similar results, except that JPL product shows more evident stripe noise effect..

EOF/PC analysis (see the Appendix) was also applied to AIS mass variations. The leading mode, shown in Figure 6.7, is actually showing the same spatial pattern as the

trend map showed in Figure 6.2; its corresponding PC evolution gives area-averaged EWH time series in the Amundsen Sea sector. The 2nd mode shows spatial pattern which covers the whole pole dome, by examining its PC time series, we guess the 2nd EOF/PC is related to ΔC_{20} coefficients, which represent the Earth's oblateness changes. To prove our guess, we apply EOF/PC analysis to monthly mass change fields without GRACE ΔC_{20} replaced by satellite laser ranging (SLR) derived ΔC_{20} coefficients. The 2nd EOF and its corresponding PC are shown as Figure 6.8. We plot the 2nd PCs together with SLR-determined and original GRACE ΔC_{20} respectively. The comparisons are shown as Figure 6.9, we can see these two sets of time series match well with each other, especially for those with original GRACE C_{20} unchanged. We will estimate the contributions of C_{20} to Antarctic ice mass balance estimates later in this chapter.

For the same monthly mass change fields with GRACE C_{20} replaced, we rotate the EOFs towards being independent (i.e. their joint probability distribution is equal to the product of the individual probability distribution) for better interpretation by applying a criterion that maximize the independence among patterns decomposed above. Then the EOF/PC analysis becomes independent component analysis (ICA) [Forootan and Kusche, 2012]. By doing this, the spatial patterns are generally more localized compared with the EOF/PC results. We rotated the leading 5 EOFs and show the results in Figure 6.10. The first and second ICs show the similar patterns as of EOF/PC analysis, which represent the trend map and long-wavelength C_{20} effect. The third IC mainly gives the abnormally high precipitation in EAIS along the coast of Dronning Maud land. The fourth IC shows stripes surrounding the Antarctic continent, which might be related to AOD1B de-aliasing model applied, since stripes noises usually do not have a increasing/decreasing trend. The fifth IC is more complicate, but based on the time series, it represents 161-day alias due to ocean tide model error in the S_2 solar tide [Han et al., 2004; Chen et al., 2008].

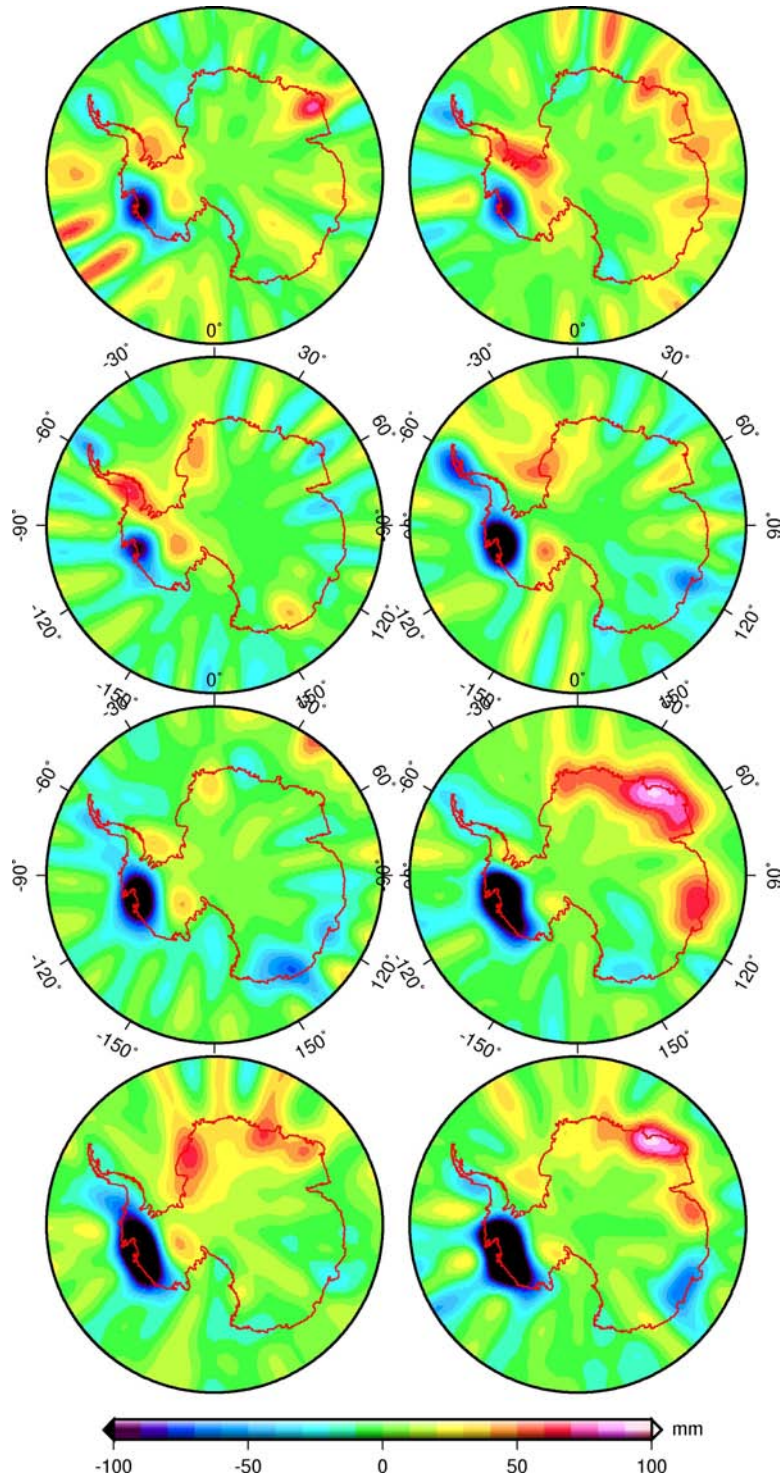


Figure 6.3 Yearly differences (from 2003 to 2011) of yearly-averaged surface mass anomaly (in terms of equivalent water thickness in mm), from CSR data products.

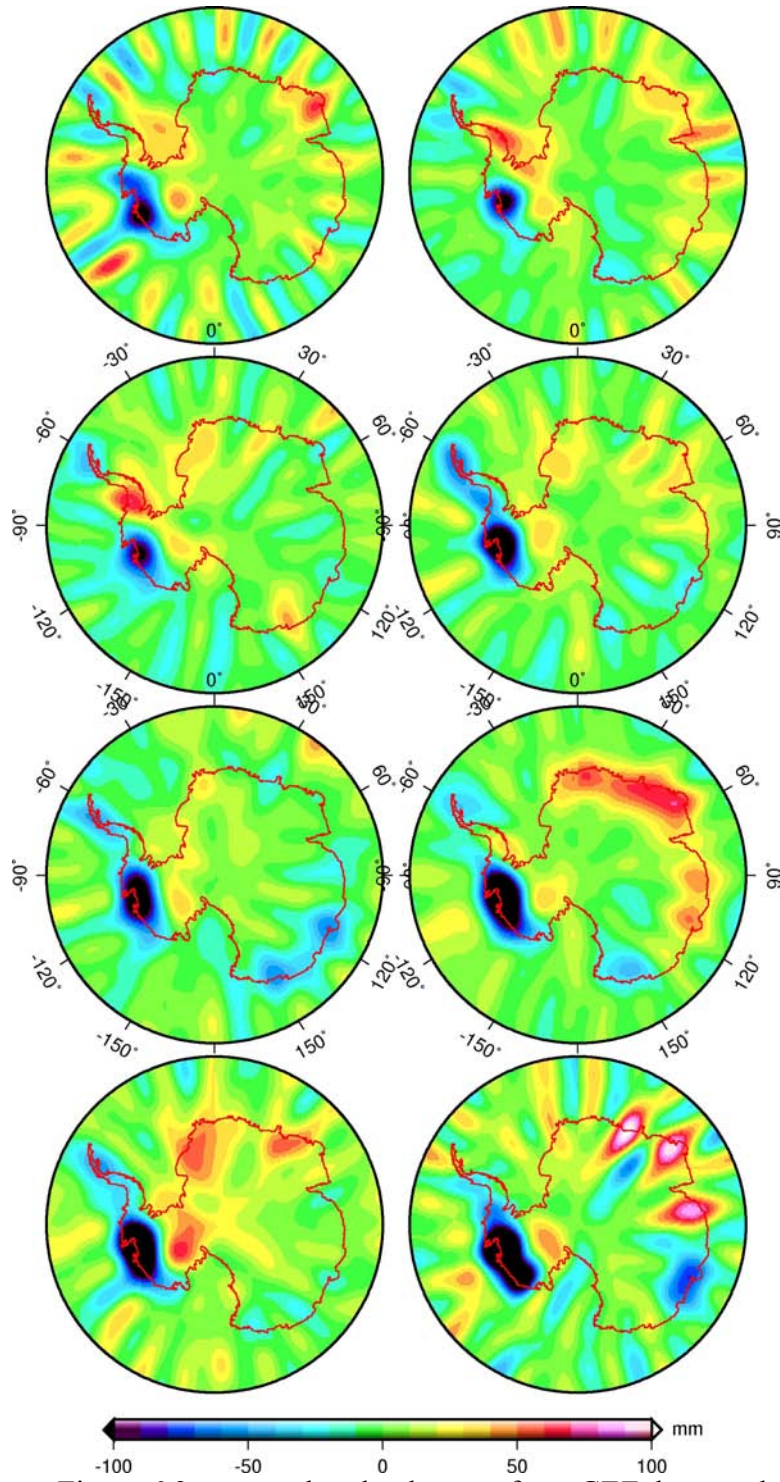


Figure 6.4 Same as Figure 6.3, except that the data are from GFZ data products.

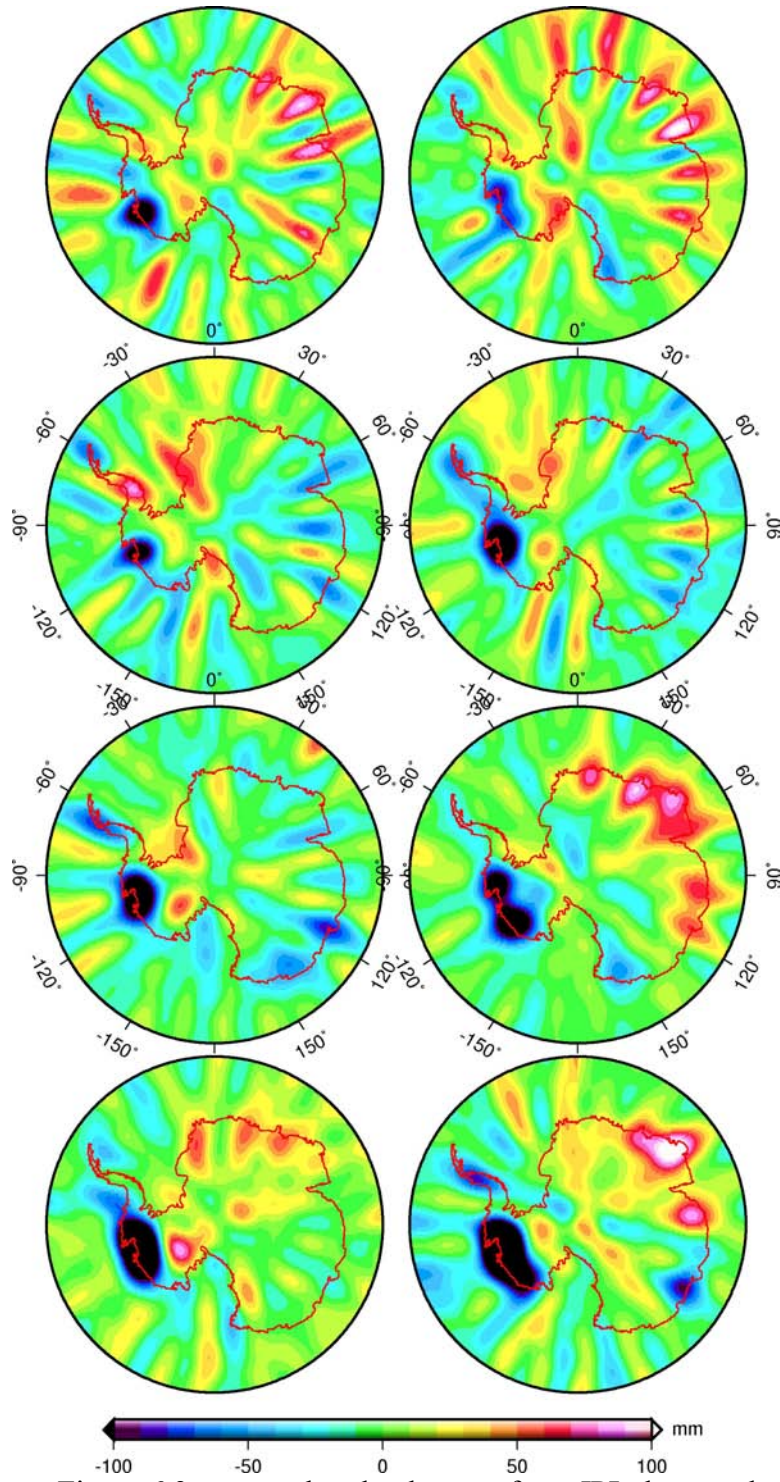


Figure 6.5 Same as Figure 6.3, except that the data are from JPL data products.

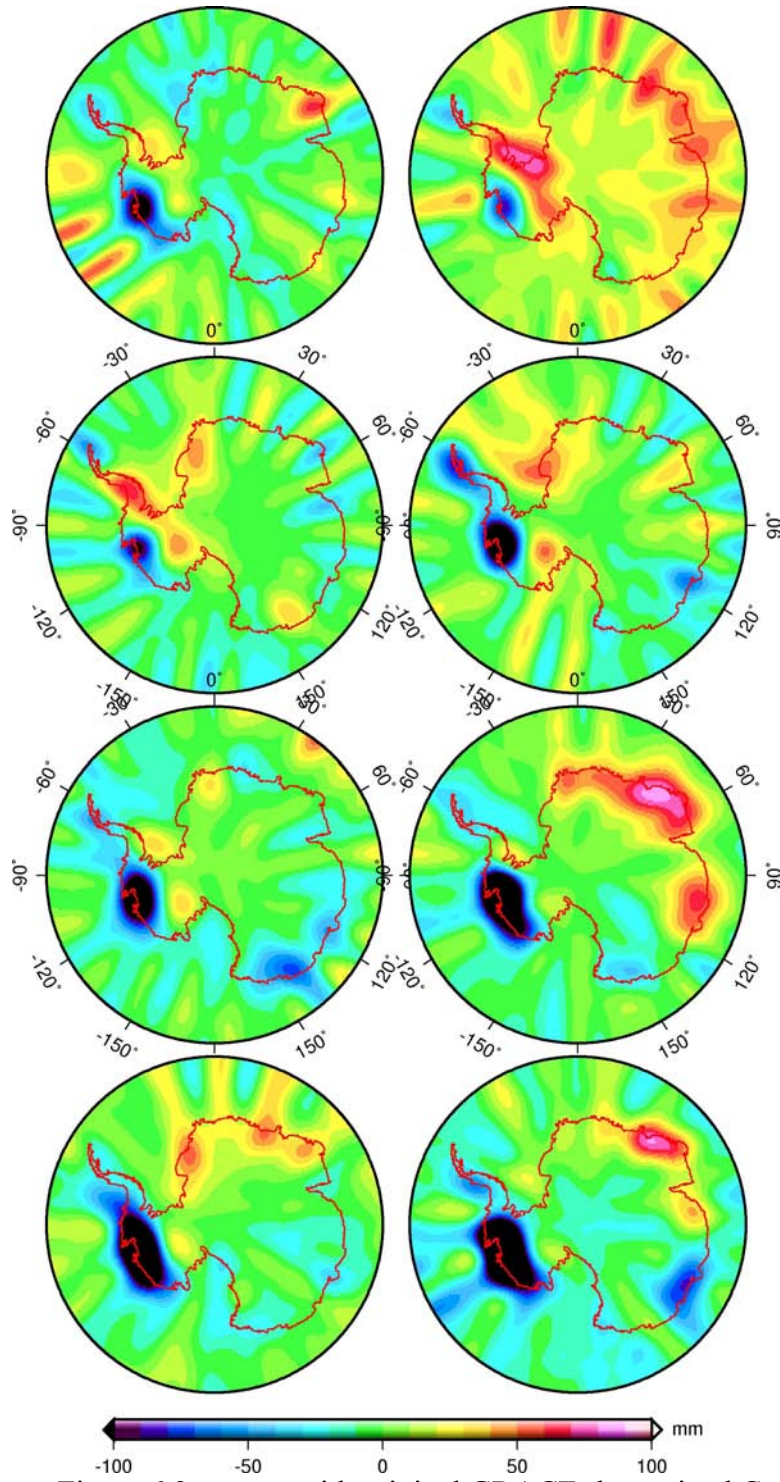


Figure 6.6 Same as Figure 6.3, except with original GRACE-determined C_{20} applied.

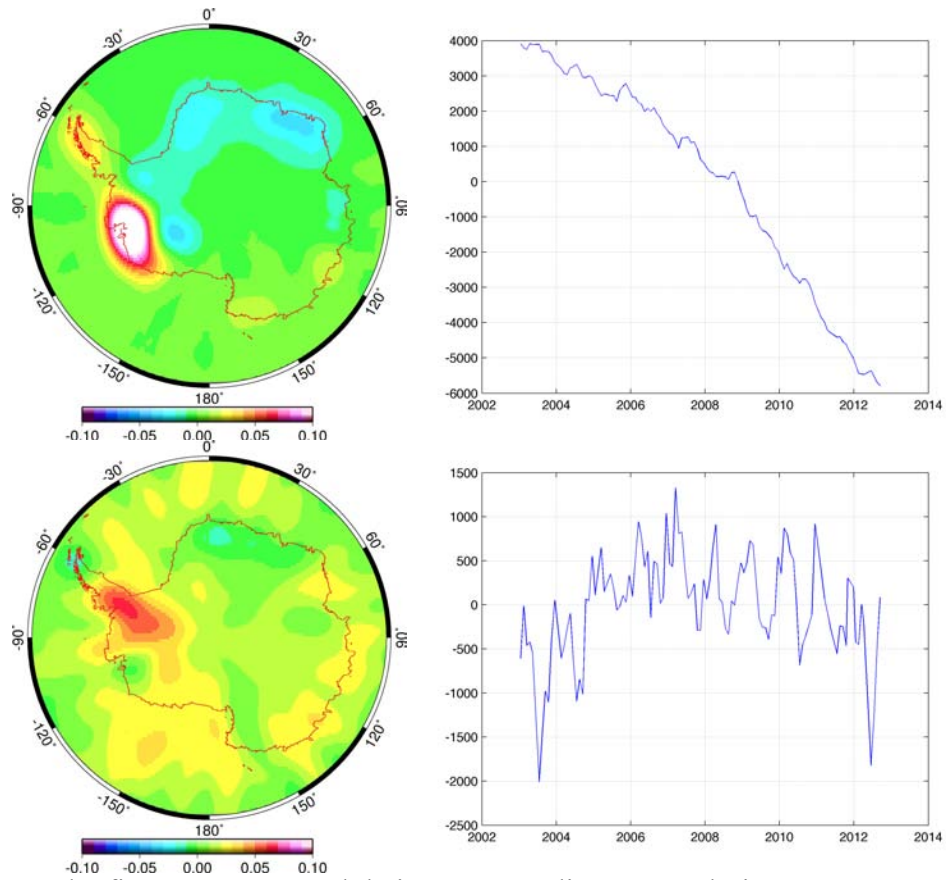


Figure 6.7 The first two EOFs and their corresponding PC evolutions.

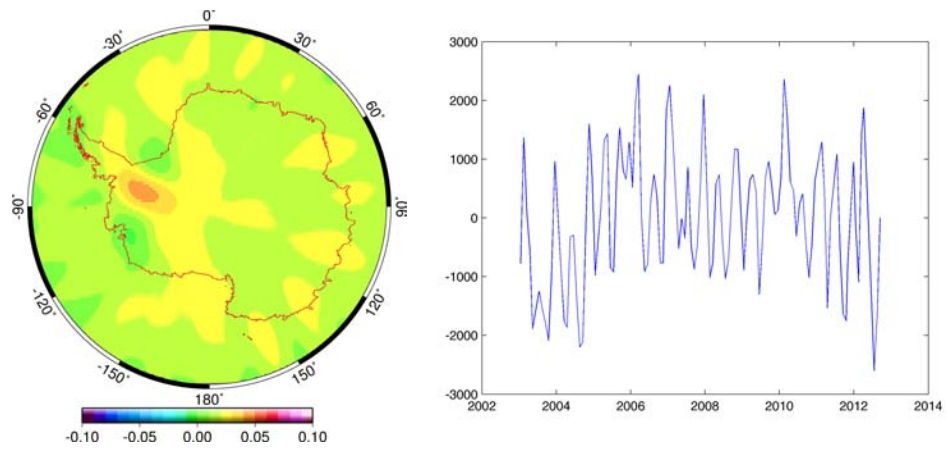


Figure 6.8 Same as the second EOF and its PC in Figure 6.7, except the monthly mass change fields are determined with original GRACE C_{20} terms unchanged.

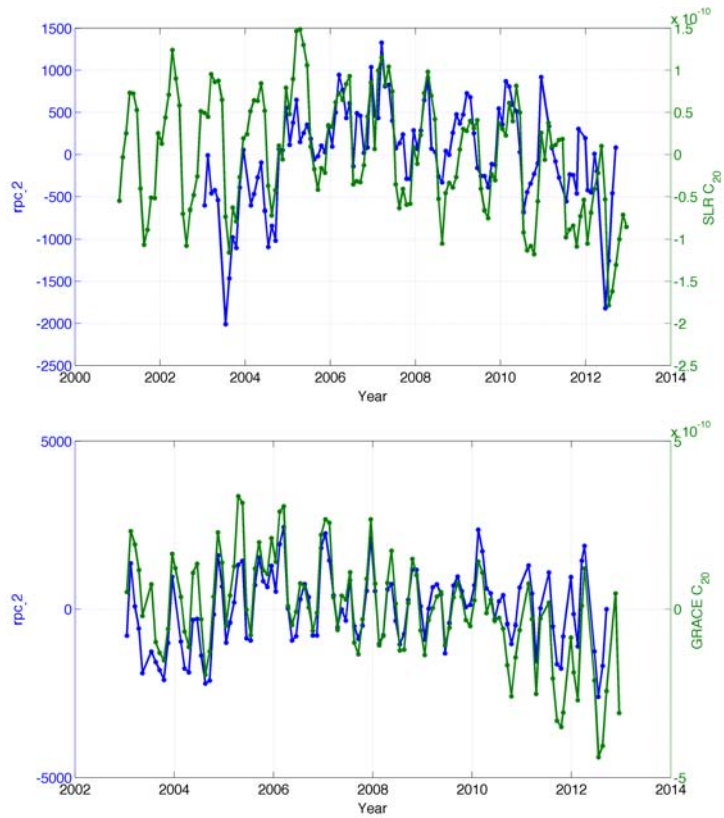
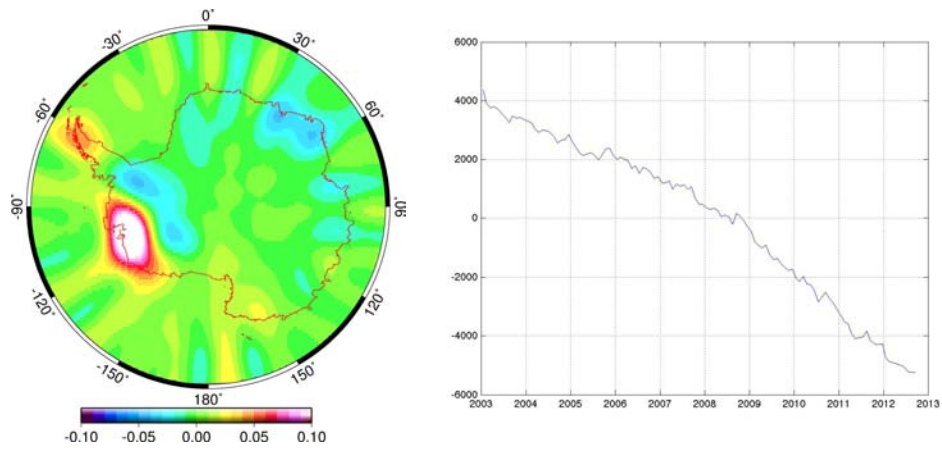
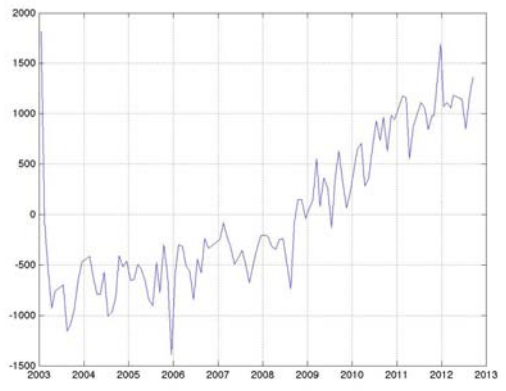
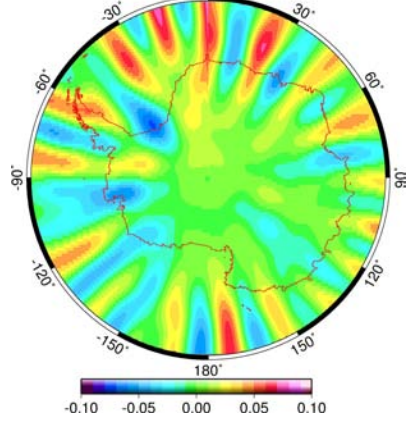
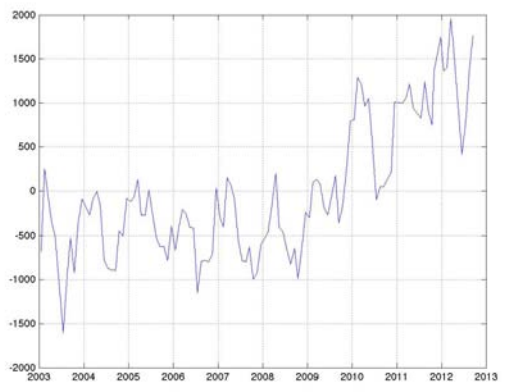
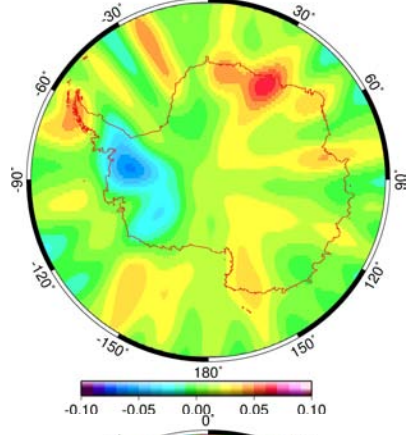
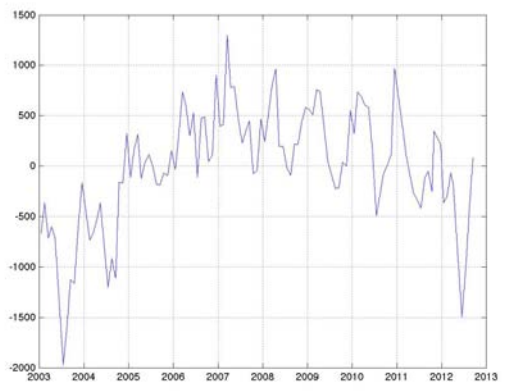
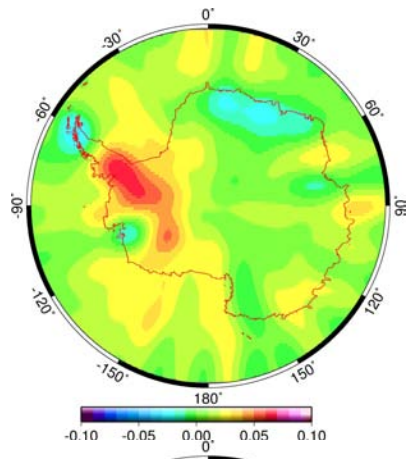


Figure 6.9 Comparisons between the 2nd PC evolutions with corresponding C₂₀ terms used in each monthly gravity fields from CSR.





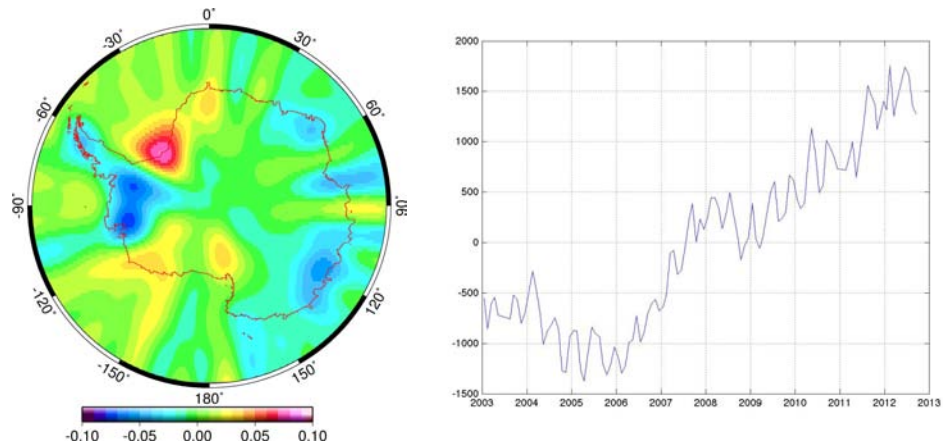


Figure 6.10 The first 5 ICs and their time evolutions.

6.3 Antarctic Surface Mass Balance

As what we applied to Greenland, we compare the P-S term with GRACE observations to gain more confidence interpreting GRACE observed mass changes, before we get the final AIS mass balance estimates. Before doing that comparison, we calculate the yearly differences of annual total precipitation from ERA-interim and NASA's Modern Era Retrospective-analysis for Research and Applications (MERRA, a long-term (1979-present) synthesis that places the current research satellite observations in a climate data context) [Rienecker et al., 2011]. The results are shown as Figure 6.11 and Figure 6.12 respectively. Unlike Tibetan Plateau, where precipitation products differ from each other significantly, these two precipitation data generally agree well with each other. Since there are no evaporation estimates over Antarctic continent in MERRA product, we use P-S form ERA-interim only to compare with GRACE measured mass changes.

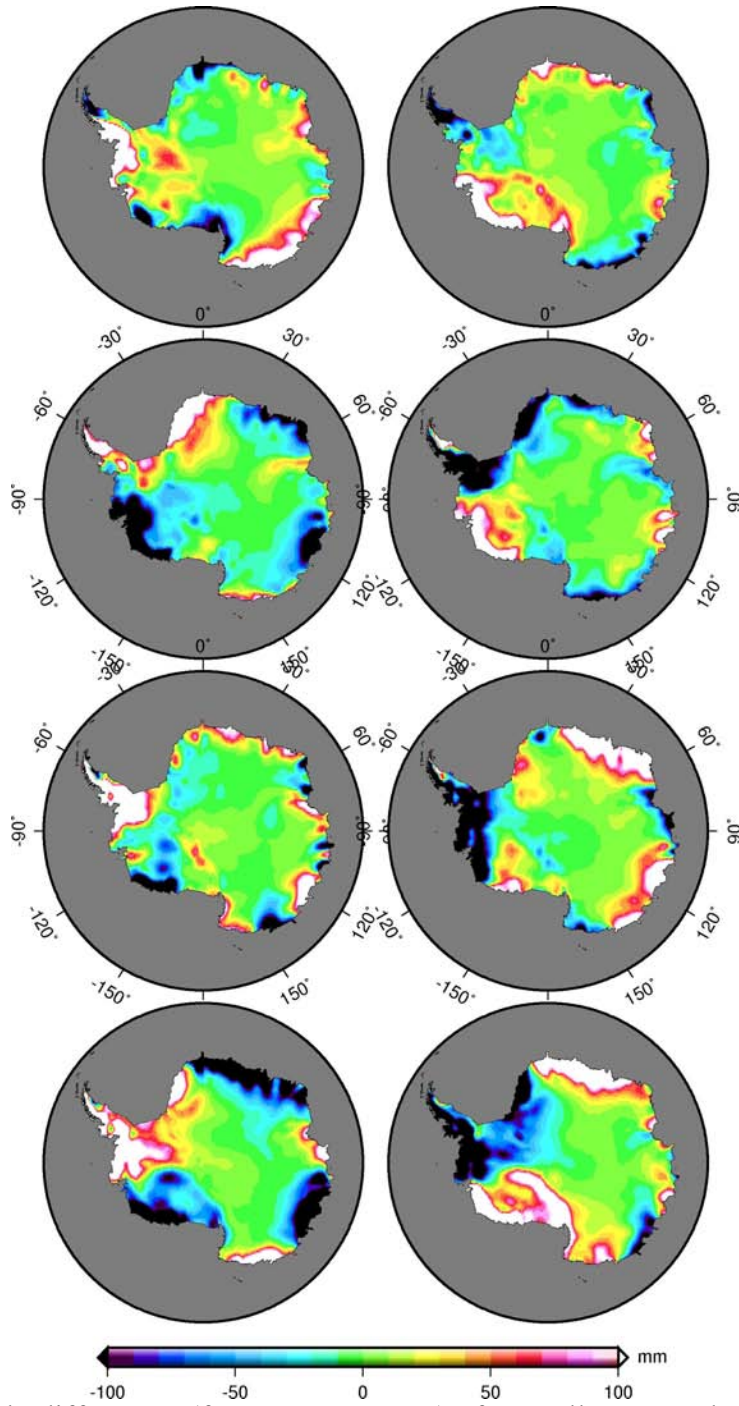


Figure 6.11 Yearly differences (from 2003 to 2011) of annually accumulated precipitation (in terms of equivalent water thickness in mm), from ERA-interim data products.

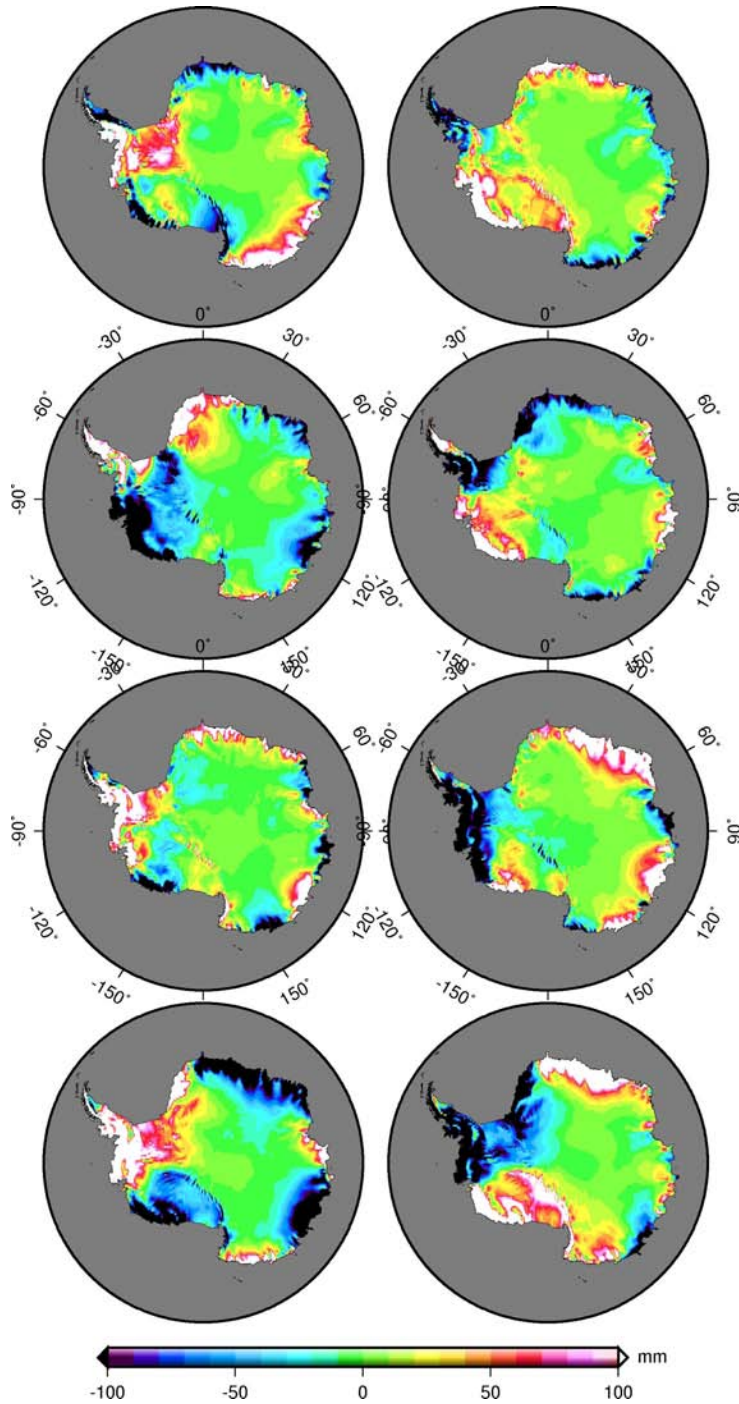
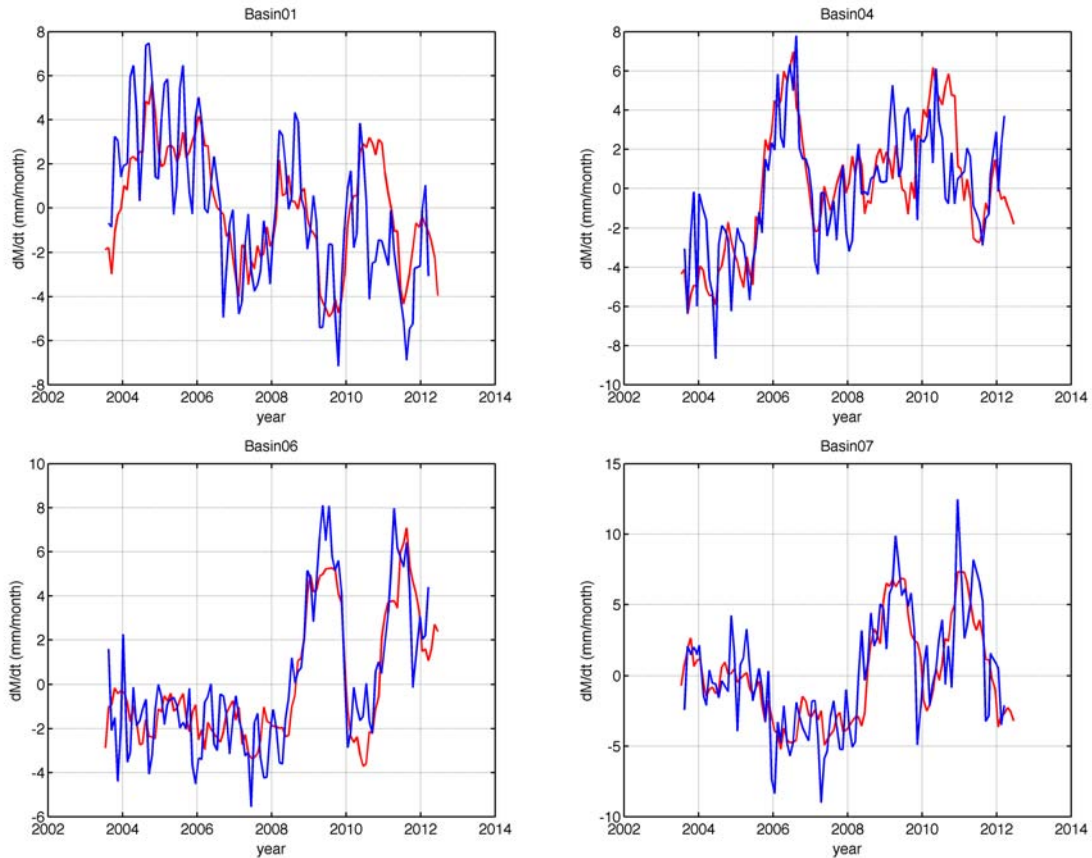


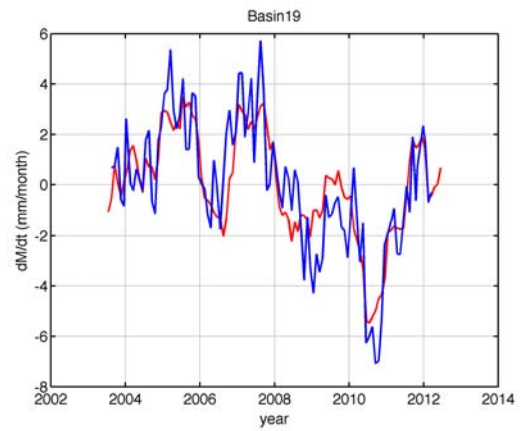
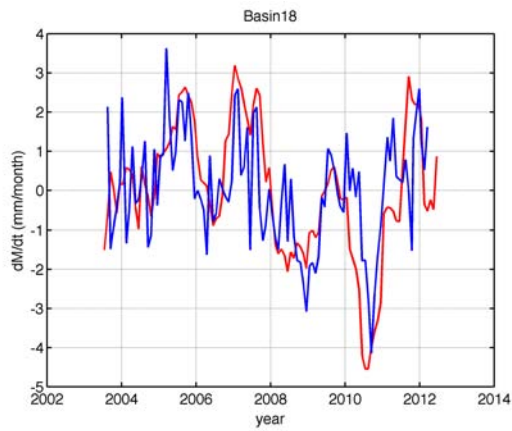
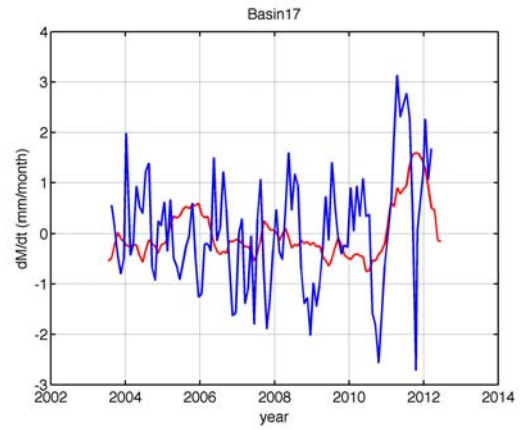
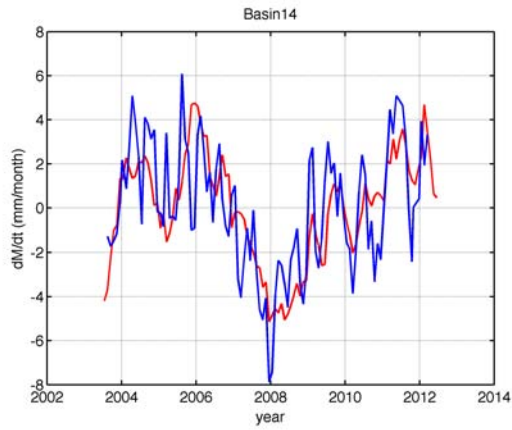
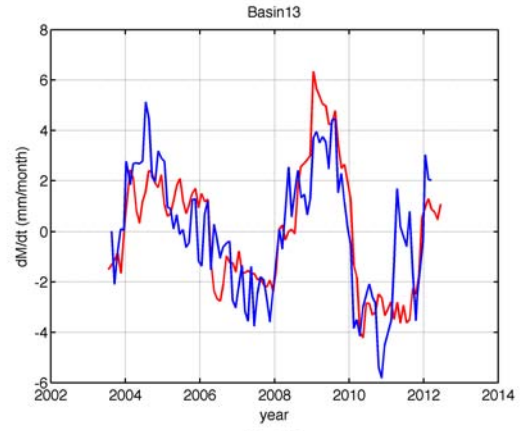
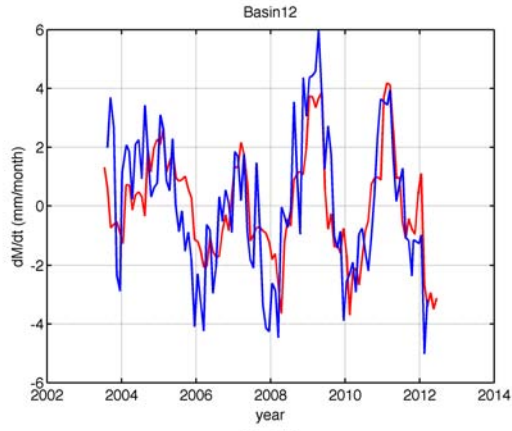
Figure 6.12 Yearly differences (from 2003 to 2011) of annually accumulated precipitation (in terms of equivalent water thickness in mm), from MERRA data products.

We choose several basins to show the comparisons, and we start from Basin 1 with GRACE-observed yearly differences showing mass gain anomalies during the first 3

years. Based on the comparison, we see that ERA-interim derived P-S agree with GRACE observed $dM(t)/dt$, the mass gain anomalies during the first 3 years are real, instead of spurious or relating to GIA signals.

Based on Figure 6.13, we can see ERA-interim derived P-S agree well with GRACE derived $dM(t)/dt$ for most of the basins along the coast of Antarctic continent. For basins located in Antarctic interior where precipitation and evaporation are both very low, we choose Basin 17 to show the comparison, we can see that GRACE observed dS/dt show large variations compared to P-S, the main reason of this is long-wavelength gravity signal, especially C_{20} , cause seasonal/inter-annual mass variations which should not exist in Antarctic interior. For the mass gain signals in EAIS shown in GRACE trend map, P-S and GRACE observed $dM(t)/dt$ reveal that they are actually caused by two different abrupt high precipitation processes which are 2005/2006 high precipitation in Coats Land where Basin 4 locates and high precipitations after 2009 in Dronning Maud Land which contains Basin 6 and 7. For Basin 19, 20 and 21 in WAIS, negative imbalance of P-S since 2007 plays an important role to ice mass loss observed by GRACE.





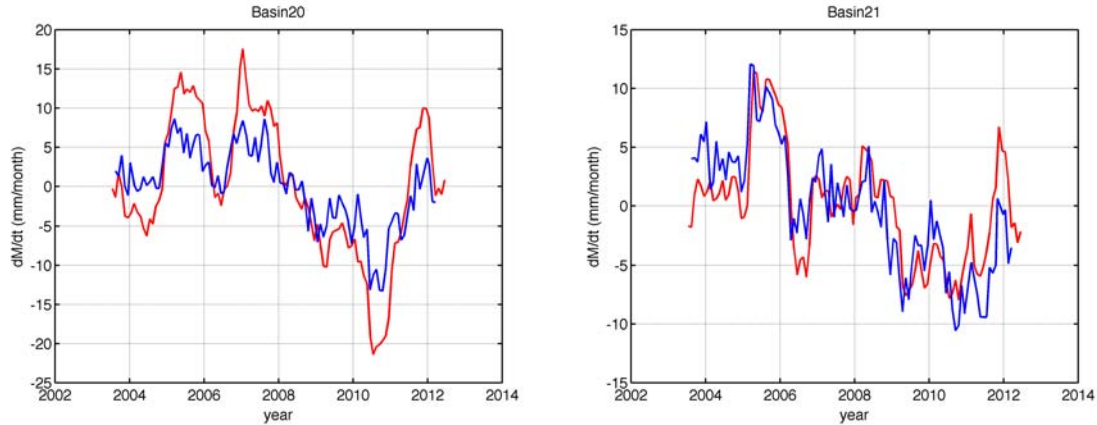


Figure 6.13 Comparison between GRACE derived $dM(t)/dt$ and P-S anomaly from ERA-interim, for selected drainage basins in Antarctic, all the time series are averaged using a 13-month sliding window.

6.4 Uncertainty Assessment

As mentioned in Section 6.1, the uncertainties of GRACE observed mass changes over Antarctic ice sheet are mainly from GIA model error, artifact ice mass loss caused by AOD1B dealiasing model applied; long-wavelength gravity signals which include C_{20} and degree-one coefficients not given by GRACE monthly gravity fields. We will estimate their individual contributions here.

6.4.1 Potential GIA models error

Glacier Isostatic Adjustment (GIA), different from post-glacial rebound (PGR) which refers to the land rebounding back after removal of surface loading by ice sheets, is a more general term that encompasses all of the processes related to the response of the solid Earth to late Quaternary land ice evolution (including changes in Earth rotation and the geopotential) [Shepherd et al., 2012]. Earlier published results before 2012 tended to apply GIA models with mass correction values larger than 100 Gt/yr and advocated ice mass loss acceleration for AIS. Publications since 2012 started to use two new GIA models which give much smaller mass correction, these two GIA models are IJ05_R2 [Ivins et al., 2013] and W12a model [Whitehouse et al., 2012a, 2012b]. Both models are built upon the model IJ05_R0, but they are entirely independent, and the W12a model is based on a glaciological model that simulates ice flow dynamics and the Earth model component is calibrated to a regional (Antarctica) relative sea level data set [Whitehouse et al., 2012; Shepherd et al., 2012]. In this study we apply the W12a regional GIA model, along with a global GIA model Paulson07 [Paulson et al., 2007], these two GIA models are converted into EWH surface mass and shown in Figure 6.14.

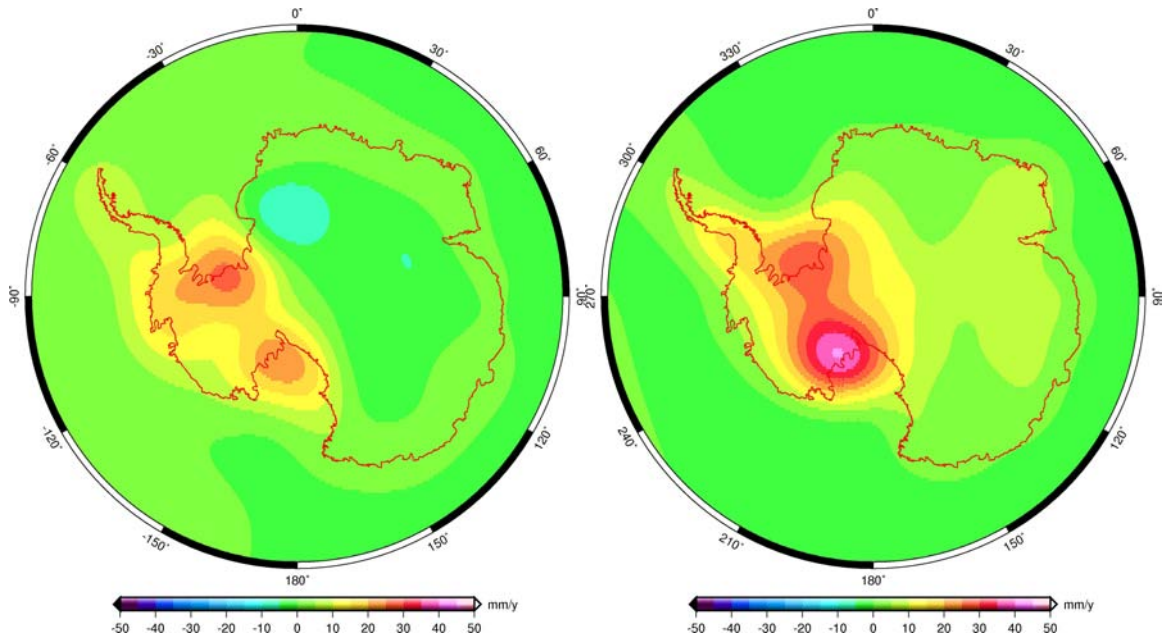


Figure 6.14 Left: the W12a GIA model in mm/yr of EWH; Right: the Paulson07 GIA model.

Large discrepancies among all currently available GIA models reveal the fact that estimating the true uncertainty of GIA correction is actually not achievable, mainly because of lacking of enough in situ measurements to constrain the model outputs. In this study, we use the best estimate of W12a GIA model to correct GRACE observed mass changes for Antarctic ice sheet, and apply the difference between W12a and Paulson07 as the approximate GIA model uncertainty (2σ). As described in Chapter 4.2, we calculate the EWH differences between those two models for each grid cell in the area ($60^{\circ}\text{S}\sim 90^{\circ}\text{S}$, $180^{\circ}\text{W}\sim 180^{\circ}\text{E}$), then calculate their standard deviation, σ_h . $2\sigma_h$, multiplied by the area of Antarctic ice sheet, is used to represent the uncertainty of GIA correction.

6.4.2 AOD1B RL05 de-aliasing ocean model

The OMCT ocean model used for GRACE de-aliasing aims to simulate high-frequency variability of ocean bottom pressure (OBP). Simulated trends in OMCT model are considered less reliable than short-term variability. For Antarctic, we fit the trend term of GAD product and find there are apparently artificial positive trend over and surrounding Antarctic Peninsula, also along the coast of Antarctic continent (Figure 6.15). No matter if the positive OBP trend in the Ross Sea is artificial or true, it does not affect our estimate of AIS mass changes. We will explain the reason later. Ideally, the artificial positive trends in AOD1B ocean product would cause same amount of negative trends in GSM products. We get a negative mass trend of ~ -14 Gt/yr while summing up the whole Antarctic continent, excluding regions covered by ice shelves, along with ~ 300 km buffer regions.

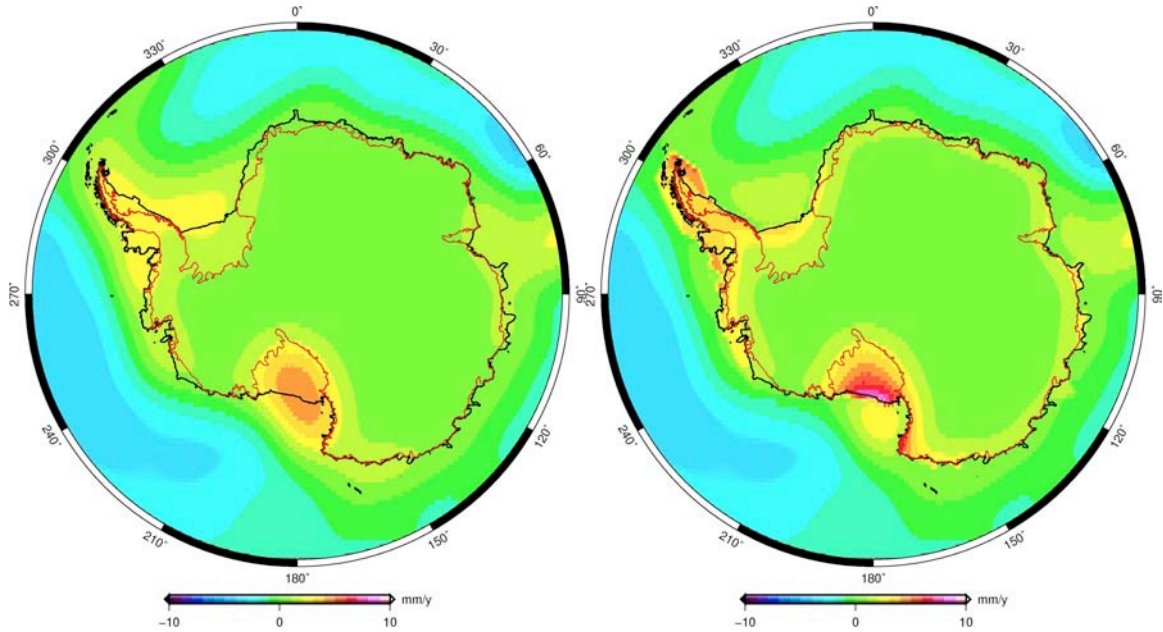


Figure 6.15 Left: trend map (300km Gaussian smoothing) of surface mass changes determined from GAD de-aliasing data product; Right: Same as Left, but with leaked signals recovered.

6.4.3 Long-wavelength gravity signals

The GRACE data are given as sets of spherical harmonic coefficients, while the C_{20} term is poorly determined by GRACE, and degree-1 terms not supplied. As shown in EOF/PC analysis before, C_{20} plays an important role to estimates of AIS mass balance. The Antarctic continent locates at the pole of the Earth, and the fully-normalized associated Legendre function in Eq. 2-16, $\tilde{P}_{20}(\cos\theta) = \sqrt{5}/2(3\cos^2\theta - 1)$, has maximum values at both poles with $\theta = 0^\circ$ and 180° . Hence, any error/uncertainty within C_{20} coefficient would have larger effect on mass estimate over polar region. Figure 6.16 shows the C_{20} time series determined by CSR, GFZ, and JPL respectively. The CSR and JPL C_{20} generally agree with each other, and show much larger magnitude than GFZ C_{20} constrained using SLR observation while GRACE data processing. There is a semi-annual term for GFZ C_{20} , which we cannot explain yet. We did an experiment using just C_{20} and C_{40} (Figure 6.17) to calculate mass changes over the globe, and average over the whole Antarctic continent, then compare the time series with those derived from all 60-degree spherical harmonic coefficients. Figure 6.18 shows the comparison using GRACE C_{20} , SLR C_{20} and GFZ C_{20} . We can see that just 2 SHCs can represent the whole set of coefficients over the Antarctic continent. This actually does not support the assumption and explanation, made by Nerem and Wahr, [2012], which claimed C_{20} coefficient played only a minor role in the GRACE estimates of Antarctic mass variability. Another evidence supporting our conclusion is the difference between CSR and GFZ determined mass changes. The GFZ derived ice mass changes in AIS is less negative than of CSR

since 2011. We compare GFZ determined C_{20} with SLR C_{20} and CSR C_{40} with GFZ C_{40} , both show GFZ determined C_{20} and C_{40} have relatively less fluctuation after 2010 (see Figure 6.19).

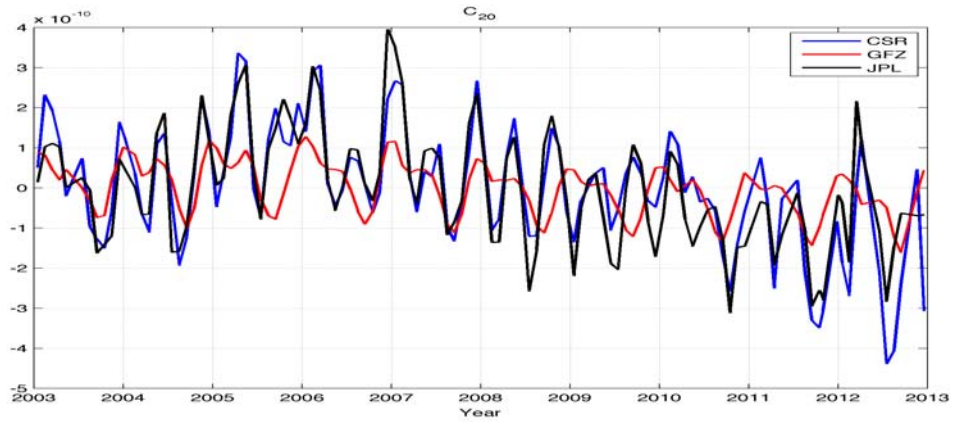


Figure 6.16 C_{20} terms determined by CSR, GFZ and JPL respectively.

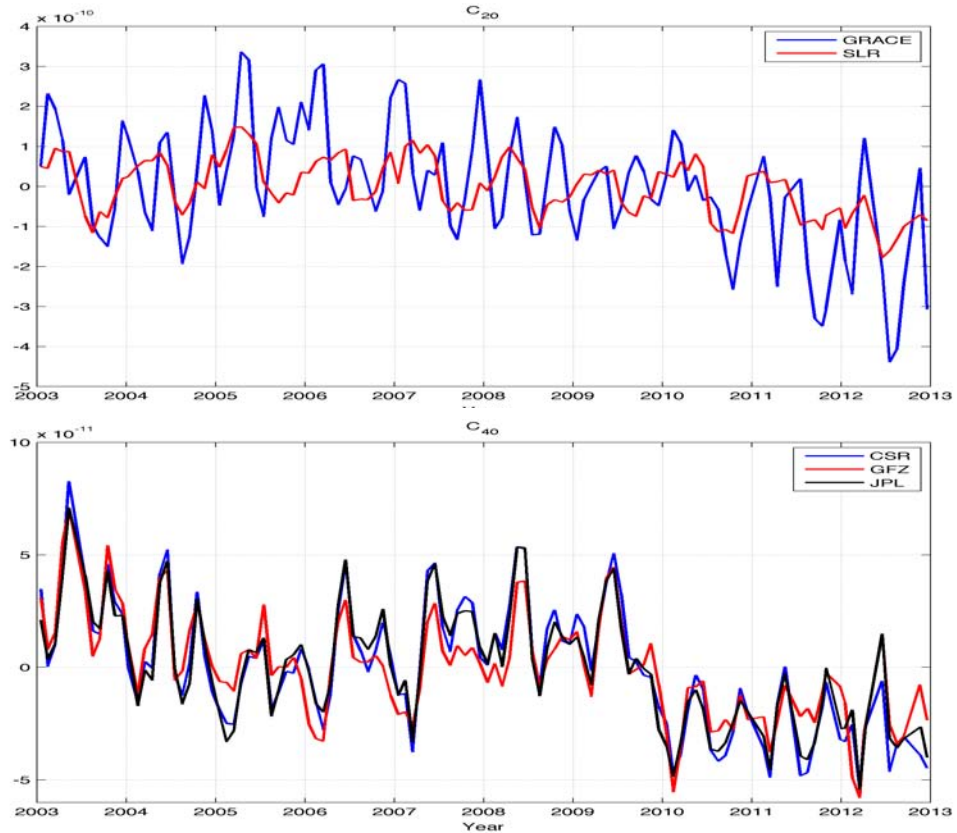


Figure 6.17 TOP: comparison between SLR and GRACE determined C_{20} terms; BOTTOM: C_{40} terms determined by CSR, GFZ and JPL respectively.

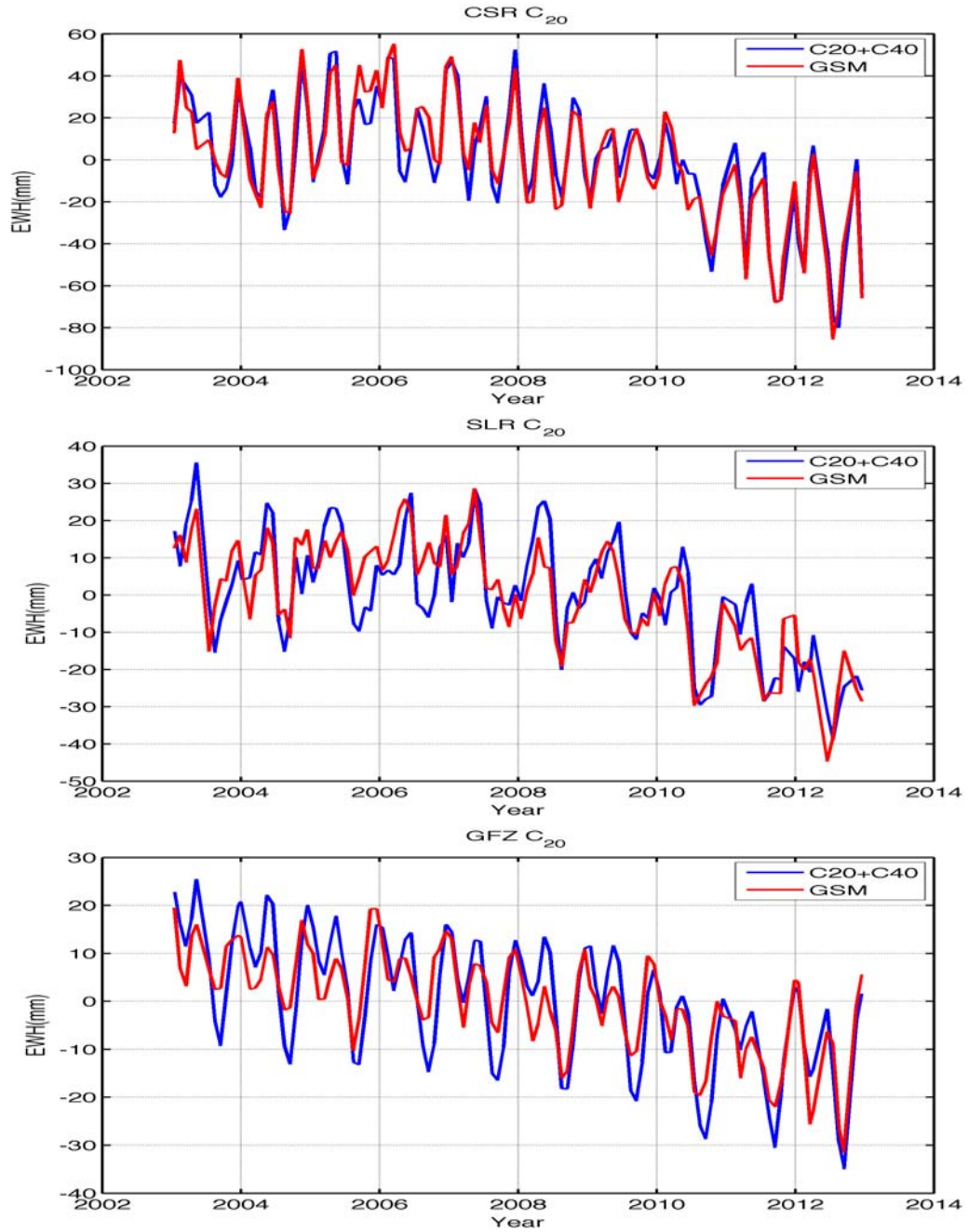


Figure 6.18 Time series of Antarctic-averaged ice mass changes in mm/yr, red lines show mass changes determined using all 60-degree SHCs; blue lines show those determined using C20 and C40 only.

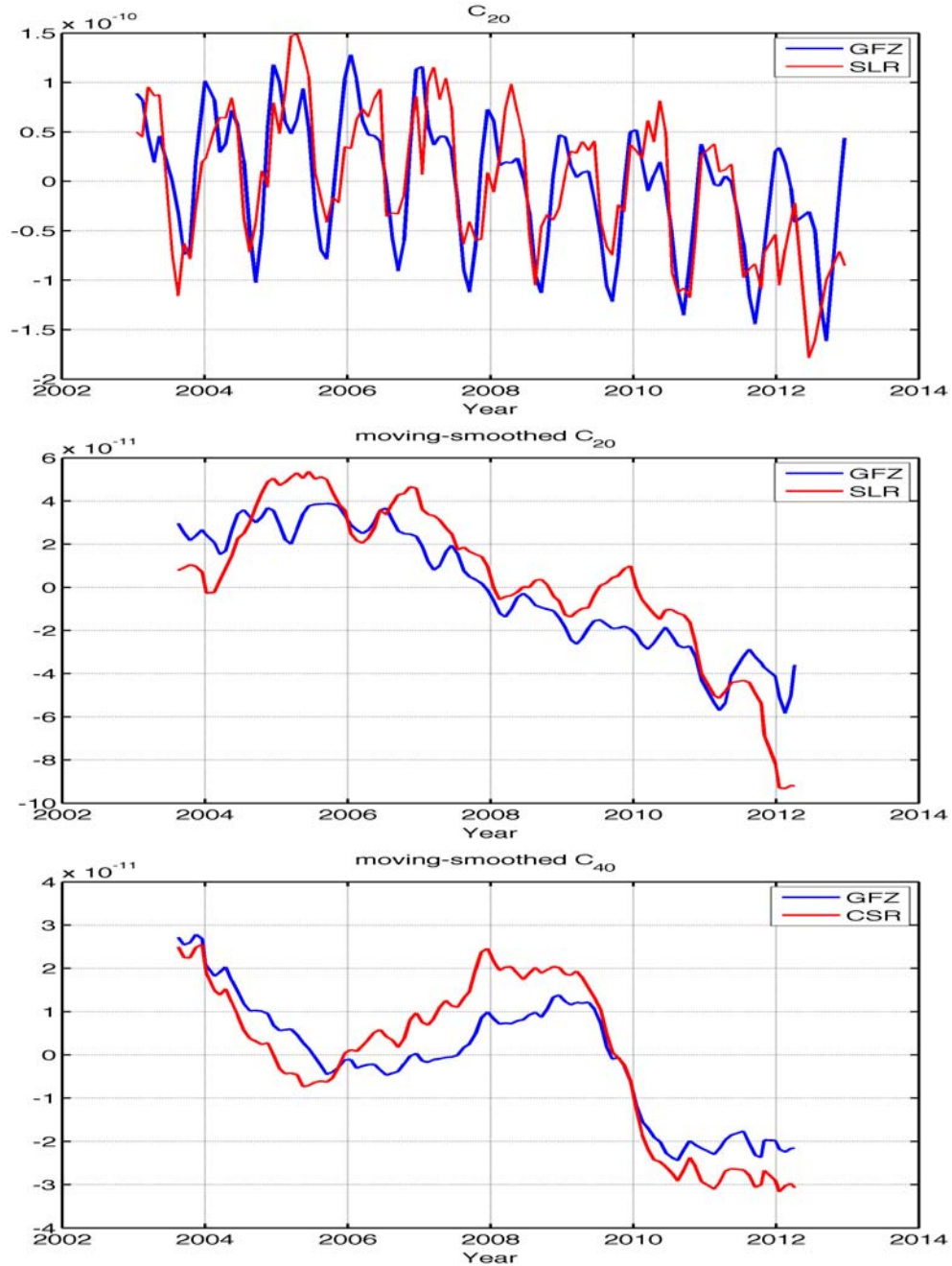


Figure 6.19 TOP: Comparison between GFZ determined C_{20} (blue) with SLR C_{20} (red); MIDDLE: same as TOP, but with averaged using a 13-month sliding window; BOTTOM: comparison between CSR C_{40} and GFZ C_{40} , same moving average applied as MIDDLE.

Degree-1 terms of SHCs are related to geocenter (i.e., center of mass of the Earth) motions. During GRACE data processing, monthly gravity solutions are defined in a reference frame with its origin defined as the center of mass, i.e., the geocenter of

GRACE monthly gravity fields is fixed in the reference frame. Therefore, the degree-1 terms do not exist in GRACE solutions. However, mass transportation and redistribution within the Earth system will cause changes of geocenter [Chen et al., 2013], especially because of accelerated ice loss in Greenland and glaciers in the north hemisphere. It is complicated and difficult to estimate and quantify the influence of geocenter motions to ice mass variability of Antarctic ice sheet. Contemporary studies applied monthly values of degree-terms, computed from ocean model and GRACE SHCs as described by Swenson et al. [2008], to estimate the omitted geocenter contribution [King et al., 2012; Shepherd et al., 2012; Velicogna et al., 2013]. In this study, we do not intent to do the same correction, because 1) the geocenter determination is not independent with respect to GRACE monthly gravity field; 2) it highly relies on ocean model outputs which cannot represent the complicate Earth system; 3) SHCs are sets of delicate mathematical expression in spectral domain, changing just one term usually means other coefficients should change accordingly. Simply adding back long-wavelength geocenter terms to existing GRACE SHCs might introduce more uncertainty, instead of correction. Here, we just estimate how long-term geocenter change rates would contribute mass changes in Antarctic, instead of correcting it in our mass balance estimates.

For Antarctic, because it locates in the pole of the Earth, the Z-component change of geocenter motion contributes the most to mass variability, we use geocenter terms published by GRACE Tellus (<http://grace.jpl.nasa.gov/data/degree1/>), which are calculated based on Swenson et al. [2008], to estimate the geocenter contribution to GRACE-observed AIS ice mass balance. The geocenter rates based on their estimates are (-0.13, 0.067, -0.28mm/yr) during Jan 2003~Dec 2012, and their contributions to AIS ice mass balance estimate is 22 Gt/yr.

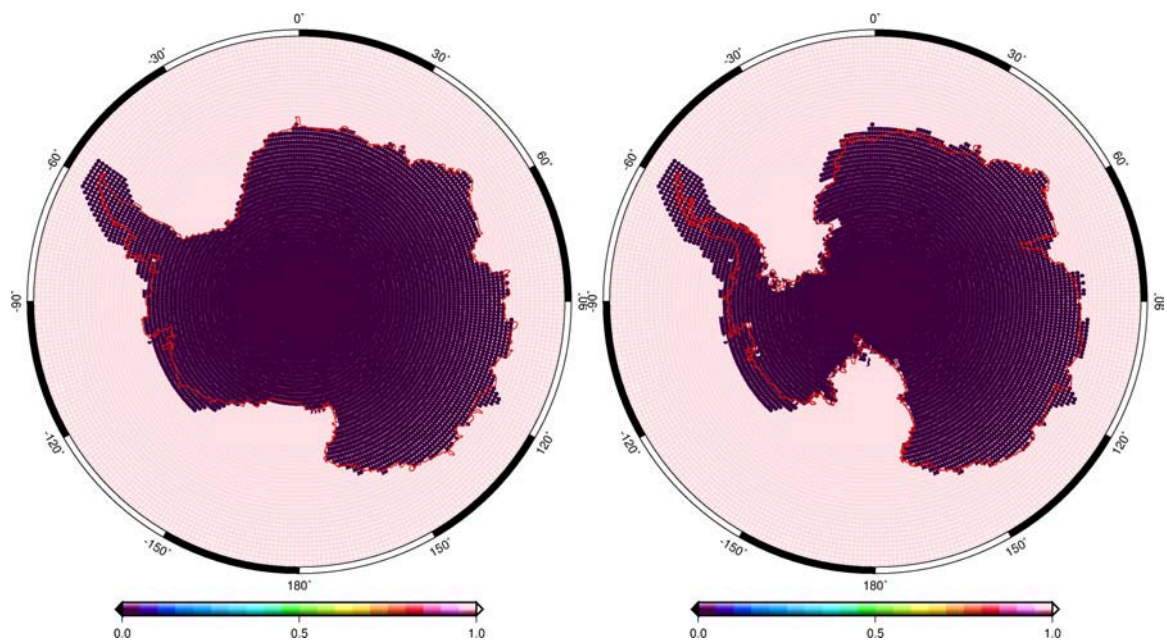


Figure 6.20 Left: mask file used to correct signal leakage caused by Gaussian smoothing; Right: same as Left, but excluding ice shelves.

6.5 Results

To calculate the mass balance of we use the mask file shown in Figure 6.20 to recover leaked signals caused by Gaussian smoothing (see Figure 6.21 for leakage-corrected trend map). The reason we apply the mask file with Filchner-Ronne ice-shelf and Ross ice-shelf included, is that we do not want to recover the mass decreasing trend after GIA corrections under Ross ice-shelf back in land. Contemporary ice mass fluctuations of and on floating ice shelves should be “transparent” to GRACE, since all mass variation is isostatically compensated by the ocean water [Sasgen et al., 2012]. There are mass loss signals under Ross ice-shelf after GIA models applied (see Figure 6.22). Possible causes are: 1) overestimated GIA effects by current GIA models; 2) artificial positive trend over the Ross Sea in GRACE de-aliasing ocean model explained above. This is unlikely to be driven by gravitational attraction caused by onshore ice mass increase on the upper left corner of Ross ice shelf, as explained by King et al. [2012], since the mass decreasing signal is too large to be caused by small onshore mass gain.

Mask file with ice shelves excluded is used to calculate mass balance over AIS for GRACE observed total mass changes and GIA contributions based on two GIA models. Time series of mass balance over the whole AIS, APIS, EAIS and WAIS are calculated and shown in Figure 6.23 ~ 6.26 respectively. Same as for Greenland, for all the times series of each region, JPL estimates agree better with CSR results, compared to those determined by GFZ product. As discussed above, the main reason is our estimates based on both CSR and JPL are using the SLR C_{20} , while original C_{20} and C_{40} are keeping unchanged for GFZ data product. For the whole AIS, the difference between GFZ and CSR/JPL results is about 17 Gt/yr.

We summarize all the estimates of mass balance rates for each region based on three data products, and the contributions from different uncertainty sources, the results are shown in Table 6.1. For W12a GIA model, we calculate its uncertainty based on the lower and upper bounds for the GIA model provided by Whitehouse et al., [2012]. The 2σ uncertainty is ± 28 Gt/yr. For Paulson07 GIA model, we estimate its uncertainty based on the difference between those two models. Finally, we report AIS ice mass changes of -118 ± 30 Gt/yr and -194 ± 86 Gt/yr for W12a and Paulson07 GIA model respectively.

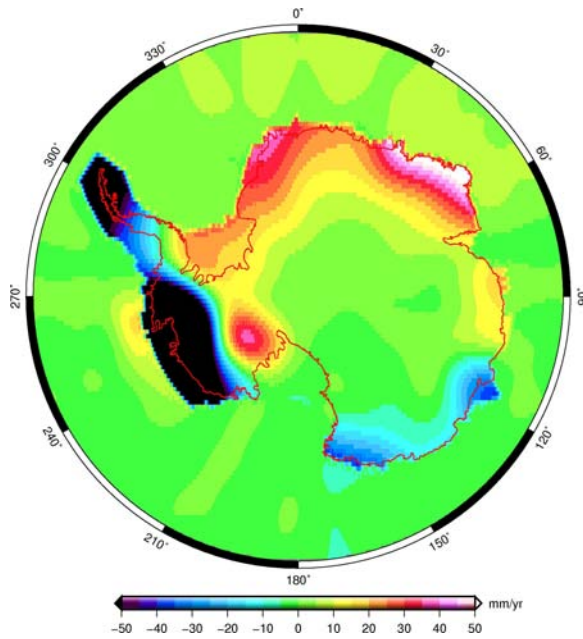


Figure 6.21 Trend map of surface mass changes after recovering leakage caused by Gaussian smoothing, in mm/yr of EWH, determined from CSR GRACE monthly gravity fields for Jan 2003 ~ Dec 2012, no GIA correction applied.

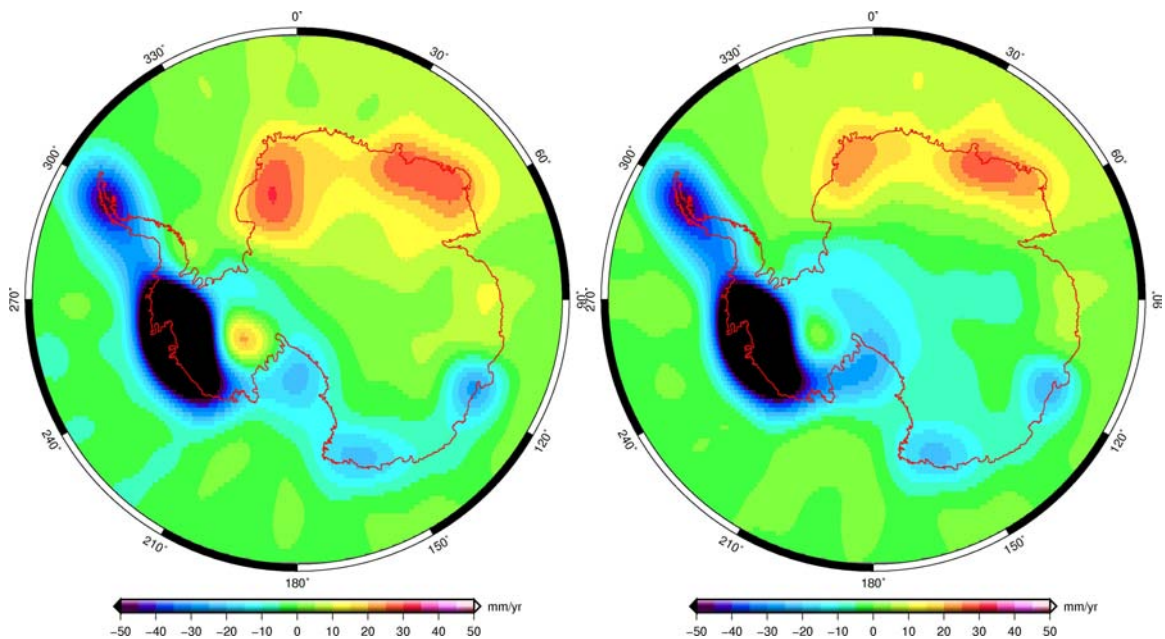


Figure 6.22 Trend map of surface mass changes after 300km Gaussian smoothing, in mm/yr of EWH. Left: W12a GIA model applied; Right: Paulson07 model applied.

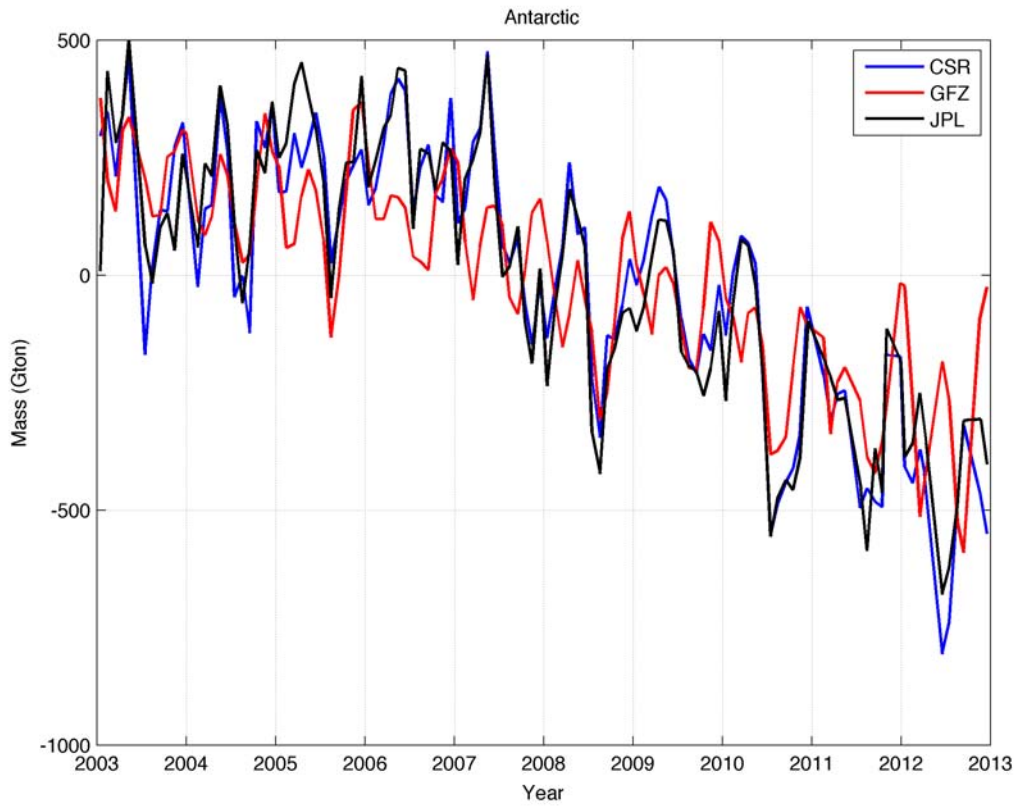


Figure 6.23 Time series of ice mass changes for AIS estimated from 3 GRACE data products for period Jan 2003 ~ Dec 2012, no GIA correction applied.

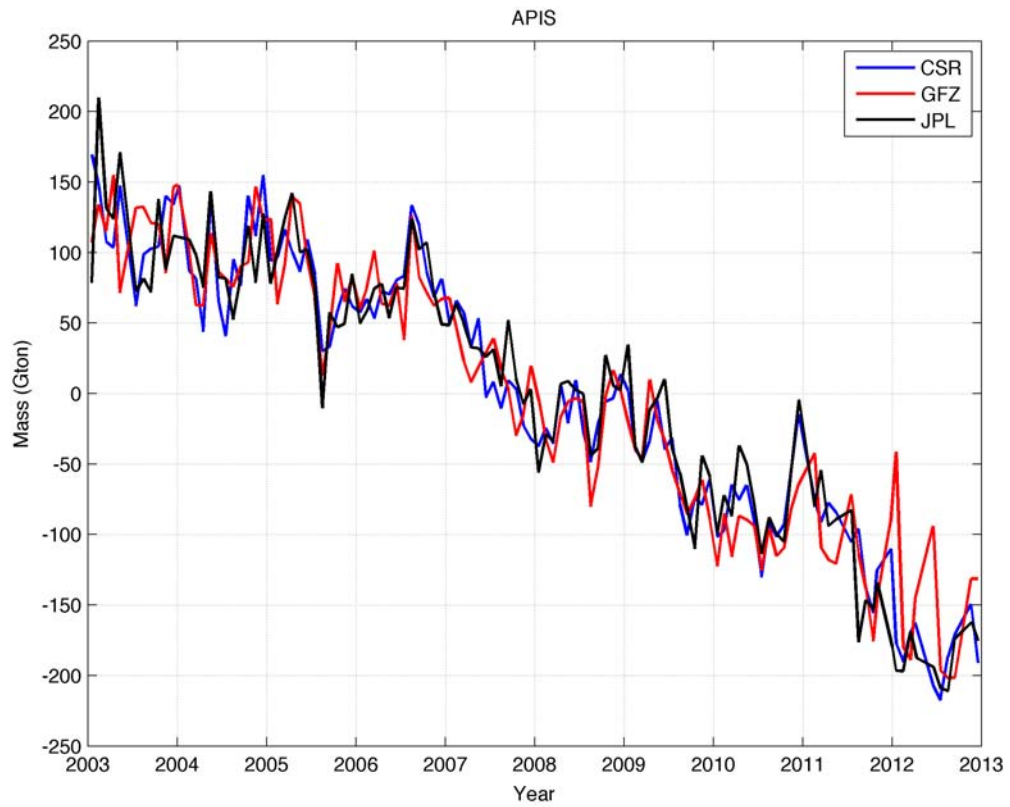


Figure 6.24 Time series of ice mass changes for APIS estimated from 3 GRACE data products for period Jan 2003 ~ Dec 2012, no GIA correction applied.

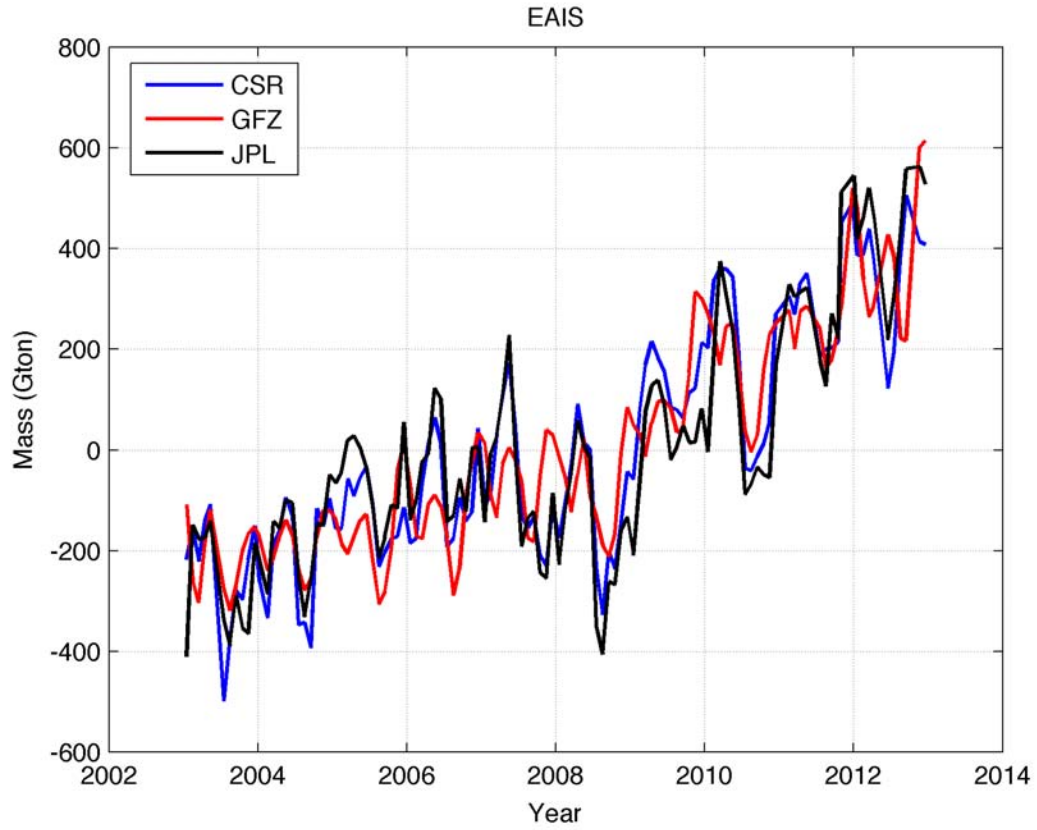


Figure 6.25 Time series of ice mass changes for EAIS estimated from 3 GRACE data products for period Jan 2003 ~ Dec 2012, no GIA correction applied.

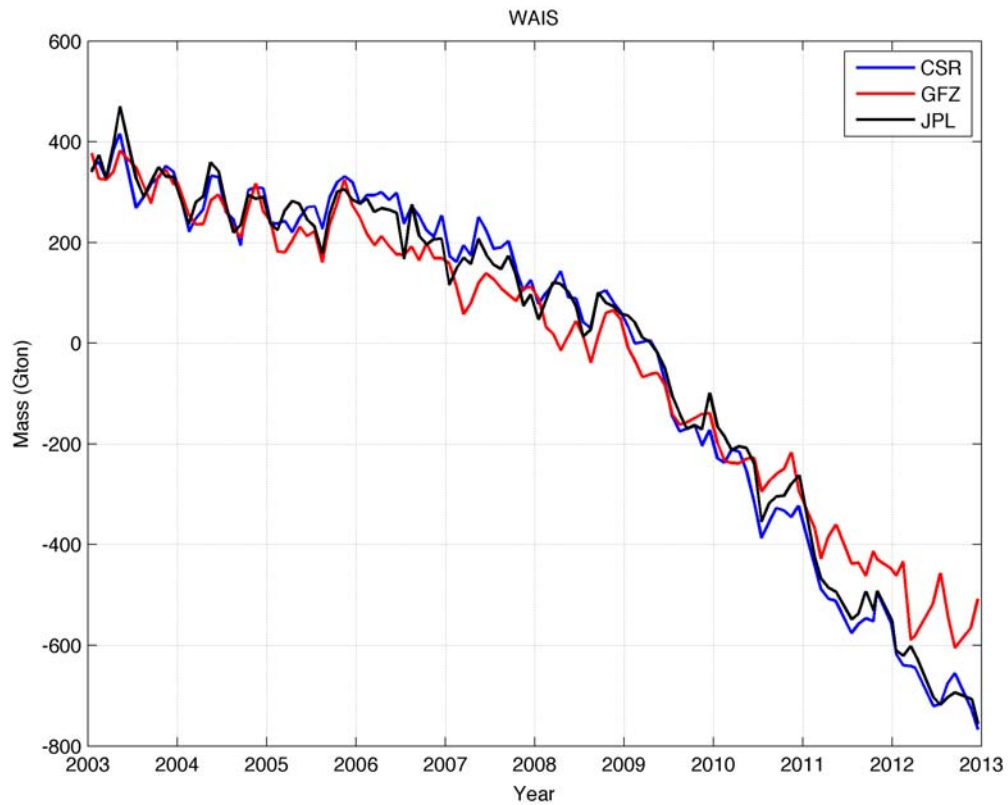


Figure 6.26 Time series of ice mass changes for WAIS estimated from 3 GRACE data products for period Jan 2003 ~ Dec 2012, no GIA correction applied.

	EAIS	WAIS	APIS	AIS
CSR	67	-111	-32	-76±12
GFZ	66	-94	-32	-60
JPL	64	-109	-32	-77
W12a (-)	-0.3	46	10	56±28
Paulson07 (-)	65	56	11	132±85
GAD (+)	8.3	3.2	2.7	14
Geocenter	×	×	×	-22

Table 6.1 Estimated 2003-2012 ice mass change rates (Gt/yr), and contributions from different uncertainty sources, (-) indicates the corresponding contributions should be subtracted from GRACE observed mass changes; while (+) indicates the contributions should be added back. The last column is the sum of the previous columns, and we did not estimate the uncertainties for EAIS, WAIS and APIS. Note that the geocenter contribution was not taken into account for the final estimate of AIS mass balance and its uncertainty.

Chapter 7 Conclusions

Sea levels around the world are rising. Ice mass loss of the polar ice sheets and major mountain glacier systems is one of the main contributors to present-day global mean sea level rise. Estimating and quantifying global ice mass balance is challenging for a number of reasons, e.g., remote locations, lack of *in situ* measurements, and spatial coverage limitation of current remote sensing techniques. GRACE twin-satellite mission has been measuring Earth's time-variable gravity field with unprecedented accuracy and temporal and spatial resolutions. The monthly GRACE measurements of Earth's gravity field can be applied to estimate mass changes of polar ice sheets and major mountain glacier systems. However, large discrepancies exist in previously published estimates of global ice mass balance determined by GRACE. In this study, we estimate GRACE-derived ice mass balance and the associated uncertainty for the world's ice sheets and mountain glacier systems.

In Chapter 3, we uncovered two spurious jumps in the atmosphere and ocean de-aliasing level-1b (AOD1B) data product, which occurred from January to February in both 2006 and 2010. These jumps attain about 7 cm of equivalent water thickness (EWT) change in some regions including the Qinghai-Tibetan Plateau and South America. These spurious jumps, uncovered in both the Release 04 (RL04) and the Release 05 (RL05) AOD1B data, may contaminate the GRACE data products in specific regions of the world. As a consequence, estimates of regional mass changes including glacier mass balance could potentially have errors. We proved that the spurious jump over South America in early 2010 was misinterpreted as real glacier mass changes (-6 ± 12 Gt/yr) in previous study. For Greenland and Antarctic ice sheets. In this study, we correct this effect by adding back the GAC jumps to GRACE monthly gravity fields. For Greenland and Antarctic ice sheets, positive and negative jumps compensate each other, leading to a negligible effect to the mass balance estimates.

In Chapter 4, we estimated GRACE-derived glacier mass balance over High Mountain Asia glacier system by further analyzing possible uncertainties. We applied an enhanced destriping filter to efficiently suppress stripe noises in GRACE monthly solutions. The destriping technique ensured us suppressing high degree noises efficiently with a relatively small smoothing radius. Therefore, we could successfully estimate glacier mass balance for regions that are close to each other but with different glacier responses to climate changes. Besides the corrections applied in previous studies that include hydrologic mass changes, post-LIA and GIA corrections, we also corrected the effect of spurious jumps caused by GRACE de-aliasing product. We further analyzed different precipitation data products and lake level changes observed by satellite altimetry, we found that vastly distributed lakes, wetlands within TBP and their responses as natural reservoirs with respect to abnormal high precipitation in certain years are the main reason which misleads glacier mass balance estimation in previous studies. Our results show that glaciers in HMA retreated at a rate of -31 ± 6 Gt/year from January 2003 to December 2011.

In Chapter 5, we estimated mass changes of the ice sheet and glaciers (January 2003 ~ December 2012) using GRACE over the Greenland and Canadian Arctic, the results of mass changes over Alaska and Patagonia glaciers are also included. For Greenland ice sheet, as the Antarctic ice sheet, most of previous studies employed empirical ways to recover leaked signal caused by Gaussian smoothing for the best estimate of total ice mass changes. In this study, we applied a leakage recovery technique by re-scaling the Gaussian-smoothed mass changes without introducing in any empirical information. Compared to previously (since 2012) published estimates ranging from -199 Gt/yr to 250 Gt/yr, our final estimate of ice mass change rate over Greenland, from Jan 2003 to Dec 2012, is -267 ± 10 Gt/yr, which is equivalent to sea level rise of 0.74 ± 0.03 mm/yr. Obviously accelerated ice mass loss was found occurring in 2010, 2011 and 2012. The mass loss rates are around twice those for years before 2010, and the 2012 yearly resolved mass balance reaches a record-low value -517 Gt based on CSR data product. The contribution of mass loss into ocean from global major mountain glacier systems is considerable, we report mass changes of -171 ± 9 Gt/yr (0.48 ± 0.02 mm/yr sea level rise) from 5 major glacier systems, including HMA glaciers discussed in Chapter 4. Compared to the result of Jacob et al. [2012], -151 ± 30 Gt/yr, the main difference is from their underestimated HMA glacier mass balance, -4 ± 20 Gt/yr.

In earlier (since 2012) published studies, large discrepancies exist for the estimates of GRACE-derived mass balance over Antarctic ice sheet, which range from -180 Gt/yr to -69 Gt/yr. In Chapter 6, we analyzed uncertainties in GRACE estimates of ice mass balance over Antarctic ice sheet, and estimate mass balance of AIS for period from Jan 2003 to Dec 2012. We found long-wavelength gravity signals (C_{20} and C_{40}) in GRACE determined monthly gravity fields are another source of large uncertainties after GIA models. We fit the trend term of GRACE de-aliasing product and found there were apparently artificial positive trend over and surrounding Antarctic Peninsula, also along the coast of Antarctic continent. This effect would cause an artificial trend of ~ -14 Gt/yr in GRACE-derived mass balance estimate over the Antarctic continent. Our final estimates of ice mass balance are based on two different GIA models, we report AIS ice mass changes of -118 ± 30 Gt/yr (0.33 ± 0.08 mm/yr sea level rise) and -194 ± 86 Gt/yr (0.54 ± 0.24 mm/yr sea level rise) for W12a and Paulson07 GIA model respectively.

The contribution of global ice mass balance to global mean sea level rise is 1.55 ± 0.1 mm/yr from January 2003 to December 2012 based on our best estimates using GRACE monthly gravity fields. It is hard to tell what improvements our solution is, by simply comparing our result to those of two most recent studies, -1.48 ± 0.26 mm/yr [Jacob et al., 2012] and 1.80 ± 0.26 mm/yr [Chen et al., 2013]. For each glacier system, we reduced uncertainties by taking into account of corrections not applied in previous studies. Moreover, our GRACE data processing techniques ensure the good agreement between GRACE observations and model-derived surface mass balance for small basins, while solutions of those two studies have their limits to represent mass changes for most of drainage basins of Greenland and Antarctic ice sheets. For the ‘mascon’ solution in Jacob et al. 2012, only grouped ‘mascons’ (average of large area) have actual meanings, single ‘mascon’ estimate is dominated by stripe noises only. Chen et al. [2013], on the other

hand, applied a destriping filter and 500 km Gaussian smoothing. The destriping filter would suppress stripes noises efficiently, but also distort signals over near-polar regions. Moreover, their empirical forward modeling approach, which is used to estimate total mass changes of ice sheet system, can only be applied to the trend estimate. One cannot get the time evolution progress of ice mass changes for the ice sheets, or for certain drainage basin.

In this study, we reduced uncertainties in the estimates of GRACE-derived global mass balance by taking into account of corrections not applied in previous studies, and by applying appropriate error propagation. It is still challenging to improve the estimates of GRACE global ice mass balance, and to reduce the contamination of various uncertainties. Further studies are still necessary to investigate GRACE-determined global ice mass balance with the assistance of other available data sets, including *in situ* data and measurements from other remote sensing techniques.

Bibliography

- A, G., J. Wahr, and S.J. Zhong (2013), Computations of the viscoelastic response of a 3-D compressible Earth to surface loading: an application to glacial isostatic adjustment in Antarctica and Canada, *Geophys. J. Int.*, 192, 557-572.
- Adler, R. F., et al. (2003), The Version-2 Global Precipitation Climatology Project (GPCP) Monthly Precipitation Analysis (1979, ÅiPresent), *Journal of Hydrometeorology*, 4(6), 1147-1167.
- Albertella, A., R. Savcenko, W. Bosch, R. Rummel (2008), Dynamic Ocean Topography: The Geodetic Approach, *IAPG/FESG No. 27*.
- Baur, O., M. Kuhn, and W. E. Featherstone (2009), GRACE-derived ice-mass variations over Greenland by accounting for leakage effects, *Journal of Geophysical Research-Solid Earth*, 114.
- Bindoff, N. L., et al. (2007), Observations: oceanic climate change and sea level. *Rep. 0521880092*, United Kingdom and New York, NY, USA.
- Boening, C., M. Lebrock, F. Landerer, and G. Stephens (2012), Snowfall-driven mass change on the East Antarctic ice sheet, *Geophysical Research Letters*, 39(21), L21501.
- Bolch, T., et al. (2012), The State and Fate of Himalayan Glaciers, *Science*, 336(6079), 310-314.
- Box J.E., J. Cappelen, D. Decker, X. Fettweis, T. Mote, M. Tedesco and R. van de Wal (2010), Greenland in *Arctic Report Card 2010*, <http://www.arctic.noaa.gov/reportcard>. Cazenave, A., K. Dominh, S. Guinehut, E. Berthier, W. Llovel, G. Ramillien, M. Ablain, and G. Larnicol (2009), Sea level budget over 2003-2008: A reevaluation from GRACE space gravimetry, satellite altimetry and Argo, *Global Planet Change*, 65(1-2), 83-88.
- Cazenave, A., and W. Llovel (2010), Contemporary Sea Level Rise, *Annu Rev Mar Sci*, 2, 145-173.
- Chambers, D. P., J. Wahr, and R. S. Nerem (2004), Preliminary observations of global ocean mass variations with GRACE, *Geophys Res Lett*, 31(13).
- Chambers, D. P. (2006), Evaluation of new GRACE time-variable gravity data over the ocean, *Geophysical Research Letters*, 33(17).
- Chao, B. F., and R. S. Gross (1987), Changes in the Earth's Rotation and Low-Degree Gravitational-Field Induced by Earthquakes, *Geophys J Roy Astr S*, 91(3), 569-596.
- Chao, B. F., W. P. Oconnor, A. T. C. Chang, D. K. Hall, and J. L. Foster (1987), Snow Load Effect on the Earth's Rotation and Gravitational-Field, 1979-1985, *J Geophys Res-Solid*, 92(B9), 9415-9422.

- Chao, B. F. (2005), On inversion for mass distribution from global (time-variable) gravity field, *Journal of Geodynamics*, 39(3), 223-230.
- Chen, J. L., C. R. Wilson, D. D. Blankenship, and B. D. Tapley (2006), Antarctic mass rates from GRACE, *Geophys Res Lett*, 33(11).
- Chen, J. L., C. R. Wilson, B. D. Tapley, and S. Grand (2007), GRACE detects coseismic and postseismic deformation from the Sumatra-Andaman earthquake, *Geophysical Research Letters*, 34(13).
- Chen, J. L., C. R. Wilson, D. Blankenship, and B. D. Tapley (2009), Accelerated Antarctic ice loss from satellite gravity measurements, *Nature Geosci*, 2(12), 859-862.
- Chen, J. L., C. R. Wilson, and B. D. Tapley (2013), Contribution of ice sheet and mountain glacier melt to recent sea level rise, *Nature Geosci*, 6(7), 549-552.
- Cheng, M. K., and B. D. Tapley (2004), Variations in the Earth's oblateness during the past 28 years, *J Geophys Res-Sol Ea*, 109(B9).
- Cheng, M. K., B. D. Tapley, and J. C. Ries (2013), Deceleration in the Earth's oblateness, *Journal of Geophysical Research: Solid Earth*, 118(2), 740-747.
- Church, J.A. et al. (2001), Intergovernmental Panel on Climate Change Third Assessment Report "Climate Change 2001".
- Church, J. A., and N. J. White (2006), A 20th century acceleration in global sea-level rise, *Geophysical Research Letters*, 33(1), L01602.
- Church, J. A., and N. J. White (2011), Sea-Level Rise from the Late 19th to the Early 21st Century, *Surv Geophys*, 32(4-5), 585-602.
- Clark, J. A., W. E. Farrell, and W. R. Peltier (1978), Global Changes in Post-Glacial Sea-Level - Numerical-Calculation, *Quaternary Res*, 9(3), 265-287.
- Clark, P. U., A. S. Dyke, J. D. Shakun, A. E. Carlson, J. Clark, B. Wohlfarth, J. X. Mitrovica, S. W. Hostetler, and A. M. McCabe (2009), The Last Glacial Maximum, *Science*, 325(5941), 710-714.
- Cogley, J.G. et al. (2011), Glossary of glacier mass balance and related terms, IHP-VII Technical Documents in Hydrology No. 86, IACS Contribution No. 2, UNESCO-IHP, Paris.
- Cook, A. J., A. J. Fox, D. G. Vaughan, and J. G. Ferrigno (2005), Retreating Glacier Fronts on the Antarctic Peninsula over the Past Half-Century, *Science*, 308(5721), 541-544.
- Cox, C. M., and B. F. Chao (2002), Detection of a large-scale mass redistribution in the terrestrial system since 1998, *Science*, 297(5582), 831-833.
- Crétaux, J. F. et al. (2011), SOLS: A lake database to monitor in the Near Real Time water level and storage variations from remote sensing data, *Advances in Space Research*, 47(9), 1497-1507.

- Davis, C. H., Y. Li, J. R. McConnell, M. M. Frey, and E. Hanna (2005), Snowfall-Driven Growth in East Antarctic Ice Sheet Mitigates Recent Sea-Level Rise, *Science*, 308(5730), 1898-1901.
- Davis, J. L., M. E. Tamisiea, P. Elosegui, J. X. Mitrovica, and E. M. Hill (2008), A statistical filtering approach for Gravity Recovery and Climate Experiment (GRACE) gravity data, *Journal of Geophysical Research-Solid Earth*, 113(B4).
- De Angelis, H. N., and P. Skvarca (2003), Glacier Surge After Ice Shelf Collapse, *Science*, 299(5612), 1560-1562.
- Deakin, R. E., and D. G. Kildea (1999), A note on standard deviation and RMS, *The Australian Surveyor*, 44(1).
- Dickey, J. O., S. L. Marcus, O. de Viron, and I. Fukumori (2002), Recent Earth oblateness variations: Unraveling climate and postglacial rebound effects, *Science*, 298(5600), 1975-1977.
- Douglas, B. C., and W. R. Peltier (2002), The puzzle of global sea-level rise, *Phys Today*, 55(3), 35-40.
- Döll, P., F. Kaspar, and B. Lehner (2003), A global hydrological model for deriving water availability indicators: model tuning and validation, *Journal of Hydrology*, 270(1,Äi2), 105-134.
- Duan, X. J., J. Y. Guo, C. K. Shum, and W. van der Wal (2009), On the postprocessing removal of correlated errors in GRACE temporal gravity field solutions, *J Geodesy*, 83(11), 1095-1106.
- Duan, J., C. K. Shum, J. Guo, and Z. Huang (2012), Uncovered spurious jumps in the GRACE atmospheric de-aliasing data: potential contamination of GRACE observed mass change, *Geophysical Journal International*, 191(1), 83-87.
- Dziewonski, A. M., and D. L. Anderson (1981), Preliminary reference Earth model, *Phys Earth Planet In*, 25(4), 297-356.
- Fang, M., and B. H. Hager (2001), Vertical deformation and absolute gravity, *Geophys J Int*, 146(2), 539-548.
- Farrell, W. E. (1972), Deformation of the Earth by surface loads, *Rev Geophys*, 10(3), 761-797.
- Farrell, W. E., and J. A. Clark (1976), Postglacial Sea-Level, *Geophys J Roy Astr S*, 46(3), 647-667.
- Fleming, K., and K. Lambeck (2004), Constraints on the Greenland Ice Sheet since the Last Glacial Maximum from sea-level observations and glacial-rebound models, *Quaternary Sci Rev*, 23(9-10), 1053-1077.
- Fischlin, A., G.F. Midgley, J.T. Price, R. Leemans, B. Gopal, C. Turley, M.D.A. Rounsevell, O.P. Dube, J. Tarazona, A.A. Velichko, 2007: Ecosystems, their properties, goods, and services. Climate Change 2007: Impacts, Adaptation and Vulnerability. Contribution of Working Group II to the Fourth Assessment Report

- of the Intergovernmental Panel on Climate Change, M.L. Parry, O.F. Canziani, J.P. Palutikof, P.J. van der Linden and C.E. Hanson, Eds., Cambridge University Press, Cambridge, 211-272.
- Flechtner, F. (2007), AOD1B product description document for product release 01 to 04, GRACE 327~750, GFZ Publ. GR-GFZ-AOD-001 Rev. 3.1, GeoForschungsZentrum Potsdam, Germany.
- Forootan, E., and J. Kusche (2012), Separation of global time-variable gravity signals into maximally independent components, *J Geod*, 86(7), 477-497.
- Gardelle, J., E. Berthier, and Y. Arnaud (2012), Slight mass gain of Karakoram glaciers in the early twenty-first century, *Nature Geosci*, 5(5), 322-325.
- Gardner, A. S., et al. (2013), A reconciled estimate of glacier contributions to sea level rise: 2003 to 2009, *Science*, 340(6134), 852-857.
- Guo, J. Y., X. J. Duan, and C. K. Shum (2010), Non-isotropic Gaussian smoothing and leakage reduction for determining mass changes over land and ocean using GRACE data, *Geophys J Int*, 181(1), 290-302.
- Guo, J. Y., Z. W. Huang, C. K. Shum, and W. van der Wal (2012), Comparisons among contemporary glacial isostatic adjustment models, *J Geodyn*, 61(0), 129-137.
- Guo, J. Y., Y. B. Li, Y. Huang, H. T. Deng, S. Q. Xu, and J. S. Ning (2004), Green's function of the deformation of the Earth as a result of atmospheric loading, *Geophys J Int*, 159(1), 53-68.
- Güntner, A., J. Stuck, S. Werth, P. Döll, K. Verzano, and B. Merz (2007), A global analysis of temporal and spatial variations in continental water storage, *Water Resources Research*, 43(5), W05416.
- Han, D. Z., and J. Wahr (1989), Postglacial Rebound Analysis for a Rotating Earth, *Slow Deformation and Transmission of Stress in the Earth*, 49, 1-6.
- Han, S. C., C. K. Shum, M. Bevis, C. Ji, and C. Y. Kuo (2006), Crustal dilatation observed by GRACE after the 2004 Sumatra-Andaman earthquake, *Science*, 313(5787), 658-662.
- Hanna, E., J. M. Jones, J. Cappelén, S. H. Mernild, L. Wood, K. Steffen, and P. Huybrechts (2013), The influence of North Atlantic atmospheric and oceanic forcing effects on 1900–2010 Greenland summer climate and ice melt/runoff, *International Journal of Climatology*, 33(4), 862-880.
- Hanna, E., X. Fettweis, S. H. Mernild, J. Cappelén, M. H. Ribergaard, C. A. Shuman, K. Steffen, L. Wood, and T. L. Mote (2013), Atmospheric and oceanic climate forcing of the exceptional Greenland ice sheet surface melt in summer 2012, *International Journal of Climatology*, DOI: 10.1002/joc.3743.
- Harig, C., and F. J. Simons (2012), Mapping Greenland's mass loss in space and time, *Proceedings of the National Academy of Sciences*.
- Huang, Z. W., J. Y. Guo, C. K. Shum, J. K. Wan, J. B. Duan, H. S. Fok, and C. Y. Kuo (2013), On the accuracy of glacial isostatic adjustment models for geodetic

- observations to estimate arctic ocean sea-level change, *Terr. Atmos. Ocean. Sci.*, *in press*.
- Huffman, G. J., D. T. Bolvin, E. J. Nelkin, D. B. Wolff, R. F. Adler, G. Gu, Y. Hong, K. P. Bowman, and E. F. Stocker (2007), The TRMM Multisatellite Precipitation Analysis (TMPA): Quasi-Global, Multiyear, Combined-Sensor Precipitation Estimates at Fine Scales, *Journal of Hydrometeorology*, 8(1), 38-55.
- IPCC (2007), Intergovernmental Panel on Climate Change, Climate Change 2007: The Physical Science Basis, Summary for Policymakers.
- Ishii, M., and M. Kimoto (2009), Reevaluation of historical ocean heat content variations with time-varying XBT and MBT depth bias corrections, *Journal of Oceanography*, 65(3), 287-299.
- Invs, E. R., and T. S. James (2005), Antarctic glacial isostatic adjustment: a new assessment, *Antarct Sci*, 17(4), 541-553.
- Invs, E. R., T. S. James, J. Wahr, E. J. O. Schrama, F. W. Landerer, and K. M. Simon (2013), Antarctic contribution to sea level rise observed by GRACE with improved GIA correction, *Journal of Geophysical Research: Solid Earth*, DOI: 10.1002/jgrb.50208.
- Jacob, T., J. Wahr, R. Gross, S. Swenson, and A. Geruo (2012), Estimating geoid height change in North America: past, present and future, *J Geodesy*, 86(5), 337-358.
- Jekeli, C. (1981), Alternative methods to smooth the Earth's gravity field. *Rep. 327*, Ohio state University, Columbus.
- Johannessen, O. M., K. Khvorostovsky, M. W. Miles, and L. P. Bobylev (2005), Recent Ice-Sheet Growth in the Interior of Greenland, *Science*, 310(5750), 1013-1016.
- Johnston, P. (1993), The Effect of Spatially Nonuniform Water Loads on Prediction of Sea-Level Change, *Geophys J Int*, 114(3), 615-634.
- Kaser, G., J. G. Cogley, M. B. Dyurgerov, M. F. Meier, and A. Ohmura (2006), Mass balance of glaciers and ice caps: Consensus estimates for 1961–2004, *Geophysical Research Letters*, 33(19), L19501.
- Kaufmann, G., P. Wu, and G. Y. Li (2000), Glacial isostatic adjustment in Fennoscandia for a laterally heterogeneous earth, *Geophys J Int*, 143(1), 262-273.
- Kemp, A. C., B. P. Horton, J. P. Donnelly, M. E. Mann, M. Vermeer, and S. Rahmstorf (2011), Climate related sea-level variations over the past two millennia, *P Natl Acad Sci USA*, 108(27), 11017-11022.
- Kendall, R. A., J. X. Mitrovica, and G. A. Milne (2005), On post-glacial sea level - II. Numerical formulation and comparative results on spherically symmetric models, *Geophys J Int*, 161(3), 679-706.

- King, M. A., R. J. Bingham, P. Moore, P. L. Whitehouse, M. J. Bentley, and G. A. Milne (2012), Lower satellite-gravimetry estimates of Antarctic sea-level contribution, *Nature*, advance online publication.
- Klees, R., E. A. Revtova, B. C. Gunter, P. Ditmar, E. Oudman, H. C. Winsemius, and H. H. G. Savenije (2008), The design of an optimal filter for monthly GRACE gravity models, *Geophysical Journal International*, 175(2), 417-432.
- Knudsen, P. (2003), Ocean tides in GRACE monthly averaged gravity fields, *Space Sci Rev*, 108(1-2), 261-270.
- Krabill, W., W. Abdalati, E. Frederick, S. Manizade, C. Martin, J. Sonntag, R. Swift, R. Thomas, W. Wright, and J. Yungel (2000), Greenland Ice Sheet: High-Elevation Balance and Peripheral Thinning, *Science*, 289(5478), 428-430.
- Kusche, J. (2007), Approximate decorrelation and non-isotropic smoothing of time-variable GRACE-type gravity field models, *Journal of Geodesy*, 81(11), 733-749.
- Lambeck, K., and M. Nakada (1990), Late Pleistocene and Holocene Sea-Level Change Along the Australian Coast, *Global Planet Change*, 89(1-2), 143-176.
- Lambeck, K., C. Smither, and M. Ekman (1998), Tests of glacial rebound models for Fennoscandinavia based on instrumented sea- and lake-level records, *Geophys J Int*, 135(2), 375-387.
- Latychev, K., J. X. Mitrovica, J. Tromp, M. E. Tamisiea, D. Komatitsch, and C. C. Christara (2005), Glacial isostatic adjustment on 3-D Earth models: a finite-volume formulation, *Geophys J Int*, 161(2), 421-444.
- Lehner, B., and P. Döll (2004), Development and validation of a global database of lakes, reservoirs and wetlands, *Journal of Hydrology*, 296, 1-22.
- Lei, Y., T. Yao, B. W. Bird, K. Yang, J. Zhai, and Y. Sheng (2013), Coherent lake growth on the central Tibetan Plateau since the 1970s: Characterization and attribution, *Journal of Hydrology*, 483(0), 61-67.
- Lemke P., et al. (2007), Observations: Changes in snow, ice and frozen ground, in *Climate Change 2007: The Physical Science Basis: Working Group I Contribution to the Fourth Assessment Report of the International Panel on Climate Change*, edited by S. Solomon et al., pp.339-383, Cambridge Univ. Press, New York.
- Leuliette, E. W., and L. Miller (2009), Closing the sea level rise budget with altimetry, Argo, and GRACE, *Geophys Res Lett*, 36.
- Leuliette, E. W., and J. K. Willis (2011), Balancing the Sea Level Budget, *Oceanography*, 24(2), 122-129.
- Levitus, S., J. I. Antonov, T. P. Boyer, R. A. Locarnini, H. E. Garcia, and A. V. Mishonov (2009), Global ocean heat content 1955-2008 in light of recently revealed instrumentation problems, *Geophys Res Lett*, 36.

- Luthcke, S. B., H. J. Zwally, W. Abdalati, D. D. Rowlands, R. D. Ray, R. S. Nerem, F. G. Lemoine, J. J. McCarthy, and D. S. Chinn (2006), Recent Greenland ice mass loss by drainage system from satellite gravity observations, *Science*, 314(5803), 1286-1289.
- Matsuo, K., and K. Heki (2010), Time-variable ice loss in Asian high mountains from satellite gravimetry, *Earth and Planetary Science Letters*, 290(1-2), 30-36.
- Marcus, S. L., J. O. Dickey, J. K. Willis, and F. Seitz (2009), Earth oblateness changes reveal land ice contribution to interannual sea level variability, *Geophys Res Lett*, 36.
- Mernild S., T. Mote and G. Liston (2011), Greenland ice sheet surface melt extent and trends: 1960-2011, *Journal of Glaciology*, 67: 621-628.
- Meyssignac, B., M. Becker, W. Llovel, and A. Cazenave (2012), An Assessment of Two-Dimensional Past Sea Level Reconstructions Over 1950-2009 Based on Tide-Gauge Data and Different Input Sea Level Grids, *Surv Geophys*, 33(5), 945-972.
- Milne, G. A. (1998), Refining models of the glacial isostatic adjustment process, Dissertation thesis, University of Toronto, Toronto.
- Milne, G. A., and J. X. Mitrovica (1998), Postglacial sea-level change on a rotating Earth, *Geophys J Int*, 133(1), 1-19.
- Mitrovica, J. X., and W. R. Peltier (1991), On Postglacial Geoid Subsidence over the Equatorial Oceans, *J Geophys Res-Sol Ea*, 96(B12), 20053-20071.
- Mitrovica, J. X., and W. R. Peltier (1993), Present-Day Secular Variations in the Zonal Harmonics of Earth's Geopotential, *J Geophys Res-Sol Ea*, 98(B3), 4509-4526.
- Mitrovica, J. X., and G. A. Milne (2003), On post-glacial sea level: I. General theory, *Geophys J Int*, 154(2), 253-267.
- Mitrovica, J. X., and J. Wahr (2011), Ice Age Earth Rotation, *Annu Rev Earth Pl Sc*, 39, 577-616.
- Mitrovica, J. X., G. A. Milne, and J. L. Davis (2001), Glacial isostatic adjustment on a rotating earth, *Geophys J Int*, 147(3), 562-578.
- Molnar, P., and P. Tapponnier (1978), Active tectonics of Tibet, *Journal of Geophysical Research: Solid Earth*, 83(B11), 5361-5375.
- Morison, J., R. Kwok, C. Peralta-Ferriz, M. Alkire, I. Rigor, R. Andersen, and M. Steele (2012), Changing Arctic Ocean freshwater pathways, *Nature*, 481(7379), 66-70.
- Munk, W. H., and G. J. MacDonald (1960), *The rotation of the earth; a geophysical discussion*, 323 p. pp., University Press, Cambridge Eng.
- Nakada, M., and K. Lambeck (1988), The Melting History of the Late Pleistocene Antarctic Ice-Sheet, *Nature*, 333(6168), 36-40.

- Nakada, M., and K. Lambeck (1991), Late Pleistocene and Holocene Sea-Level Change - Evidence for Lateral Mantle Viscosity Structure, *Nato Adv Sci I C-Mat*, 334, 79-94.
- Nerem, R. S., and J. Wahr (2011), Recent changes in the Earth's oblateness driven by Greenland and Antarctic ice mass loss, *Geophys Res Lett*, 38.
- NGS (1986), Geodetic Glossary, National Geodetic Survey, Rockville, MD, September 1986.
- Paulson, A., S. J. Zhong, and J. Wahr (2005), Modelling post-glacial rebound with lateral viscosity variations, *Geophys J Int*, 163(1), 357-371.
- Paulson, A., S. J. Zhong, and J. Wahr (2007), Inference of mantle viscosity from GRACE and relative sea level data, *Geophys J Int*, 171(2), 497-508.
- Peltier, W. R. (1998), Postglacial variations in the level of the sea: Implications for climate dynamics and solid-earth geophysics, *Rev Geophys*, 36(4), 603-689.
- Peltier, W. R. (2004), Global glacial isostasy and the surface of the ice-age earth: The ice-5G (VM2) model and grace, *Annual Review of Earth and Planetary Sciences*, 32, 111-149.
- Peltier, W. R. (2009), Closure of the budget of global sea level rise over the GRACE era: the importance and magnitudes of the required corrections for global glacial isostatic adjustment, *Quaternary Sci Rev*, 28(17-18), 1658-1674.
- Peltier, W. R., and A. M. Tushingham (1991), Influence of Glacial Isostatic-Adjustment on Tide-Gauge Measurements of Secular Sea-Level Change, *J Geophys Res-Solid*, 96(B4), 6779-6796.
- Peltier, W. R., R. Drummond, and K. Roy (2012), Comment on “Ocean mass from GRACE and glacial isostatic adjustment” by D. P. Chambers et al, *Journal of Geophysical Research: Solid Earth*, 117(B11), B11403.
- Pritchard, H. D., R. J. Arthern, D. G. Vaughan, and L. A. Edwards (2009), Extensive dynamic thinning on the margins of the Greenland and Antarctic ice sheets, *Nature*, 461(7266), 971-975.
- Qiu, J. (2008), China: The Third Pole, *Nature*, 454, 393-396.
- Purcell, A., A. Dehecq, P. Tregoning, E. K. Potter, S. C. McClusky, and K. Lambeck (2011), Relationship between glacial isostatic adjustment and gravity perturbations observed by GRACE, *Geophys Res Lett*, 38.
- Rahmstorf, S., A. Cazenave, J. A. Church, J. E. Hansen, R. F. Keeling, D. E. Parker, and R. C. J. Somerville (2007), Recent climate observations compared to projections, *Science*, 316(5825), 709-709.
- Richman, M. (1986), Rotation of principal components, *Int. J. Climatol.*, 06, 293-335.

- Rienecker, M. M., and Coauthors (2011): MERRA: Modern-Era Retrospective Analysis for Research and Applications. *J. Climate*, 24, 3624-3648.
- Rignot, E., and R. H. Thomas (2002), Mass Balance of Polar Ice Sheets, *Science*, 297(5586), 1502-1506.
- Rignot, E., J. L. Bamber, M. R. van den Broeke, C. Davis, Y. Li, W. J. van de Berg, and E. van Meijgaard (2008), Recent Antarctic ice mass loss from radar interferometry and regional climate modelling, *Nature Geosci*, 1(2), 106-110.
- Rignot, E., I. Velicogna, M. R. van den Broeke, A. Monaghan, and J. T. M. Lenaerts (2011), Acceleration of the contribution of the Greenland and Antarctic ice sheets to sea level rise, *Geophysical Research Letters*, 38(5), L05503.
- Rodell, M., et al. (2004), The Global Land Data Assimilation System, *Bulletin of the American Meteorological Society*, 85(3), 381-394.
- Rodell, M., I. Velicogna, and J. S. Famiglietti (2009), Satellite-based estimates of groundwater depletion in India, *Nature*, 460(7258), 999-1002.
- Roemmich, D., and J. Gilson (2009), The 2004–2008 mean and annual cycle of temperature, salinity, and steric height in the global ocean from the Argo Program, *Prog Oceanogr*, 82(2), 81-100.
- Roemmich, D., G. C. Johnson, S. Riser, R. Davis, J. Gilson, W. B. Owens, S. L. Garzoli, C. Schmid, and M. Ignaszewski (2009), The Argo Program: Observing the global ocean with profiling floats.
- Rubincam, D. P. (1984), Postglacial Rebound Observed by Lageos and the Effective Viscosity of the Lower Mantle, *J Geophys Res*, 89(Nb2), 1077-1087.
- Sasgen, I., V. Klemann, and Z. Martinec (2012), Towards the inversion of GRACE gravity fields for present-day ice-mass changes and glacial-isostatic adjustment in North America and Greenland, *J Geodyn*, 59, 49-63.
- Sasgen, I., H. Konrad, E. R. Ivins, M. R. van den Broeke, J. L. Bamber, Z. Martinec, and V. Klemann (2012), Antarctic ice-mass balance 2002 to 2011: regional re-analysis of GRACE satellite gravimetry measurements with improved estimate of glacial-isostatic adjustment, *The Cryosphere Discuss.*, 6(5), 3703-3732.
- Schrama, E. J. O., B. Wouters, and D. A. Lavallee (2007), Signal and noise in Gravity Recovery and Climate Experiment (GRACE) observed surface mass variations, *Journal of Geophysical Research-Solid Earth*, 112(B8).
- Schrama, E. J. O., and B. Wouters (2011), Revisiting Greenland ice sheet mass loss observed by GRACE, *Journal of Geophysical Research-Solid Earth*, 116.
- Shepherd, A., and D. Wingham (2007), Recent Sea-Level Contributions of the Antarctic and Greenland Ice Sheets, *Science*, 315(5818), 1529-1532.
- Shepherd, A., et al. (2012), A Reconciled Estimate of Ice-Sheet Mass Balance, *Science*, 338(6111), 1183-1189.
- Shum, C. K., and C. Y. Kuo (2011), Observation and Geophysical Causes of Present-Day Sea-Level Rise, *Climate Change and Food Security in South Asia*, 85-104.

- Shum, C. K., and C. Y. Kuo (2013), *Climate Change and Sea-Level Rise*, edited by Y. Q. Wang, Taylor and Francis.
- Shum, C. K., C. Y. Kuo, J. Y. Guo, J. B. Duan, and Z. W. Huang (2012), Present-Day Ocean Sea-Level Budget, in *AOGS-AGU (WPGM) Joint Assembly*, Singapore, August 13-17, 2012.
- Simpson, M. J. R., G. A. Milne, P. Huybrechts, and A. J. Long (2009), Calibrating a glaciological model of the Greenland ice sheet from the Last Glacial Maximum to present-day using field observations of relative sea level and ice extent, *Quaternary Sci Rev*, 28(17-18), 1631-1657.
- Song, Y. T., and F. Colberg (2011), Deep ocean warming assessed from altimeters, Gravity Recovery and Climate Experiment, in situ measurements, and a non-Boussinesq ocean general circulation model, *J Geophys Res-Oceans*, 116.
- Spada, G., V. R. Barletta, V. Klemann, R. E. M. Riva, Z. Martinec, P. Gasperini, B. Lund, D. Wolf, L. L. A. Vermeersen, and M. A. King (2011), A benchmark study for glacial isostatic adjustment codes, *Geophys J Int*, 185(1), 106-132.
- Stern, N. H., and G. Britain (2006), *Stern Review: The economics of climate change*, HM treasury London.
- Swenson, S., and J. Wahr (2006), Post-processing removal of correlated errors in GRACE data, *Geophys Res Lett*, 33(8).
- Swenson, S., D. Chambers, and J. Wahr (2008), Estimating geocenter variations from a combination of GRACE and ocean model output, *Journal of Geophysical Research: Solid Earth*, 113(B8), B08410.
- Swenson, S.C. and J.M. Wahr (2011), Estimating signal loss in regularized GRACE gravity field solutions, *Geophysical Journal International*, 185(2), 693-702.
- Tamisiea, M. E. (2011), Ongoing glacial isostatic contributions to observations of sea level change, *Geophys J Int*, 186(3), 1036-1044.
- Tamisiea, M. E., and J. X. Mitrovica (2011), The Moving Boundaries of Sea Level Change Understanding the Origins of Geographic Variability, *Oceanography*, 24(2), 24-39.
- Tamisiea, M. E., J. X. Mitrovica, and J. L. Davis (2007), GRACE gravity data constrain ancient ice geometries and continental dynamics over Laurentia, *Science*, 316(5826), 881-883.
- Tapley, B. D., S. Bettadpur, M. Watkins, and C. Reigber (2004), The gravity recovery and climate experiment: Mission overview and early results, *Geophys Res Lett*, 31(9).
- Tedesco, M., et al. (2011), The role of albedo and accumulation in the 2010 melting record in Greenland, *Environ. Res. Lett.* 6(1), doi: 10.1088/1748-9326/6/1/014005.

- Thomas, R., et al. (2004), Accelerated Sea-Level Rise from West Antarctica, *Science*, 306(5694), 255-258.
- Tiwari, V. M., J. Wahr, and S. Swenson (2009), Dwindling groundwater resources in northern India, from satellite gravity observations, *Geophysical Research Letters*, 36(18), L18401.
- van der Wal, W., E. Kurtenbach, J. Kusche, and B. Vermeersen (2011), Radial and tangential gravity rates from GRACE in areas of glacial isostatic adjustment, *Geophys J Int*, 187(2), 797-812.
- Velicogna, I., and J. Wahr (2002), A method for separating antarctic postglacial rebound and ice mass balance using future ICESat Geoscience Laser Altimeter System, Gravity Recovery and Climate Experiment, and GPS satellite data, *J Geophys Res-Sol Ea*, 107(B10).
- Velicogna, I., and J. Wahr (2005), Greenland mass balance from GRACE, *Geophys Res Lett*, 32(18).
- Velicogna, I., and J. Wahr (2006), Acceleration of Greenland ice mass loss in spring 2004, *Nature*, 443(7109), 329-331.
- Velicogna, I. (2009), Increasing rates of ice mass loss from the Greenland and Antarctic ice sheets revealed by GRACE, *Geophysical Research Letters*, 36(19), L19503.
- Velicogna, I., and J. Wahr (2013), Time-variable gravity observations of ice sheet mass balance: Precision and limitations of the GRACE satellite data, *Geophysical Research Letters*, 40, doi:[10.1002/grl.50527](https://doi.org/10.1002/grl.50527).
- Vermeer, M., and S. Rahmstorf (2009), Global sea level linked to global temperature, *Proceedings of the National Academy of Sciences*, 106(51), 21527-21532.
- Wahr, J., H. Dazhong, and A. Trupin (1995), Predictions of Vertical Uplift Caused by Changing Polar Ice Volumes on a Viscoelastic Earth, *Geophys Res Lett*, 22(8), 977-980.
- Wahr, J., M. Molenaar, and F. Bryan (1998), Time variability of the Earth's gravity field: Hydrological and oceanic effects and their possible detection using GRACE, *J Geophys Res-Sol Ea*, 103(B12), 30205-30229.
- Wahr, J., S. Swenson, V. Zlotnicki, and I. Velicogna (2004), Time-variable gravity from GRACE: First results, *Geophys Res Lett*, 31(11).
- Wahr, J., S. Swenson, and I. Velicogna (2006), Accuracy of GRACE mass estimates, *Geophysical Research Letters*, 33(6).
- Wang, H., and P. Wu (2006), Effects of lateral variations in lithospheric thickness and mantle viscosity on glacially induced surface motion on a spherical, self-gravitating Maxwell Earth, *Earth Planet Sc Lett*, 244(3-4), 576-589.
- Whitehouse, P. L., M. J. Bentley, G. A. Milne, M. A. King, and I. D. Thomas (2012), A new glacial isostatic adjustment model for Antarctica: calibrated and tested using

- observations of relative sea-level change and present-day uplift rates, *Geophys J Int*, 190(3), 1464-1482.
- Willis, J. K., D. P. Chambers, and R. S. Nerem (2008), Assessing the globally averaged sea level budget on seasonal to interannual timescales, *J Geophys Res-Oceans*, 113(C6).
- Willis, J. K., D. P. Chambers, C. Y. Kuo, and C. K. Shum (2010), Global Sea Level Rise RECENT PROGRESS AND CHALLENGES FOR THE DECADE TO COME, *Oceanography*, 23(4), 26-35.
- Wingham, D. J., A. J. Ridout, R. Scharroo, R. J. Arthern, and C. K. Shum (1998), Antarctic elevation change from 1992 to 1996, *Science*, 282(5388), 456-458.
- Wingham, D. J., M. J. Siegert, A. Shepherd, and A. S. Muir (2006), Rapid discharge connects Antarctic subglacial lakes, *Nature*, 440(7087), 1033-1036.
- Woodworth, P. L., and R. Player (2003), The permanent service for mean sea level: An update to the 21st century, *J Coastal Res*, 19(2), 287-295.
- Wouters, B., and E. J. O. Schrama (2007), Improved accuracy of GRACE gravity solutions through empirical orthogonal function filtering of spherical harmonics, *Geophysical Research Letters*, 34(23).
- Wouters, B., D. Chambers, and E. J. O. Schrama (2008), GRACE observes small-scale mass loss in Greenland, *Geophysical Research Letters*, 35(20).
- Wu, P. (2005), Effects of lateral variations in lithospheric thickness and mantle viscosity on glacially induced surface motion in Laurentia, *Earth Planet Sc Lett*, 235(3-4), 549-563.
- Wu, P., and W. van der Wal (2003), Postglacial sealevels on a spherical, self-gravitating viscoelastic earth: effects of lateral viscosity variations in the upper mantle on the inference of viscosity contrasts in the lower mantle, *Earth Planet Sc Lett*, 211(1-2), 57-68.
- Yao, T., et al. (2012), Different glacier status with atmospheric circulations in Tibetan Plateau and surroundings, *Nature Clim. Change*, 2(9), 663-667.
- Yoder, C. F., J. G. Williams, J. O. Dickey, B. E. Schutz, R. J. Eanes, and B. D. Tapley (1983), Secular Variation of Earth's Gravitational Harmonic J2 Coefficient from Lages and Nontidal Acceleration of Earth Rotation, *Nature*, 303(5920), 757-762.
- Zhong, S. J., A. Paulson, and J. Wahr (2003), Three-dimensional finite-element modelling of Earth's viscoelastic deformation: effects of lateral variations in lithospheric thickness, *Geophys J Int*, 155(2), 679-695.
- Zenner, L., T. Gruber, A. Jaggi, and G. Beutler (2010), Propagation of atmospheric model errors to gravity potential harmonics-impact on GRACE de-aliasing, *Geophysical Journal International*, 182(2), 797-807.
- Zenner, L., E. Fagiolini, I. Daras, F. Flechtner, T. Gruber, T. Schmidt, and G. Schwarz (2012), Non-tidal atmospheric and oceanic mass variations and their impact on GRACE data analysis, *Journal of Geodynamics*, 59, 9-15.

Zwally, H. J., M. B. Giovinetto, J. Li, H. G. Cornejo, M. A. Beckley, A. C. Brenner, J. L. Saba, and D. Yi (2005), Mass changes of the Greenland and Antarctic ice sheets and shelves and contributions to sea-level rise: 1992-2002, *Journal of Glaciology*, 51(175), 509-527.

Zwally, H., M. Giovinetto, M. Beckley, and J. Saba (2012), Antarctic and Greenland Drainage Systems, GSFC Cryospheric Sciences Laboratory.

Appendix

Empirical Orthogonal Functions (EOF) Analysis

Products of geodetic observing systems (e.g., GRACE monthly gravity fields and satellite altimetry data which are used in this study) and geophysical models (e.g., hydrology and atmospheric models) are most commonly represented in form of time series of spatially distributed grid points [Kusche et al., 2011]. Usually, most of the geophysical signals are dominated by a few spatial patterns and temporal variability. Identifying these most important patterns can help interpreting the dynamical/physical behavior involved within these data/model systems. The Empirical Orthogonal Functions (EOF), also known as the more common name Principal Component Analysis (PCA), is one of the most popular analysis techniques that are employed to identify spatial patterns and temporal variability of geophysical fields. Here, we describe the EOF method with corresponding mathematical concepts behind it according to Kusche et al. [2011].

The original aim of EOFs was to decompose a continuous space-time field $X(t,s)$, where t and s represent time and spatial variables, as:

$$X(t,s) = \sum_{k=1}^M c_k(t) u_k(s) \quad \text{A-1}$$

where M is the number of modes, $u_k(s)$ is an optimal set of basis function of space, and $c_k(t)$ are expansion functions of time [Hannachi et al., 2006]. The EOF/PCA has been used extensively to extract dominant modes that capture most of the observed data variability, while simultaneously suppressing those modes with low variance.

Suppose we have gridded data sets composed of a continuous space-time field $X(t,s)$ at time t and spatial position s . The observed field can be represented as:

$$\mathbf{X} = (\mathbf{x}_1, \mathbf{x}_2, \dots, \mathbf{x}_m) \quad \text{A-2}$$

with $n \times 1$ data vector \mathbf{x} , given for time epochs t_i :

$$\mathbf{x}_i = \begin{pmatrix} x_{1i} \\ x_{2i} \\ \vdots \\ x_{ni} \end{pmatrix} \quad i=1,2,\dots,m. \quad \text{A-3}$$

In our study, \mathbf{X}_i represent the values of observed or modeled field in n spatial locations at time epoch t_i . The data are also assumed to be centered, with temporal mean of each spatial points already being subtracted from the observations, i.e.

$$\frac{1}{m} \sum_{i=1}^m x_{ji} = 0 \quad \text{A-4}$$

The aim of EOF analysis is to find uncorrelated linear combinations of the different variables that explain maximum variance. The covariance matrix of the anomaly data matrix \mathbf{X} is defined as:

$$\mathbf{C} = \frac{1}{m} \mathbf{X}\mathbf{X}^T \quad \text{A-5}$$

Note that the covariance matrix \mathbf{C} contains the variances and co-variances of the data viewed as time series per location, in contrast to $\mathbf{C}^* = \frac{1}{n} \mathbf{X}^T \mathbf{X}$ which contains the spatial variance and covariance of the data viewed as functions of position for any time epoch. The total variance is given by:

$$\Delta^2 = \text{trace}(\mathbf{C}) = \frac{1}{m} \sum_{j=1}^n \left(\sum_{i=1}^m x_{ji}^2 \right) \quad \text{A-6}$$

To find uncorrelated linear combination of different variables that explain maximum variance means to find a unit-length direction $\mathbf{u} = (u_1, u_2, \dots, u_n)^T$, such that $\mathbf{X}\mathbf{u}$ has maximum variability [Hannachi et al., 2006], which yields:

$$\max(\mathbf{u}^T \mathbf{C} \mathbf{u}), \text{ s.t. } \mathbf{u}^T \mathbf{u} = 1 \quad \text{A-7}$$

The EOF analysis is therefore obtained as the solution to the eigenvalue problem. An alternative way to decompose the data vector is given by the eigenvalue decomposition of \mathbf{C} :

$$\mathbf{C} = \mathbf{E}\mathbf{\Lambda}\mathbf{E}^T \quad \text{A-8}$$

where $\mathbf{\Lambda}$ is a diagonal matrix which contain the n eigenvalues λ_j , and the $n \times n$ matrix \mathbf{E} contain the corresponding eigenvectors \mathbf{e}_j . The sum of all the eigenvalues satisfies:

$$\sum_{j=1}^n \lambda_j = \Delta^2 \quad \text{A-9}$$

Assuming the eigenvalues are normally sorted in decreasing order as $\lambda_1 \geq \lambda_2 \geq \dots \geq \lambda_n$. One can state that each eigenvalue explain a fraction $\eta_j = \lambda_j / \Delta^2$ of the total variance.

EOF analysis/PCA replaces the basis \mathbf{u}_j with \mathbf{e}_j as the vector basis for representing the original observations \mathbf{x}_i , The convention, about the scaling of the eigenvectors, has to be adopted, such that:

$$\mathbf{e}_j^T \mathbf{e}_j = 1 \quad \text{A-10}$$

\mathbf{e} can be viewed as discrete version of a function which describes common pattern in the entire data, and are called EOFs or simply ‘modes’. For original data which are provided on 2-D gridded locations, it is common to visualize the corresponding EOFs on the grid. Then the principal component representation of the data vector is:

$$\mathbf{x}_i = \sum_{j=1}^n d_{ji} \mathbf{e}_j = \mathbf{E} \mathbf{d}_i \quad \text{A-11}$$

where the principal components (PCs) are determined by projecting the original data vector onto the new basis:

$$\mathbf{d}_i = \mathbf{E}^T \mathbf{x}_i \quad \text{A-12}$$

The data vector can be reconstructed with only a few EOFs and corresponding PCs which represent the largest part of the total variability.

Rotation

In the real world, the mathematical constraints of EOF analysis/PCA, i.e. spatial orthogonality of EOFs and temporal uncorrelation of PCs, impose limits on physical interpretability of PCA results, because physical processes are not independent, and physical modes are non-orthogonal in general. To gain easy interpretation, Rotated EOFs (REOF) is most widely used to find physically plausible modes, by sacrificing either orthogonality of the EOFs or uncorrelatedness of the PCs and applying new optimization criteria.

Rotated EOFs can be defined by straightly applying an orthogonal matrix \mathbf{V} to the EOFs: $\mathbf{R} = \mathbf{E} \mathbf{V}^T$. The rotated EOFs still remain orthogonal since $\mathbf{R}^T \mathbf{R} = \mathbf{V} \mathbf{E}^T \mathbf{E} \mathbf{V}^T = \mathbf{I}$, but the rotated PCs $\mathbf{r}_i = \mathbf{V} \mathbf{d}_i = \mathbf{R}^T \mathbf{y}_i$ loose the property of being uncorrelated.

To determine the optimized orthogonal matrix V in EOF and PC rotations, various criteria have been applied, in our study, we choose to follow the VARIMAX criterion [Kaiser 1958] only, which maximizes a simplicity criterion according to:

$$\max \left(f(V) = \sum_{i=1}^m \left(\sum_{j=1}^n R_{ji}^4 - \frac{\gamma}{n} \left(\sum_{j=1}^n R_{ji}^2 \right)^2 \right) \right) \quad \text{A-13}$$

The value inside the summations is proportional to the variance of the square of the rotated EOFs, this variance will be big if some R_{ji} are close to 1 and many others are near 0.